Study of crack initiation in low-cycle fatigue of an austenitic stainless steel

Pengfei Mu

N° d'ordre : 154

ECOLE CENTRALE DE LILLE

THESE

présentée en vue
d'obtenir le grade de

DOCTEUR

en

Spécialité : Mécanique

par

Pengfei MU

DOCTORAT DELIVRE PAR L'ECOLE CENTRALE DE LILLE

Titre de la thèse :

Etude de l'amorçage en fatigue plastique d'un acier inoxydable austénitique

Study of crack initiation in low-cycle fatigue of an austenitic stainless steel

Soutenue publiquement le 29 mars 2011 devant le jury d'examen :

Président	Jean-Bernard Vogt, Professeur, UMET, Université de Lille 1
Rapporteur	Véronique Favier, Professeur, PIMM, ENSAM Paris
Rapporteur	Patrick Villechaise, Directeur de recherche, Institut P', ENSMA
Membre	Philippe Bompard, Professeur, Ecole Centrale Paris
Membre	Eric Charkaluk, Chargé de recherche, LML, Ecole Centrale de Lille
Directrice de thèse	Véronique Aubin, Professeur, Ecole Centrale Paris

Thèse préparée dans le Laboratoire de Mécanique de Lille (UMR CNRS 8107)

Ecole Doctorale SPI 072 (Lille I, Lille III, Artois, ULCO, UVHC, EC Lille)

PRES Université Lille Nord de France

ACKNOWLEDGEMENT

I start by thanking all the members of the jury for having accepted to examine this work and for their interests and remarks.

Then my deepest gratitude goes to my supervisors Madame Véronique AUBIN for having welcomed me and followed me during my thesis. I would like to thank her for her professional instructions and suggestions, her personal quality and scientific literacy, and her constant patience and encouragement, that guided me, influenced me and got me through this work.

I'd like also to thank Madame Suzanne Degallaix-Moreuil, my supervisor during my first year of thesis, for her guidance and kindness. Her pragmatic and strict attitude toward work set a good example for me in my scientific life.

I'm grateful to my supervisors during my graduate study in China, Mr Yongsheng LI and Mr Xiongyao XIE, who recommended to study in France, and to the China Scholarship Council, who provided the scholarship to me for my study and my life in France.

I would also like to acknowledge the important contribution of others to this work.
First, I would like to show my gratitude to Madame Iris ALVAREZ, Mr Alberto F. ARMAS (professors), and Fernando (technician) of the Instituto de Física Rosario (Argentina), who welcomed me in Argentina and helped me realize the fatigue test and in-situ observation. I would also thank Gaby, who accommodated me, and all the other ebullient Argentine friends in Gaby's residence who gave me friendship and unforgettable memories during my stay.

My sincere thanks are also given to the Laboratoire de Mécanique des Sols, Structures et Matériaux, in paticular Madame Françoise GARNIER, who carried out the EBSD measurement, and Yan LI, who helped in the finite element calculation.

I am indebted to all my colleagues and teachers of the laboratoire de Mécanique de Lille and of the Ecole Centrale de Lille, in particular Pierre and Jean (Fortran), Ahmed (image correlation and redaction), Mohamed (redaction), François (specimen maching), David and Xavier (SEM), Jean-Yves (chemical etching), Marie-Claire (secretariat), for their kindness and support throughout my work.

Last but not the least, my gratitude also extends to my family and my friends who have been assisting, supporting and caring for me all my life.

CONTENT TABLE

GENERAL INTRODUCTION

In order to answer to higher and higher quality requirements, in the one hand, and, in the other hand, in order to reduce the conception cost, manufacturers need today to predict at best the fatigue behavior of their structures under real loading conditions. Numerous models exist in the literature and allow to predict the number of cycles to failure. Based on empirical observations, they describe more or less the mean stress effects, the multiaxial effects and variable amplitude loadings. However, these criteria are based on macroscopic observations and cannot be directly linked to the microstructure properties. They cannot supply any answer to the following questions. How extrapolate a parameter set identified on a given material to a second material? Which characteristics of the microstructure are harmful or should be favored with respect to the fatigue life?

Failure in fatigue results from two successive phenomena: first of all the initiation of cracks followed by their propagation and competition until one main crack leads to the rupture of the structure. Crack initiation, as micropropagation, is completely governed by the microstructure. This study focuses on the analysis and the prediction of crack initiation in low-cycle fatigue.

Some crack initiation criteria have been defined considering plastic strains in a grain, based on considerations on the physical mechanisms of plastic deformation (PSB, dislocation, vacancies, etc.) [Tanaka 81] [Manonukul 04] [Sangid 11], or using dislocation dynamics [Déprés 04] but the initiation mechanisms are still not fully understood and the existent criteria are not easy to use, as they need local variables at the grain scale.

The material studied is an austenitic stainless steel. This type of steels has high ductility, low yield stress and relatively high ultimate tensile strength compared to typical carbon steels. Because of their high chromium (which contributes to their inoxydability) and nickel (which helps to form the austenitic structure) contents, the austenitic stainless steels provide a very high corrosion resistance combined to good mechanical properties. So in the past 50 years, austenitic stainless steels have been widely used in corrosive environments, such as cryogenic technology, nuclear equipment, chemistry, ocean technology, food industry, biomedicine and petrochemical processing. This family of stainless steels accounts for about 65-70 % of the total amount of stainless steels that are produced.

The present study aims at establishing a crack initiation criterion in low-cycle fatigue, which should be usable under variable amplitude loading conditions. A mean field approach was chosen in order to simulate easily variable complex cyclic loadings applied to the material. The grains of the material are then represented as surrounded by all the other grains, without taking into account the influence of neighbouring grains. As crack initiation occurs at the surface in fatigue, a specific localization law has to be established in order to account for the fact that grains in surface are less constrained than in the bulk. The first objective of this work is thus to provide a numerical frame allowing to test initiation criteria in fatigue. Moreover, the second objective is to discriminate between existing criteria from the literature on the same experimental data base. The study is focused on intragranular crack initiation as the framework of the mean field approach chosen does not allow to consider the influence of neighbouring grains. Crystallographic parameters influencing the intragranular crack initiation were then studied, considering the necessity of high number of statistical experimental data, due to the scattering observed in fatigue. The mechanical behavior of grains at the surface was simulated and various crack initiation criteria compared to the experimental results.

The research objective is to analyze the crack initiation in a stainless steel AISI 316L under low-cycle fatigue. For that, first, tension-compression fatigue tests have been carried out to characterize the mechanical behavior of the material and to validate the different constitutive laws. The surface of specimen was observed in-situ to monitor the evolution of surface damage. After the test, the specimen surface was observed by SEM to verify the crack initiation and to identify the cracks directions. Then, the specimen surface was scanned by EBSD to obtain the crystallographic orientations. To determine the number of cycles to crack initiation, the method of image correlation was adopted. Besides the fatigue test and analysis related, the simulation aiming at modeling the mechanical behavior and fatigue behavior was done with a Fortran program (SiDoLo). A finite element simulation is scheduled to identify the parameters in the localization law for surface grains and to analyze the influence of neighboring grains.

This thesis is composed of five chapters:

In chapter I, some basic knowledge on fatigue analysis will be presented. At first, the concept of fatigue is introduced. Second, an introduction to the anti-corrosion principle of stainless steels, to the classification of stainless steels, and to austenitic stainless steels is given. Third, the experimental

procedures and some classic results for this material will be presented. Fourth, factors influencing the heterogeneity of stresses and strains at the microstrutural scale will be introduced. At the end of this chapter, crack initiation and propagation in fatigue will be presented.

Chapter II aims at characterizing the mechanical behavior of the studied material. The material studied, the equipment and experimental procedures are presented consequently. The experimental results of tensile tests in monotonic and low-cycle fatigue conditions were carried out. Their results are given and analyzed.

In chapter III, the modeling of the mechanical behavior of the studied material will be discussed. A multi-scale approach is adopted in the modeling. This approach has two main advantages: it can firstly be used to account for both macroscopic and microscopic phenomena as it is based on physical plastic description and needs secondly a limited computation time compared which allows to simulate complex cyclic loadings. The localization, local crystalline behavior and homogenization laws adopted in the modeling are presented. In the second part of this chapter, the parameters used in the modeling were identified either by direct measurement from experimental results, either from the literature or by inverse method using genetic algorithm.

Chapter IV aims at analyzing the plasticity and surface damage during a low-cycle fatigue test. A tension-compression fatigue test was carried out with an in-situ observation system, which allows to observe the specimen surface during the test. The observation zones were scanned by electron back scatter diffraction (EBSD) after the test in order to establish grain orientations. The specimen surface was then observed with a scanning electron microscope (SEM). The sites for crack initiation have been identified, and the orientations of slip systems associated to microcracks analyzed. Digital image correlation was used to calculate strain and displacement fields at the grain scale to determine the crack initiation time.

Chapiter V is dedicated to the analysis of crack initiation criteria. Because surface grains are less constraint than grains in the bulk, a specific localization law for surface grains has to be introduced. The Finite Element calculations made to identify its parameters are then described. Then, some fatigue life criteria and crack initiation criteria from literatures are presented. The indicators used in

these criteria are analyzed and evaluated by comparison to the experimental data. Two crack initiation criteria with good indicator performance proposed by Tanaka and Mura [Mura 94] and C. Déprés [Déprés 04] are then presented in detail and evaluated.

At last, the general conclusion sums up the main results obtained and describes some perspectives of this work.

I. INTRODUCTION TO FATIGUE AND TO CRACK INITIATION

In this first chapter, some basic knowledge on fatigue analysis will be presented. This chapter is organized as follows. Section I.1 introduces the concept of fatigue and the famous Wöhler curve used in fatigue analysis. The properties of stainless steels are presented in section I.2. Section I.3 will present, on the one hand, the procedures to carry out mechanical tests and to collect data and, on the other hand, the mechanical behavior of austenitic stainless steels under cyclic loading. In section I.4, the plastic crystalline behavior of polycrystalline materials will be introduced. The source of plasticity, factors influencing the distribution of intragranular stress and strain, and the plasticity induced relief are presented. Section I.5 presents crack initiation, the location sites observed and factors. At last, crack propagation will be introduced briefly, as it is not the main subject of this study.

I.1. WHAT IS FATIGUE ?

The term “fatigue” defines the damage and failure of materials under cyclic loadings. Damage and failure occur even if stresses applied to the component are lower than the tensile strength, σ_{TS}, and also lower than the yield strength, σ_y.

There exist various forms of fatigue. The most common fatigue is mechanical fatigue (see FIG. I.1a)), which is the result of a cyclic mechanical loading, which induces cyclic stresses and strains. If the cyclic loadings are applied together with high temperatures or fluctuant temperatures, creep-fatigue or thermomechanical fatigue can occur (see FIG. I.1b)). A corrosive environment may give rise to corrosion-fatigue (see FIG. I.1c)). Contact fatigue or fretting fatigue (see FIG. I.1d)) may be the result of the repeated loadings applied on the rolling surface between materials. Various forms of fatigue may often coexist, depending of the loading and environment conditions.

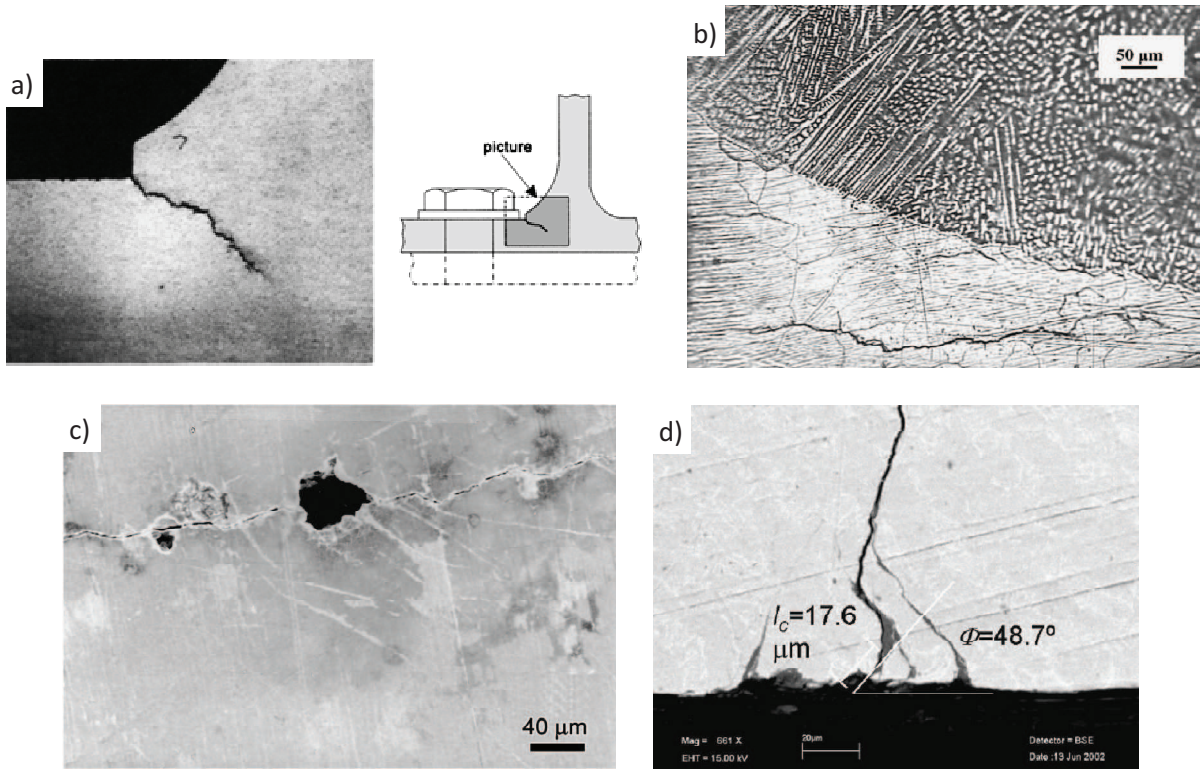

FIG. I.1 - Various forms of fatigue cracks: a) Cross section of mechanical fatigue cracks at sharp corner [Schijve 09]; b) Thermomechanical fatigue crack near weld-base interface at 823 K ± 0.6 % [Prasad Reddy 08]; c) Corrosion fatigue crack crossing a pit [Xie 02]; d) Multiple fretting fatigue cracks emerging from the contact surface (at the bottom of the micrograph) [Conner 04].

Wöhler curve, also called S-N curve, is often used to characterize the material performance in fatigue. It shows the relationship between the cyclic stress amplitude applied to a component and the number of cycles to failure in the logarithmic scale. In order to get a Wöhler curve, several cyclic mechanical tests have to be made. During the tests, material specimens are loaded/unloaded with given loading parameters (load ratio, load level, roughness of the specimen …) until failure, and the number of cycles to failure for each specimen is registered. The result (stress level and number of cycles to failure) for each specimen generates one point in the Wöhler curve. Because of the scattering between specimens, a high number of tests have to be carried out to construct the Wöhler curve.

FIG. I.2 shows an example of Wöhler curve. It can be seen that a given stress amplitude leads to various numbers of cycles to failure, N_R. When the stress amplitude decreases, the scattering of N_R increases [François 91]. In fact, many factors can influence fatigue life, e.g. the surface roughness and the heterogeneity of the material microstructure. This scattering in the number of cycles to failure

makes the prediction of fatigue life very difficult. In order to obtain an acceptable failure probability, a security coefficient is generally used in fatigue design.

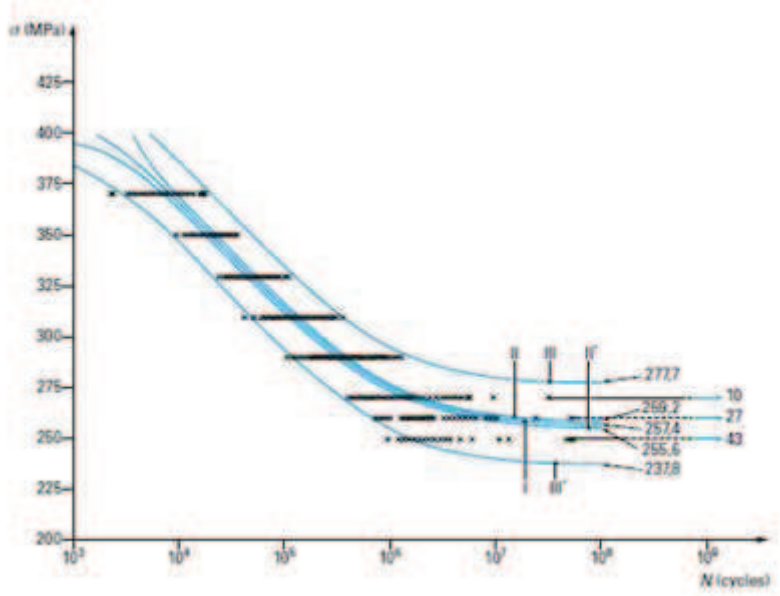

FIG. I.2 - Wöhler Curve of steel XC 10 [Bastenaire 72].

A Wöhler curve presents 3 domains:

- Low-cycle domain. Under high loadings, the failure occurs after a few cycles ($N_R < 10^4$-10^5 cycles).
- Domain of limited endurance ($10^5 < N_R < 10^7$ cycles).
- Domain of endurance, also called domain of large number of cycles ($N_R > 10^7$ cycles).

The Wöhler curve presents generally a horizontal asymptote called fatigue limit, below which failure does not occur. However, gigacyclic mechanical tests call into question the existence of this limit [Mughrabi 99] [Mughrabi 06] [Stanzl-Tschegg 07].

In high cycle fatigue, the deformation is primarily elastic. This is the case for example in rotating or vibrating systems like wheels, axles and engine components. In low-cycle fatigue, macroscopic plastic deformation occurs every cycle and plays an important role.

I.2. STAINLESS STEELS AND AUSTENITIC STAINLESS STEELS

The material considered in this study is an AISI 316L austenitic stainless steel. Let us introduce first the stainless steel family and then the austenitic stainless steels.

I.2.1. STAINLESS STEELS

The inoxydability phenomenon of certain steels was discovered in the beginning of the 20th century. According to Castro [Castro 90], it is between 1904 and 1909 that the German Goldschmidt and the French Guillet and Portevin published their first works about steel grades with chromium. The corrosion resistance of these steels is due to the formation of an oxide layer of chromium protector at the surface of the alloy, called passivation layer. The chromium content must be at least 12 % in the alloy to produce this passivation layer.

At the beginning of the development of stainless steels, the discovery of the role of growing chrome additions on the resistance to the atmospheric and aqueous corrosion led naturally to the classification of stainless steels according to their corrosion resistance. Afterwards, other classifying parameters are considered. For example, stainless steels can be classified by their crystallographic structures, which depend on their compositions principally in Cr and Ni. Four families of stainless steels have been developed, classified according to their crystallographic structure:

- Martensitic steels.
- Austenitic steels.
- Ferritic steels.
- Austeno-ferritic steels, also called duplex.

Crystallographic structure can be predicted knowing chemical composition. Some alloying elements as Cr, Mo, Al stabilize the ferrite whereas other as Ni, C, N stabilize the austenite. The influence of the alloying elements on the final structure of the alloy can be expressed by the Schaeffler diagram (FIG. I.3) [Schaeffler 49], where chromium and nickel equivalents have been defined to take into account the content in alloying elements.

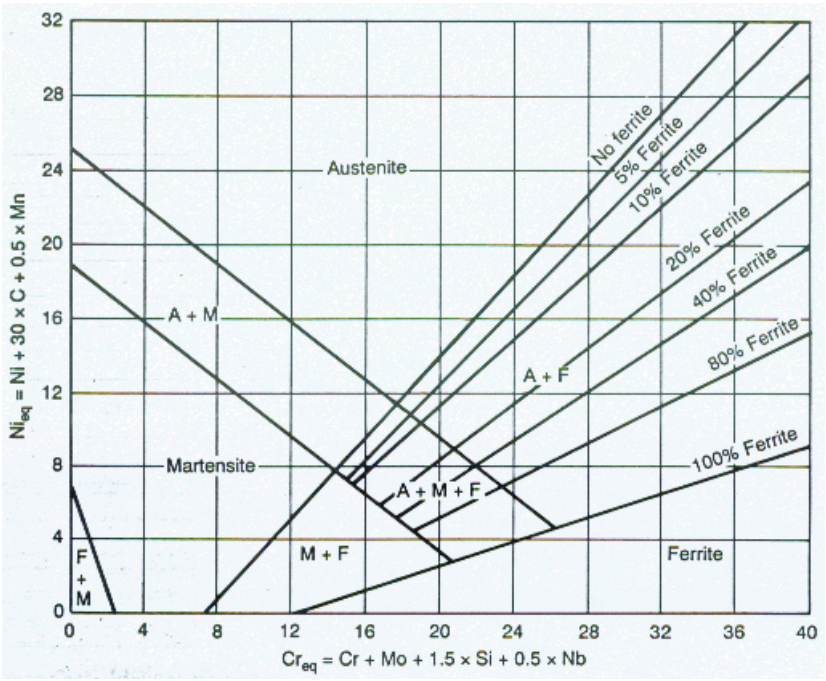

FIG. I.3 - Schaeffler diagram [Schaeffler 49].

I.2.2. AUSTENITIC STAINLESS STEELS

Austenitic stainless steels are widely used since the 1960s. They have a face-centered cubic (FCC) structure at room temperature. The chrome content (16-26 %) contributes to their inoxydability, and nickel content helps to form the austenitic structure (6-22 % in series AISI 300). Because of the cost of the nickel, it has been partly replaced by nitrogen and manganese in series AISI 200, as manganese helps nitrogen to be dissolved in the austenitic matrix and nitrogen stabilizes the austenitic structure. The content of nickel decreases then to 3.5-6 % in series AISI 200.

The thermal treatment generally used consists of keeping the material at around 1050 °C during one hour in order to put in solution all the alloying elements. The material is then water-quenched to keep the solid solution at room temperature.

Austenitic stainless steels have relatively weak mechanical characteristics (yield stress of about 250 MPa and ultimate tensile stress of about 550 MPa). The addition of atoms in interstitial solid solution, as carbon or nitrogen, leads to a distortion of the crystal lattice which highly hardens the material as interstitial solution atoms fix the edge dislocations [Cottrel 53] [Friedel 64]. A hardening of the material can also be obtained by cold hardening.

I.3. MECHANICAL BEHAVIOR UNDER CYCLIC LOADING

In the section below, the mechanical behavior of austenitic stainless steels will be analyzed and discussed under cyclic loading. Results obtained for austenitic stainless steels, especially for AISI 316L stainless steel will be presented, as this material is the subject of this study.

I.3.1. MECHANICAL TESTS

Cyclic mechanical tests provide information about stress-strain changes in the material studied during cycling. Various loadings can be tested, which can be uniaxial or multiaxial, tension (on cylindrical or flat useful part), torsion, internal pressure (on tubular useful part) or any combination of these loadings.

Servocontrolled machines allow to make precise control and measurements during mechanical tests. The working principle of a uniaxial servohydraulic machine is shown in FIG. I.4. A servo-valve controls electronically the movement of an actuator. The specimen is fixed between the actuator and the load cell. The section of the specimen's useful part has to be constant and its length has to be sufficiently large to assume that strains and stresses are uniform in the useful part (FIG. I.5). The specimens used during monotonic tensile tests and low-cycle fatigue tests are usually cylindrical in revolution, with smooth heads. The length/diameter ratio of the specimen for low-cycle fatigue tests must be low enough to avoid buckling in the useful part area and the connecting radius must be large enough to avoid crack initiation in the connecting areas.

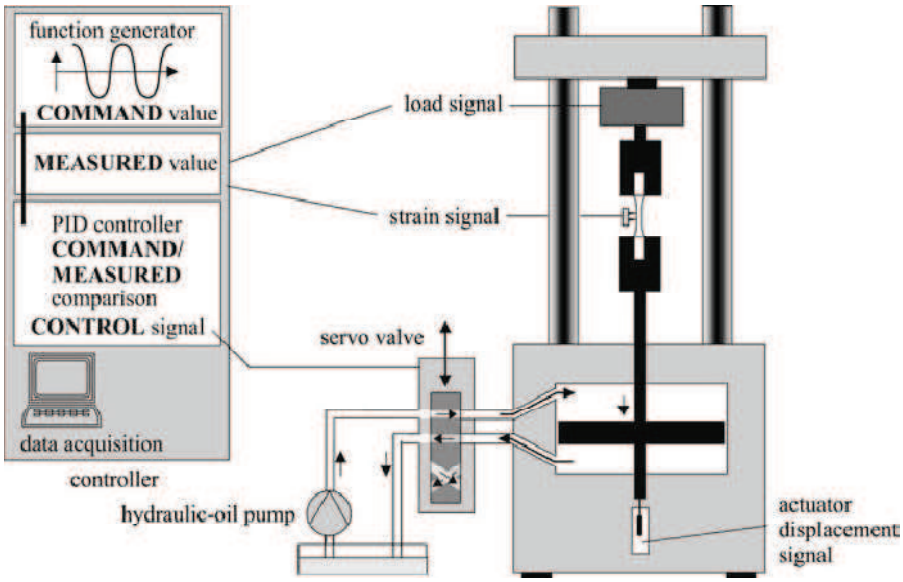

FIG. I.4 - Schematic representation of the working principle of servohydraulic test machines [Krupp 07].

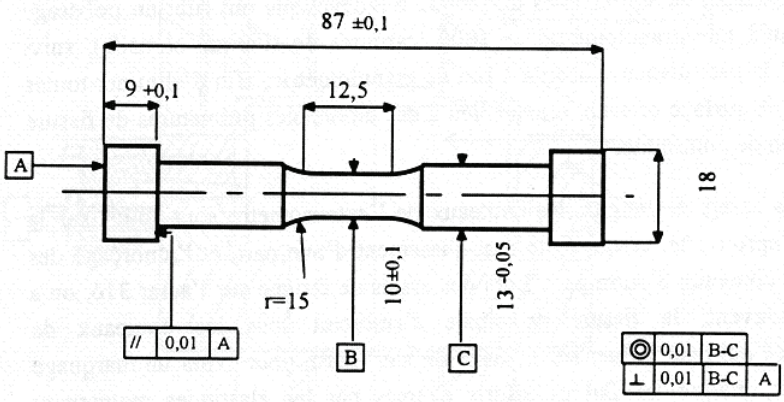

FIG. I.5 - Classical specimen sketch for fatigue testing [Moussavi 97].

Three signals are generally measured during the tests: the displacement of the actuator, the load applied to the specimen and the strain imposed to the specimen. The displacement of the actuator is measured through a linear variable differential transformer (LVDT) sensor. A load cell composed of a test body equipped with strain gauges allows to measure the load imposed to the specimen in real-time. The stress in the useful part of the specimen can then be deducted through the assumption of uniform state. Strains in the useful part of the specimen can be measured through three types of sensors: a gauge or an extensometer fixed on or attached to the specimen surface or, more recently, an optical system consisting in a camera filming the surface and a software of image analysis. In that case, marks or specks must be drawn on the specimen surface to allow following these marks during the deformation of the specimen [ASTM 02]. Several optical deformation measurement techniques, such as electronic speckle pattern interferometry (ESPI) [Robert 89], moire interferometry [Kafri 80] [Kafri 90] and digital image correlation method (DICM) [Peters 82] [Yamaguchi 81], have appeared with well-developed computer technology. The Digital Image Correlation Method (DICM) has been widely used in experimental mechanics in recent years. Not only the laser speckle pattern but also the natural texture or artificial pattern on the surface of the object can be used to determine the displacement of the object. Examples of use of DICM can be found in [Hild 02] [Lagattu 04] [Tao 05] [Roux 09].

These three strain sensors have their own advantages and disadvantages. A gauge is cheap and can be used for long-time tests and measurements in various directions. Whereas, it should be carefully oriented in order to get correct results. It has a temperature limit (< 200 °C) and cannot be reused for a second time. In certain testing environment (e.g. in acid solutions), it cannot be used. An extensometer is reusable, but as a gauge, it also has a temperature limit (< 1000 °C) and is not

suitable to certain testing environments. It is not capable for long-time tests, because its blades may glide on the specimen surface. As for an optical system, it has no temperature limit because there is no contract during measurement; it is reusable. However, this technique has limitations of time delay and precision in measurement. The most appropriate technique will change with loading conditions.

These three signals (displacement, load, strain) can all be used to control the machine. However, proportional-integral-derivative (PID) parameters must be adjusted to take into account the stiffness of the machine.

I.3.2. BAUSCHINGER EFFECT

The so called Bauschinger effect can be seen during the first loading cycle. After a first loading in tension, the material yields at a lower stress when the direction of loading is reversed than that for continued forward deformation [Bauschinger 86]. The yield stress in tension is then much larger than that in compression. FIG. I.6 shows the first hysteresis loop of a tension-compression test on an austenitic stainless steel AISI 316L [Choteau 99].

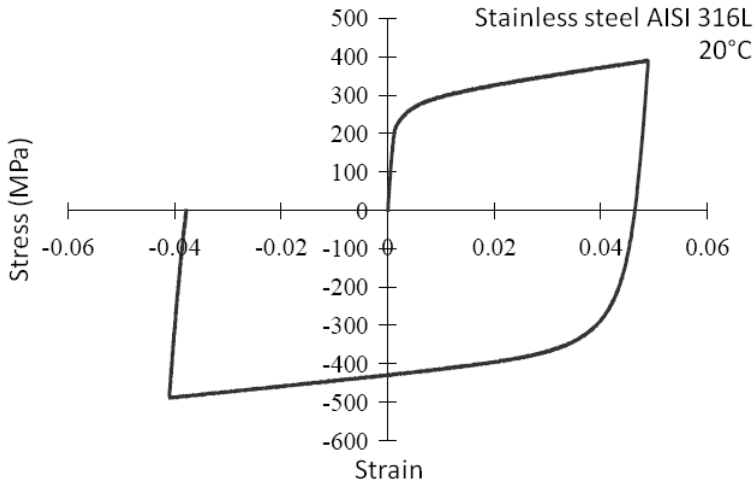

FIG. I.6 - First cycle of tension-compression of an austenitic stainless steel AISI 316L [Choteau 99].

I.3.3. MECHANICAL BEHAVIOR UNDER LOW-CYCLE PLASTIC FATIGUE

Studying the cyclic mechanical behavior implies to follow the stress amplitude changes during the cycling as a function of the imposed strain amplitudes. It is often possible to distinguish two stages of cyclic consolidation: a stage of rapid change of the stress amplitude, and a saturation stage during which the stress amplitude remains constant or almost constant. During the saturation stage, one

speaks of hardening if the stress amplitude increases during cycling, and of softening if the stress amplitude decreases. The stabilized cycle can be elastic, which is called adaptation, or plastic, one speaks of accommodation.

Cyclic hardening/softening behavior of austenitic stainless steels has been studied in [Degallaix-Moreuil 86] [Marchionni 96] [Obrtlík 94] among many others. For austenitic stainless steels, a hardening is observed in the early cycles. Higher the imposed strain amplitude, more evident the hardening. The hardening is followed by a quasi-stabilization of stress amplitude at average strain amplitude (lower than 0.8 %) [Zong 90] [Moussavi 97]. At high strain amplitude (1.3 %), the accommodation phase is followed by a quasi-stabilization phase, characterized by a slight hardening (FIG. I.7) [Moussavi 97]. The test ends with the fall of the stress amplitude due to the appearance of a crack. The crack propagation leads to specimen failure.

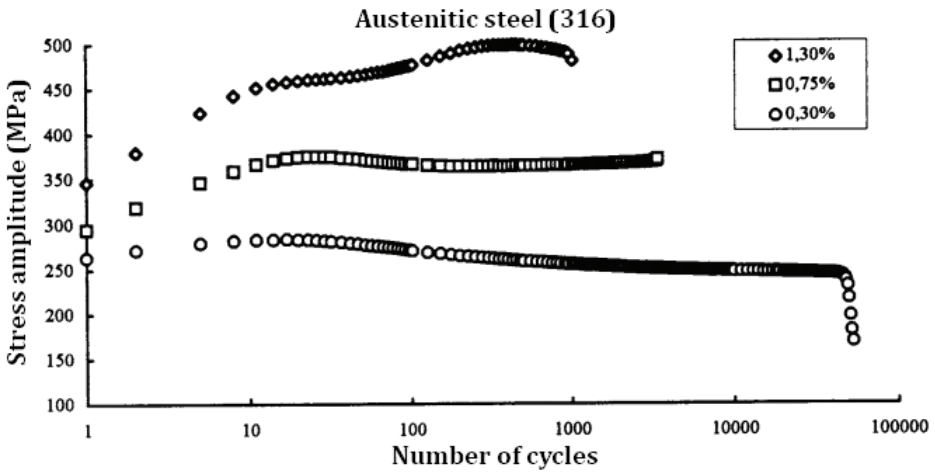

FIG. I.7 - Cyclic hardening/ softening curve of an austenitic stainless steel AISI 316L at 20 °C [Moussavi 97].

I.3.4. HYSTERESIS LOOPS

The hysteresis loop shows the relationship between stress and strain at various numbers of cycles. FIG. I.8 shows the stable hysteresis loops of an AISI 316L stainless steel under cyclic loadings at various strain amplitudes [Yang 04]. The Bauschinger effet is evident. At an imposed total strain amplitude of 0.2 %, the loop is almost closed. For the larger strain amplitudes, the loops open largely. Besides, it can be noted that as the strain amplitude increases, the residual strain at zero stress increases, too.

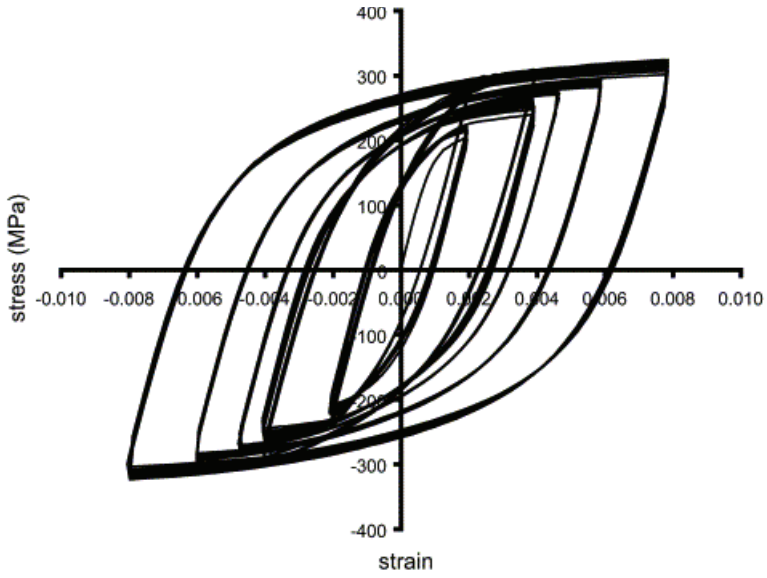

FIG. I.8 - Experimental hysteresis loops a 316L stainless steel under uniaxial tension-compression cyclic loads, at room temperature and with a strain rate of 2×10^{-3} s^{-1}. Total strain amplitude successively applied: ±0.20%, ±0.40%, ±0.47%, ±0.60%, ±0.80%, ±0.40%, ±0.20% [Yang 04].

I.3.5. FATIGUE LIFE

The fatigue life of a material can be analysed with a so-called Manson-Coffin curve. Manson-Coffin curve describes the relation between the number of cycles to failure and the imposed plastic strain amplitude. FIG. I.9 shows the Manson-Coffin curves for three 316L stainless steels with different nitrogen content (A < B < D < E) at room temperature [Vogt 84]. It can be seen that, for the four steels tested, the fatigue life decreases as long as the total strain amplitude increases and that these two values have a linear relationship in logarithmic coordinates. For a certain total strain amplitude (especially if $\varepsilon_t < 1$ %), $N_A < N_B < N_D < N_E$, which demonstrates that the addition of nitrogen will increase the fatigue life of austenitic stainless steels. However, saturation seems to occur when the nitrogen content is above 0.12 weight %. It should be mentioned that fatigue life depends not only on the material behavior, but also on the experimental conditions, e.g. temperature, environment, strain rate.

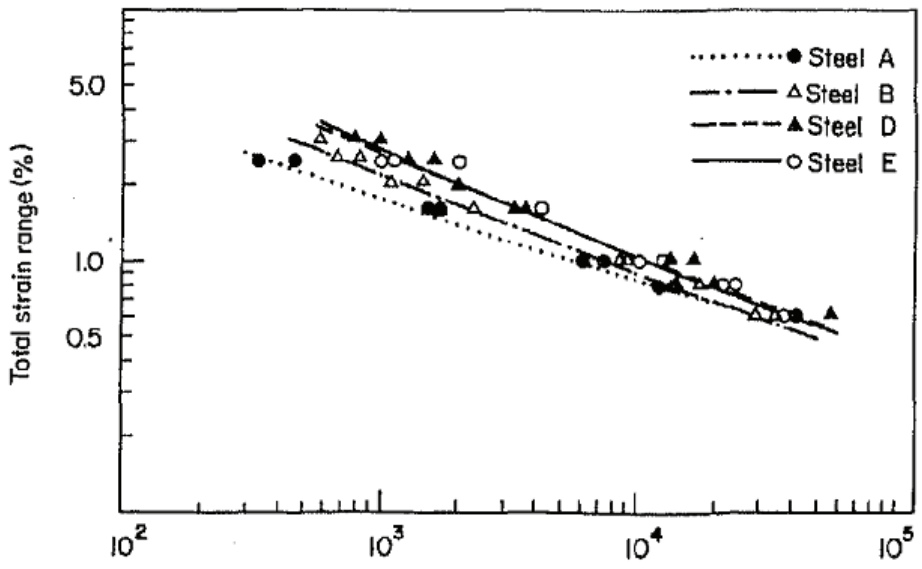

FIG. I.9 - Manson-Coffin curves for three 316L stainless steels with different nitrogen contents (A < B < D < E) [Vogt 84].

I.4. PLASTIC CRYSTALLINE BEHAVIOR

I.4.1. DISLOCATIONS - SOURCE OF PLASTICITY

Dislocations are linear defects in the crystalline structure. FIG. I.10 a) and b) presents the two types of elementary dislocations: edge dislocation and screw dislocation, depending on the orientation of the Burgers vector toward the displacement direction. Dislocations can be observed by means of six main methods, surface methods [Vogel 53] [Fisher 57], decoration methods [Amelinckx 58] [Amelinckx 64] [Humphreys 80], transmission electron microscopy [Lindroos 71] [Ray 71] [Howie 61], X-ray diffraction [Jenkinson 62], field ion microscopy [Melmed 96] and electron chanelling imaging [Gutierrez-Urrutia 09]. FIG. I.11 presents dislocation lines observed by transmission electron microscopy in a stainless steel. Dislocation slip can be regarded as sliding or successive displacement of one plane of atoms over another, which is called slip planes. Slip results in the formation of slip markings of extrusions and intrusions at the surface, some of these markings cannot be erased during cyclic loadings, they are named persistent slip markings. More details about the appearance of surface relief will be given below in section I.5.1.

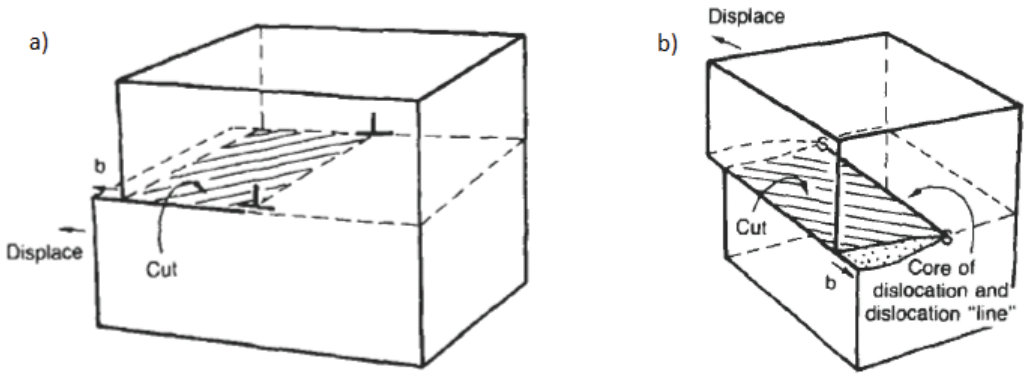

FIG. I.10 - Edge dislocation a) and screw dislocation b). The direction line represents the direction of the discontinuity line. b, Burgers vector, is the magnitude of the crystalline network defect [Ashby 96].

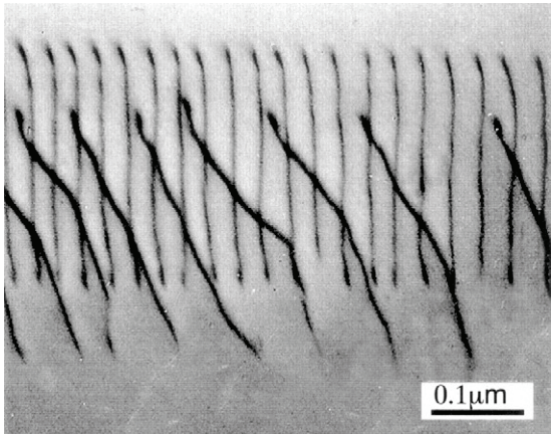

FIG. I.11 - Two parallel rows of dislocations presented by a thin film transmission electron micrograph [Hull 01].

The dislocation density represents the length of dislocations in a unit volume (m/m^3). It increases by plastic deformation due to the formation of new dislocations and dislocation multiplication, and can be removed by appropriate heat treatment (annealing).

I.4.2. STRESS AND STRAIN IN GRAINS AND SLIP SYSTEMS

The stress state in a given crystal of a polycrystal depends on parameters, on the one hand, internal to the crystal (such as crystallographic orientation, stacking fault energy, presence of hardening components as atoms in solid solution or precipitates…) and, on the other hand, external to the crystal (temperature, loading path, applied strain rate, position and location of other grains at the

boundaries…). FIG. I.12 shows the plastic strain field at the surface of a 3D polycrystal subjected to pure tension assuming a plastic crystalline behavior [Zeghadi 07]. Tension is applied along the y-direction. The stress field obtained at the free surface are compared assuming in the first case a pure elastic behavior with anisotropic elasticity and in the second case a crystalline plastic behavior with anisotropic elasticity. Stress distributions are heterogeneous in both cases. This heterogeneity is due to the strain incompatibilities between grains caused by the anisotropy of the elastic and plastic behavior. The stress distribution patterns are intimately related to the grain morphologies (grain size and grain shape) and to the grain orientations. In the next paragraphs, the influences of elastic anisotropy, grain orientation, grain size and shape will be discussed extensively.

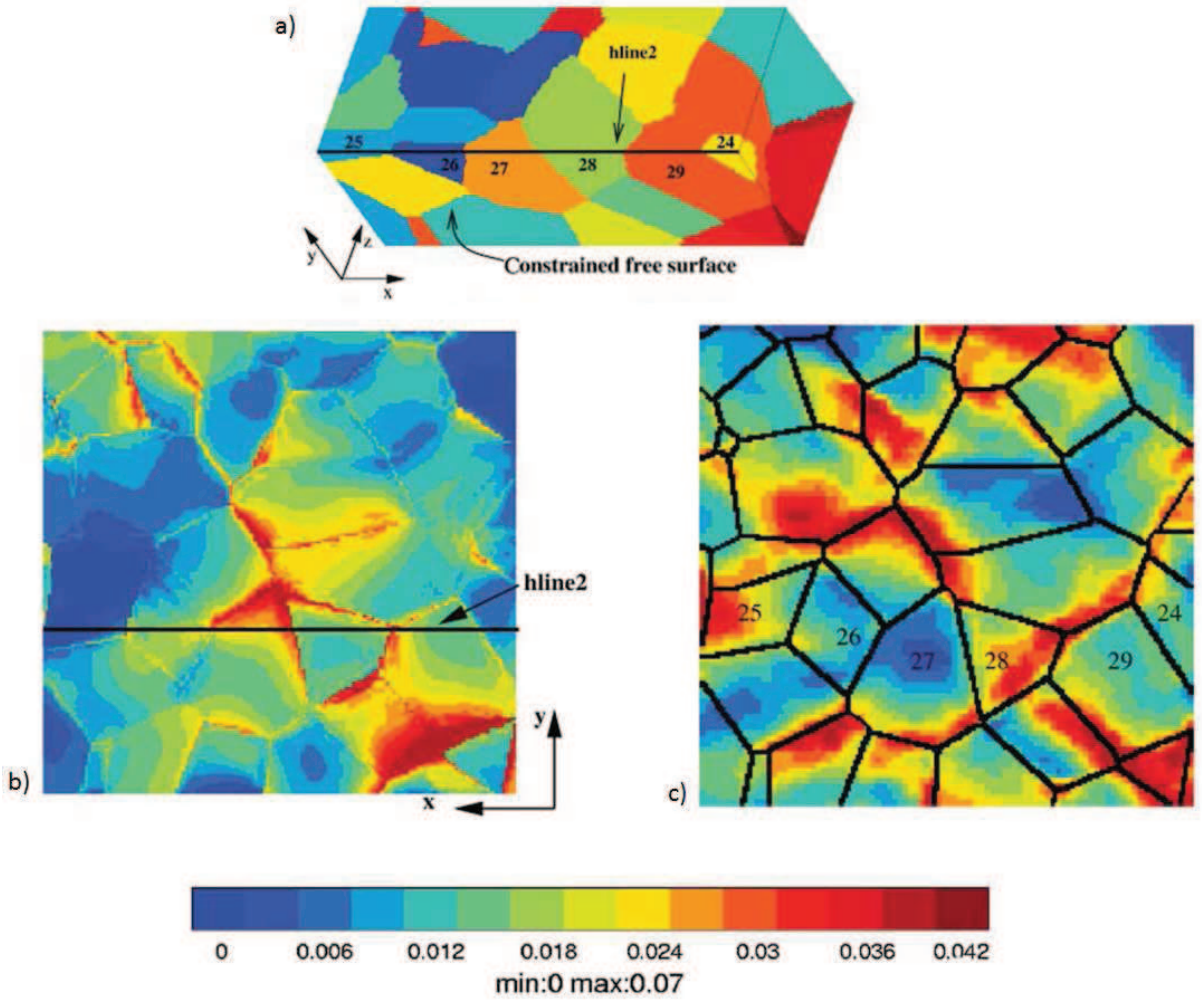

FIG. I.12 - Von Mises equivalent stress field at the surface of 3D polycrystal subjected to tension along y-direction: polycrystalline aggregate a); comparison between a pure anisotropic elastic behavior b) and an elastoplastic crystalline behavior c) [Zeghadi 07].

➢ ELASTIC ANISOTROPY

A anisotropic material does not have the same behavior in all the directions. Mechanical anisotropy of engineering materials may result from oriented internal structures at different scales. Anisotropy may be inherent due to the elaboration process where specific directional properties are designed or naturally produced as for instance in the case of composites, foams, powders, multiphase solids, and most geomaterials. On the other hand, anisotropy may be induced by loadings, giving rise to various types of damage, as for instance in the case of concrete and highly deformed metals [Bigoniand 99]. The influence of the spatial heterogeneity of elastic properties on the inception of plasticity has been first brought to light qualitatively by slip trace analysis in bicrystals [Hook 67] and in polycrystals [Hashimoto 83a, b]. The link between the single crystal elastic anisotropy and the onset of yielding in polycrystals has been first studied within the homogenization framework by [Hutchinson 70].

The rigidity tensor (4th order) permits to express the crystalline elastic behavior. It links the tensors of stress and strain in the elastic domain in the following way: $\underline{\underline{\sigma}} = \mathrm{C}\underline{\underline{\varepsilon}}$ or $\sigma_{ij} = \mathrm{C}_{ijkl}\varepsilon_{ij}$ in indicial writing. In general, the tensor rigidity is composed of 21 independent coefficients. Face-centered cubic (FCC) material have a cubic symmetry, and present then orthotropic elasticity. In this case, the rigidity tensor is composed of only three independent coefficients: C_{11}, $\mathrm{C}_{12}$and C_{44}. The tensor C is then written as:

$$\begin{pmatrix}\sigma_{11}\\ \sigma_{22}\\ \sigma_{33}\\ \sigma_{12}\\ \sigma_{23}\\ \sigma_{31}\end{pmatrix} = \begin{pmatrix}\mathrm{C}_{11} & \mathrm{C}_{12} & \mathrm{C}_{12} & 0 & 0 & 0\\ \mathrm{C}_{12} & \mathrm{C}_{11} & \mathrm{C}_{12} & 0 & 0 & 0\\ \mathrm{C}_{12} & \mathrm{C}_{12} & \mathrm{C}_{11} & 0 & 0 & 0\\ 0 & 0 & 0 & \mathrm{C}_{44} & 0 & 0\\ 0 & 0 & 0 & 0 & \mathrm{C}_{44} & 0\\ 0 & 0 & 0 & 0 & 0 & \mathrm{C}_{44}\end{pmatrix}\begin{pmatrix}\varepsilon_{11}\\ \varepsilon_{22}\\ \varepsilon_{33}\\ 2\varepsilon_{12}\\ 2\varepsilon_{23}\\ 2\varepsilon_{31}\end{pmatrix} \quad \text{(I-1)}$$

The anisotropy is characterized by the coefficient of anisotropy:

$$\mathrm{a} = 2\frac{\mathrm{C}_{44}}{\mathrm{C}_{11}-\mathrm{C}_{12}} \quad \text{(I-2)}$$

TAB. I.1 presents the elastic rigidity coefficients and the anisotropy coefficient of several materials. The more the elasticity is anisotropic, the more the value of the anisotropy coefficient is far from 1. The austenitic steel, referenced as $\mathrm{Fe}\,\gamma$, is highly anisotropic, with an anisotropy coefficient of 3.4. This value is close to the ratio of maximal longitudinal elastic modulus E_{max} (direction <111>) and minimal modulus E_{min} (direction <100>). This means that under the same loadings, in the direction corresponding to E_{max}, the grain has a deformation three times less than that in the direction corresponding to E_{min}.

Material	C_{11} (10^9 Pa)	C_{12} (10^9 Pa)	C_{44} (10^9 Pa)	a	E_{max}/E_{min}
Isotropic	-	-	-	1	1
Al	107	60.8	28.3	1.2	1.17
Fe α	247.7	144.6	118	2.5	2.5
Cu	170	124	75	3.3	3
Fe γ	197.5	125	122	3.4	2.96

TAB. I.1 - Coefficients of the elastic rigidity matrix C_{ij}, anisotropy coefficient and ratios of Young's modulus of some metals at room temperature [Huntington 58].

Osterstock showed that the anisotropy of crystalline elasticity has a great influence on high cycle fatigue, when plastic strain is very limited [Osterstock 08]. However, in low cycle fatigue, its influence is negligible, the plastic behavior is the main cause of the stress-strain field heterogeneities.

➢ VARIATION OF THE CRYSTAL ORIENTATION FROM GRAIN TO GRAIN

The question of the effect of crystal orientation on the stress-strain behavior has first been addressed analytically, initially by [Schmid 50] and more recently by [Kocks 98] using crystal plasticity simulations and texture analyses. Various experiments have been carried out on single FCC crystals to analyze orientation effects: simple shear [Kochendorfer 50], direct shear [Phillips 62] and cyclic tension-compression tests with different crystal orientations (e.g. [Mughrabi 78] [Jin 84] [Li 99a]). A summary of early experimental results on FCC single crystals as a function of orientation can be found in [Nabarro 64].

Modifying the orientation of a single crystal will change its yield strength and flow stress as observed during tests of tension, compression or channel die compression of single crystals at quasi-static strain rates on the order of 10^{-4}-10^{-2} s^{-1} (e.g. [Lange 53] [Haasen 58] [Driver 94]). Similar effects were observed in shock recovery experiments with high strain rates on the order of 10^5 s^{-1} [Follansbee 91].

The crystal orientation will also influence the cyclic behavior and the dislocation configuration. Li *et al.* [Li 99a, b] [Li 01] summarized the plateau in the CSS curves of copper single crystals of different orientations. As shown in FIG. I.13a, the CSS curves show significant difference with variations in orientation, which can be specially introduced as follows: (1) a similar saturation plateau behavior is apparent for single, conjugate double and [011] multiple slip oriented copper single crystals; (2) coplanar double, critical double and [001] multiple slip oriented copper single crystals have higher CSS curves without plateau regions. Dislocation configurations of copper single crystals with various

orientations are illustrated in the stereographic triangle in FIG. I.13b. The classical PSB ladder structure appears in copper single crystals with single, conjugate double and [011] multiple slip orientations. As the orientations of copper single crystals change from [011] to [001] in the stereographic triangle the corresponding dislocation patterns vary from PSB ladders to a labyrinth structure. When the orientation changes from [011] to [-111] PSB ladders will be gradually converted into a cell-like structure.

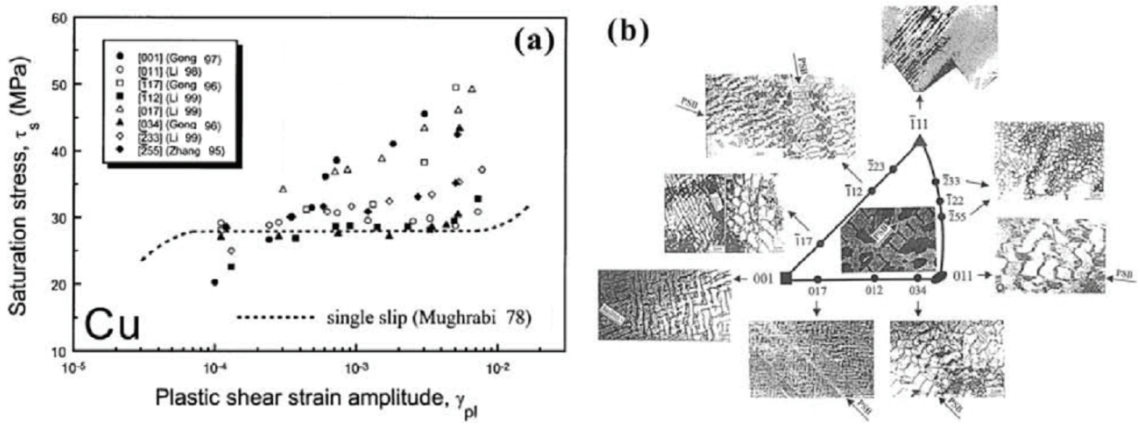

FIG. I.13 - CSS curves and dislocation configurations of copper single crystals with different orientations [Li 99a, b] [Li 01].

➢ GRAIN SIZE AND SHAPE

Hall [Hall 51] and Petch [Petch 53] found independently that the yield strength in mild steel varies with the inverse square root of grain size as

$$\sigma = \sigma_0 + \mathrm{k}\mathrm{d}^{-1/2} \tag{I-3}$$

where d is the mean grain size, σ_0 is the yield stress in the imaginary situation with infinitely large grains, and k is a material constant.

Armstrong *et al.* [Armstrong 62] showed experimentally that for a number of metallic polycrystalline aggregates the flow stress at constant strain is related to the grain size, d, by the same form as the Hall-Petch relationship between yield strength and grain size, i.e. σ, σ_0 and k are functions of the strain. For much smaller sizes, on the order of nanometers, Horstemeyer and Baskes [Horstemeyer 99] have shown using the embedded atom method (EAM) that global yield and plastic flow are size dependent.

Several models have been proposed to account for the grain size dependency. One theory is that grain boundaries act as obstructions to dislocation motion and therefore dislocations pile-up at grain boundaries giving rise to stress concentrations. Another model based on work hardening assumes an inverse relationship between dislocation density and grain size. A theory that supports the work hardening model was proposed by Ashby [Ashby 70] arguing that an increase with strain in the density of geometrically necessary dislocations at a grain boundary affects the work hardening of polycrystals.

Classical crystal plasticity formulations like [Peirce 83] do not include any material length scales in the constitutive equations, and therefore they cannot capture the experimentally observed grain size effects. Within recent years several non-local crystal plasticity formulations have been proposed. Some of these formulations are based on strain gradient plasticity theories that make use of an internal material length scale parameter [Shu 99] [Borg 06]. Other non-local formulations are continuum theories of dislocations [Acharya 00] [Gurtin 02] [Han 05] [Evers 04] [Kuroda 06]. Grain size effects in polycrystals have been predicted with such crystal plasticity formulations by [Acharya 00] [Ever 04] [Schwartz 10]. Furthermore, discrete dislocation plasticity models have been used to analyze grain size strengthening in the work of [Biner 02] and [Balint 05].

The grain shape effect can be studied by means of the aspect ratio α (α= a/b where a and b are the half-axes of the grain). In the research work of Radi and Abdul-Latif [Radi 09], three values of α, 0.75, 1.25 and 75, were chosen. Their influence on the macroscopic strain-stress response was studied using a self-consistent approach in monotonic tension. The simulations show a remarkable sensitivity to the aspect ratio as shown in FIG. I.14. Moreover, Mura carried out a systematical theoretical study on isotropic and anisotropic inclusions of different shapes (spherical, ellipsoid, plate, cylinder …) [Mura 87]. Studies have also been carried out on the effects of grain shape on the slip system activity and on the lattice rotations [Tiem 86], on yield strength anisotropy [Cho 99], on residual stresses [Kreher 93].

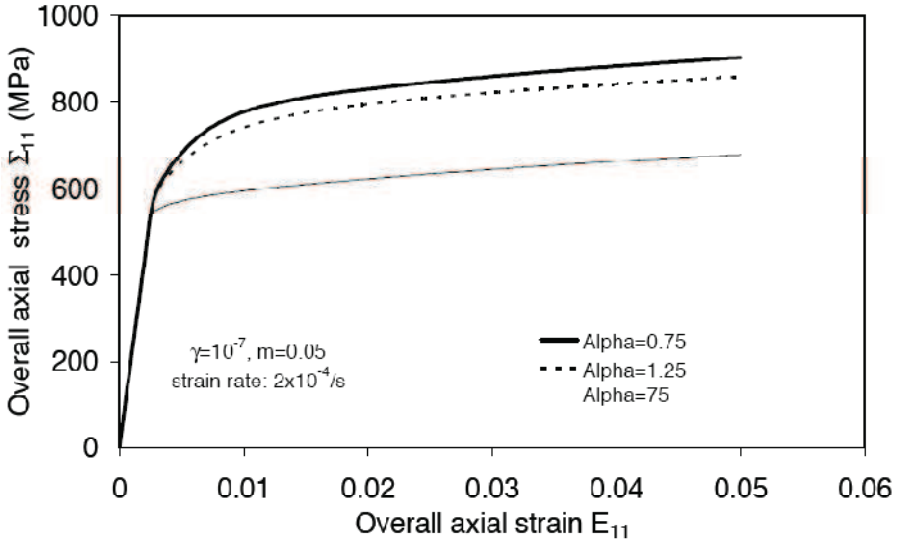

FIG. I.14 - Grain shape effect on the macroscopic stress-strain curve [Radi 09].

I.5. CRACK INITIATION

I.5.1. RELIEF APPEARANCE AND PERSISTENT SLIP BANDS

Even in the case of idealized materials, having no defects, no precipitates and no grain boundaries, and being perfectly polished, cyclic deformation will lead sooner or later to crack initiation, provided some infinitesimal amount of localized irreversible plastic slip is present.

The pioneering work on the nature and physical mechanisms of fatigue damage evolution started more than 100 years ago. In 1903, Ewing and Humfrey [Ewing 03] first presented optical microscopic observations of the surface of flat specimens of polycrystalline Swedish iron, fatigued in rotating bending. They observed localized cyclic slip in surface grains and formation of surface markings. They observed also that fatigue cracks appeared in the rough surface relief. After that, the discovery of extrusions [Forsyth 53], intrusions [Hull 55] [Cottrell 57] [Forsyth 53], persistent slip bands [Thompson 56], dislocation structure of persistent slip bands [Laufer 64] [Laufer 66] [Lukáš 68] and its relation to sharp surface slip markings [Atkinson 73] contributed to the identification of the mechanisms of surface relief formation.

FIG. I.15 describes the steps of formation of relief on surface, which contributes to crack initiation. Slip occurs first in a grain having the conditions more favorable. Once a slip occurs in a grain, a slip step will be created at the material surface, where fresh metal surface is exposed to oxygen from the

environment [Thompson 56] [Krupp 07], see FIG. I.15a. Absorption of oxygen impedes complete reversibility of gliding. Upon unloading, the reversed slips will occur in the adjacent parallel slip planes, as shown in FIG. I.15b. As the process of loading-unloading continues, the same sequence happens again in the second cycle (FIG. I.15c and d). Slip marks appear at the surface of the specimen. During the cyclic loadings, intrusions and extrusions will appear at the surface, as seen in FIG. I.15e. Beside the environmental effect, cyclic slip irreversibility can be attributed to mutual interactions between dislocations. The dynamic equilibrium between dislocation multiplication by the Frank-Read mechanism and the annihilation of screw and edge dislocations especially in persistent slip bands (PSBs) leads to the generation of vacancies, which eventually cause macroscopic roughness along the intersection lines between PSBs and originally polished specimen surface [Lukáš 96] [Differt 86].

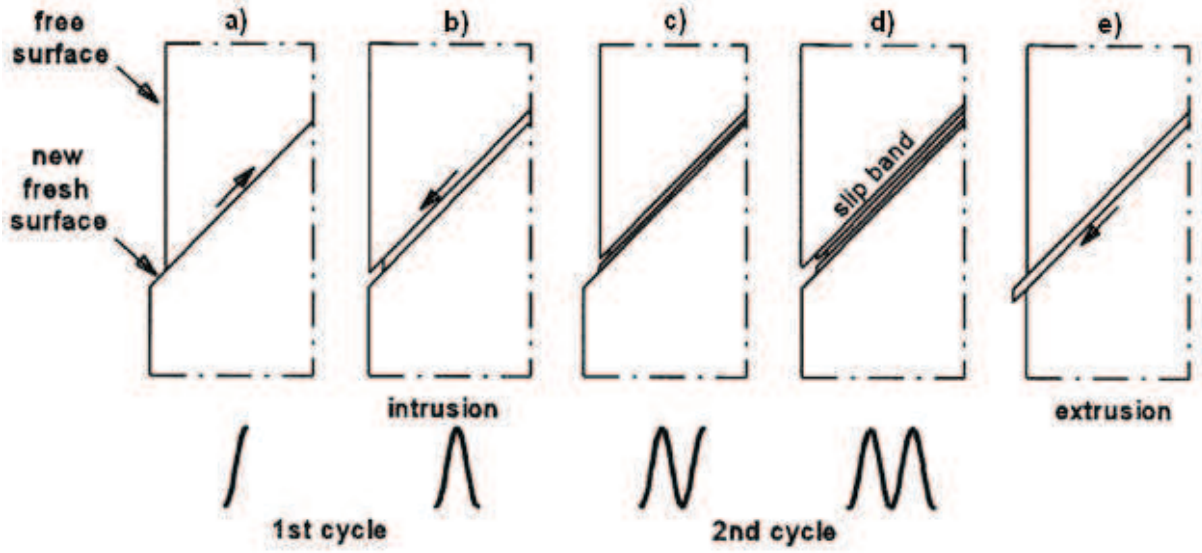

FIG. I.15 - Schematic description of mechanisms of crack nucleation from plastic activity [Schijve 09].

Cyclic plastic strain localization in persistent slip bands (PSBs) is now accepted as a general and very important feature of cyclic straining in crystalline materials, which can be regarded as the first sign of fatigue damage [Polák 03] [Lukáš 04] [Laird 96] [Suresh 98] [Lukáš 01] [Mughrabi 01]. The phenomenon of PSBs was discovered by Thompson *et al.* [Thompson 56], who revealed that the locations of the bands at the surface of the specimen remained visible after electro-polishing. The structure of PSBs was then identified using transmission electron microscopy [Laufer 64] [Laufer 66] [Lukáš 68] [Atkinson 73], and their specific dislocation arrangement was described in [Laird 86] [Polák 03] [Lukáš 04] [Laird 96] [Suresh 98] [Lukáš 01] [Mughrabi 01].

FIG. I.16 presents a scheme a persistent slip band. Where the PSB intersects the free surface, a persistent slip mark appears [Man 09]. Dislocation distributions in PSB with a so-called ladder structure embedded in the matrix with a vein structure are indicated schematically according to Essmann *et al.* [Essmann 81]. However, the classic "ladder" structure indicated in FIG. I.16 is not the only internal structure observed in PSBs (compare e.g. [Polák 03] [Lukáš 04]). The dipolar nature of the walls in PSB is highlighted in agreement with Antonopoulos *et al.* [Antonopoulos 76]. Within the PSBs, dislocation annihilation will occur and lead either to the formation of vacancies or interstitials [Essmann 81]. Due to their mutual repulsion, the increase in the interface dislocation density gives rise to the establishment of internal compressive stresses within the PSB. These compressive stresses are superimposed to the applied remote stress σ_a and lead to tensile stress peaks at the flanks of the PSB at the specimen surface. Ma and Laird [Ma 87] [Ma 89] showed for cyclically deformed copper single crystals that crack initiation takes place at the flanks of the PSB at the specimen surface (see FIG. I.17).

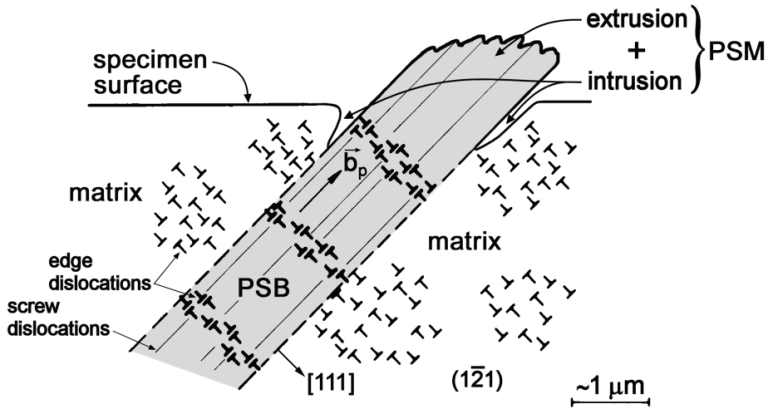

FIG. I.16 - Scheme of appearance of persistent slip bands [Man 09].

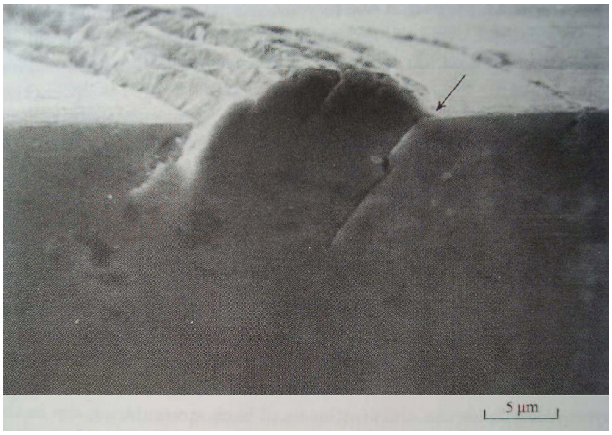

FIG. I.17 - Fatigue crack initiation at a PSB-matrix interface in a Cu crystal fatigued for 60 000 cycles at γ_{pl} = 0.002 at room temperature [Ma 89].

I.5.2. LOCATION OF CRACK INITIATION

At room temperature and in low-cycle fatigue, there are different locations of crack initiation:

- Some cracks initiate in persistent slip bands (PSB). These cracks are called transgranular cracks (see FIG. I.18a).
- Some cracks initiate in grain boundaries. They are called intergranular cracks (see FIG. I.18b).
- Some cracks initiate in twin boundaries (see FIG. I.18c).

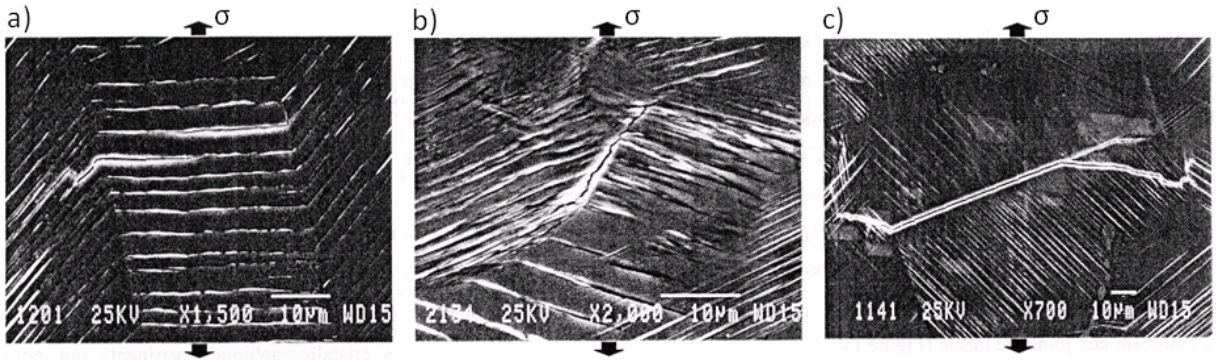

FIG. I.18 - a) Transgranular crack (at 5000 cycles in air), b) intergranular crack (at 15000 cycles in vacuum), c) crack initiated at twin boundaries (at 12500 cycles in air). $\Delta\varepsilon^p/2 = 2 \times 10^{-3}$, 20 °C [Mineur 00b].

In air and at room temperature, the cracks observed in a stainless steel AISI 316L are mainly transgranular cracks (75%) under a plastic strain amplitude $\Delta\varepsilon_p/2$ of 2×10^{-3} after 5000 cycles, which represent about 20 % of the life, see FIG. I.19 [Mineur 00b].

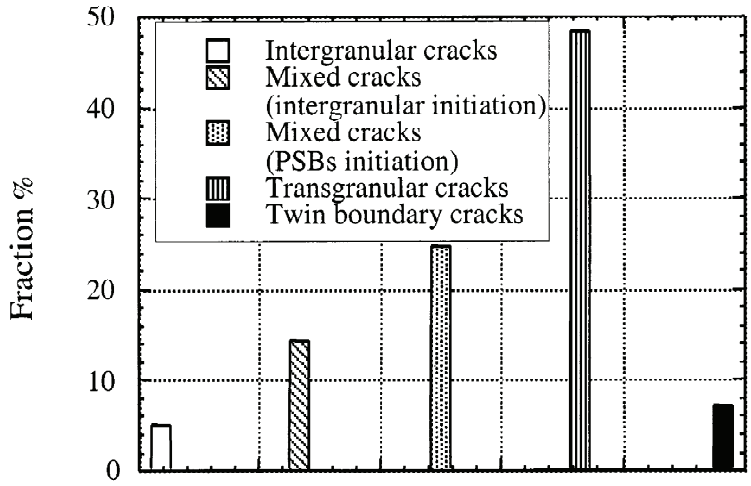

FIG. I.19 - Distribution of the initiation sites of cracks (air, AISI 316L, $\Delta\varepsilon_p/2 = 2 \times 10^{-3}$, 5000 cycles) [Mineur 00a].

The distribution of these various types of cracks depends not only on the material behavior, but also on the test conditions: stress amplitude, temperature, surface and environment. In the next sections, these influence factors will be successively introduced.

I.5.3. Influence of stress amplitude

The influence of stress amplitude was first studied for single-crystalline copper and nickel and was then broadened to technical polycrystalline materials.

Investigations on polycrystalline copper by Figueroa and Laird [Figuera 83] and Kim and Laird [Kim 78a] revealed that for moderate strain amplitudes, transgranular cracks initiate at the intersection points between PSBs and grain boundaries. Heinz and Neumann [Heinz 92] revealed that under low stress amplitudes, microcracks initiate principally in twin boundaries or in slip bands. At higher strain amplitudes and for a correspondingly higher volume fraction of PSBs, the high number of slip steps, reaching heights up to 1 µm along the grain boundaries, promotes intergranular crack initiation [Kim 78a, b]. This was supported by transmission electron microscopy studies of Huang and Ho [Huang 00], who found protrusions along the PSB-grain boundary interfaces. However, for high strain amplitudes, they reported crack initiation at grain boundaries without PSB interactions, but accompanied by pronounced formation of dislocation cell structures. The appearance of cell structures is an indication of uniform strain within the respective grains, causing relative displacements from grain to grain and, eventually, the formation of transgranular cracks emanating from the grain boundary.

I.5.4. Importance of surface roughness

In technical components, the typical initiation sites for fatigue cracks are notches, either given by engineering design or due to surface roughness caused by machining. The influence of such notches of various radii on the initiation and propagation or non-propagation of microstructurally short cracks was studied by Vallellano *et al.* [Vallellano 00a, b] by means of a micromechanical model. Andrews and Sehitoglu [Andrews 00] showed by experimental studies on 4340 steel that the influence of surface roughness becomes the key factor when the mean surface roughness R_a exceeds the diameter of intrinsic material defects or the grain size. Wareing and Vaughan [Wareing 79] examined three surface finishes with grooves ranging from 0.1 mm to 4 mm in type 316 stainless steel. They concluded that the fourfold reduction in fatigue life resulted from a difference in nucleation sites and the resulting shape of the cracks as they interacted with each other. Fluck [Fluck 51] examined the effects of roughness and the effects of the direction of the scratches. He found that longitudinal scratches had little effect, even if they were large.

In order to reduce the risk of promoting crack initiation at the surface, many high-stressed components are surface treated by means of, for example, shot peening, tensile pre-stressing, roller hardening or laser-shock peening. The compressive residual stresses in the surface layer, resulting from such kinds of surface treatments, reduce the crack-driving effect of applied remote tensile stresses in the surface layer.

I.5.5. INFLUENCE OF RESIDUAL STRESS

Residual stress refers to a stress distribution, which is present in a structure, component, plate or sheet, while there is no external load. Under fatigue loading, residual stresses play the role of internal loading and are superimposed to the external loading. Therefore, in general, residual stresses affect fatigue behavior in the same way as an applied mean stress. In crack initiation dominated situations residual stresses at a surface are favorable if compressive, but detrimental if tensile [Pook 07]. Almer [Almer 00] used the combined techniques of X-ray diffraction and Finite Element analysis to analyze fatigue crack initiation in the presence of residual stresses. The author showed that the residual macrostresses relaxed less rapidly than the residual microstresses employed along with mechanical tests and can strongly affect crack initiation behavior.

In order to increase fatigue resistance, compressive residual stresses are often purposely introduced around these concentrators through processes such as shot-peening [Underwood 95], press-fitting [Underwood 95] [Edwards 92] [Lai 93], and tensile pre-straining [Underwood 95] [Mowbray 73] [Aswath 88].

I.6. CRACK PROPAGATION

Once initiated, cracks propagate first on surface, then deep into the bulk (FIG. I.20). The crack will have to cross the microstructural barriers as the grain boundaries, the twin boundaries or the precipitates. If the crack succeeds in crossing the first few grains, it will then reorient perpendicularly to the direction of the principal stress. The crack is then said microstructurally long and the law of Paris [Paris 63] can be applied to predict its propagation rate. Magnin classified the cracks observed in an austenitic stainless steel of type AISI 316L (grain size $\overline{d}$ = 50 µm) under uniaxial fatigue stress, at 20 °C, into 4 categories, according to the relation between their lengths and the grain size [Magnin 84]. Type I cracks have a length less than the grain size. Type II cracks cross one or two grain boundaries. The propagation of cracks of types I and II is governed by the microstructural and crystallographic aspects. They propagate mainly along the persistent slip bands in surface grains.

Type III and IV cracks propagate perpendicular to the direction of maximum principal stress, according to Paris law. Bataille *et al.* [Bataille 94] studied the evolution of the density of cracks of type I, II and III in function of their length during the cycling, in a 316L stainless steel under a plastic strain amplitude of 4×10^{-3} (FIG. I.21). At the beginning of the cyclic saturation, cracks of type I germinate along the slip bands. Then, these cracks micro-propagate and coalesce, leading to cracks of type II, then of type III. During all this time, germination, micro-propagation and microcoalescence still go on. Finally, the coalescence of cracks of type III and their propagation lead to the apparition of one or two cracks of the order of millimeter, namely crack of type IV which causes the ruin of the specimen.

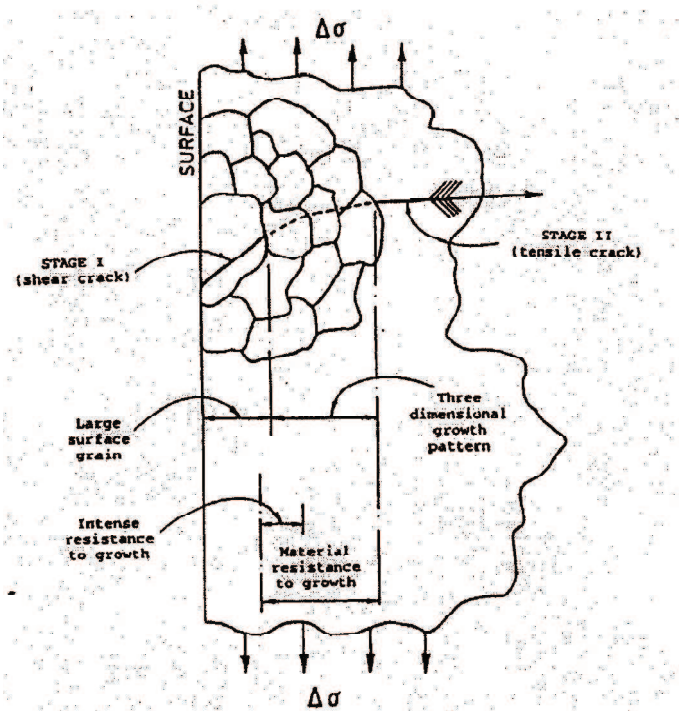

FIG. I.20 - Different stages of cracking under isothermal uniaxial cyclic loading of tension-compression [Miller 97].

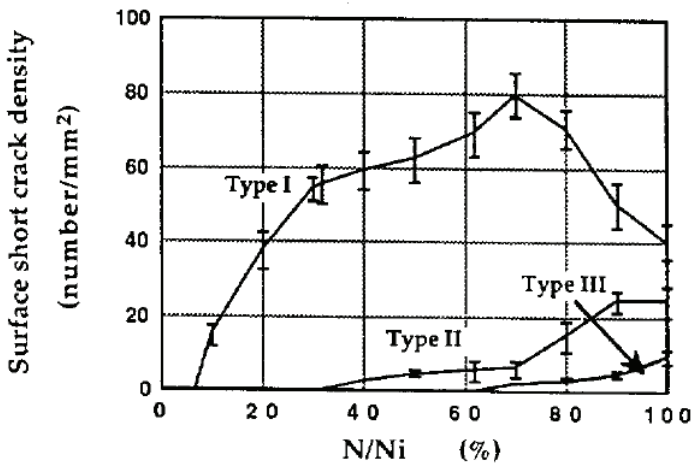

FIG. I.21 - Evolution of the density of cracks in function of their length during the cycling at $\Delta\varepsilon_p/2 = 4 \times 10^{-3}$, N_i = 7500 cycles (about 90 % of N_R), $\dot{\varepsilon} = 10^{-3}$ s^{-1} [Bataille 94]. Each of the 3 curves corresponds to the density of cracks of a given type (I, II and III).

I.7. CONCLUSION

After a brief presentation of the material studied here, we presented its mechanical behavior under cyclic loading. Although the mechanical behavior is homogeneous at a macroscopic scale, it is obviously not the case at the grain scale. The effects of various parameters on local stress and strain heterogeneities have been discussed: anisotropic elasticity, crystal orientations, grain sizes and grain shapes. This stress/strain localization will obviously favor crack initiation. The mechanism of crack initiation due to plastic activity in persistent slip bands has been described. Data from the literature concerning the influence of the loading and surface on crack initiation have also been reported.

II. MECHANICAL CHARACTERIZATION OF THE STUDIED STEEL

In this chapter, we present the low-cycle fatigue tests carried out on an austenitic steel in the context of this work and their results. These tests should enable us to characterize the behavior of the austenitic steel under cyclic loading. They will then allow us to identify and validate various constitutive laws selected in the literature (see Chapter III).

We first describe the studied material (section II-1), the equipment and the experimental procedures used (section II-2). The experimental results are then presented and analyzed in section II-3. We finally analyze the monotonic tensile behavior of the steel studied (section II-3.2), and its uniaxial low-cycle fatigue behavior (section II-3.3).

II.1. STUDIED MATERIAL

The material studied is an austenitic stainless steel Z2CND17-12 (AISI 316L). Its chemical composition is given in TAB. II.1. Elements present in very small amount could not be measured. The material was supplied in a plate of 14 mm thickness. After being rolled, the plates have been solution treated for one hour and then water-quenched. All alloying elements have been put in solid solution. The microstructure obtained is given in FIG. II.1. The studied material has an average grain size, determined using software OIM, of 50 microns. The microstructure is similar in the 3 directions of the plate and the material has a globally isotropic microstructure.

C	Cr	Ni	Mo	Mn	Si	P	Fe
≤0.030	18.51	12.85	2.15	1.50	0.71	≤0.045	bal.

TAB. II.1 - Chemical composition of the stainless steel studied.

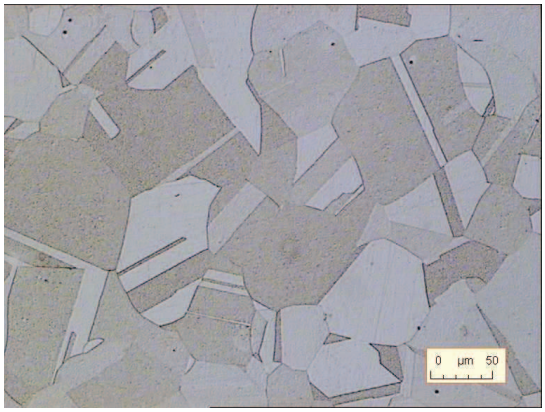

FIG. II.1 - Microstructure of the studied austenitic stainless steel, observed by optical microscope.

II.2. EXPERIMENTAL METHODS

II.2.1. TESTING MACHINE

FIG. II.2 shows the uniaxial testing machine used. This is a servo-hydraulic INSTRON machine of type 8501. It is equipped with a load cell of capacity ± 100 kN. The movement of the actuator can be controlled in displacement, load or strain. The control and data acquisition were carried out using programs developed in the laboratory with software LabVIEW [Aubin 01]. Fatigue tests were performed at room temperature (20 °C) and in air. The tension/compression tests were carried out under total strain control, which is measured by an extensometer with a gauge length of 10 mm and a capacity of ± 10 %. The measurement of the longitudinal movement of the actuator was done using a sensor LVDT of capacity ± 75 mm. The load and strain were recorded simultaneously at imposed frequency during cycling.

FIG. II.2 - Uniaxial fatigue testing machine.

II.2.2. SPECIMENS

The testing specimens were cylindrical with smooth heads. Their useful part had a diameter of 10 mm and a length of 30 mm (FIG. II.3, b and c). This length is larger than the gauge length (10 mm), which allows to have an area of about 20-25 mm long in which the strain is homogeneous. 4 specimens were machined from the plate with a 14 mm thickness (FIG. II.3d): 1 for a monotonic test and 3 for cyclic tests. The specimens were taken in the plate parallel to the rolling direction. Since the thickness of the plate is smaller than the diameter of the specimen heads, the heads were truncated (FIG. II.3).

The specimens were fixed on the testing machine using the grips shown in FIG. II.4.

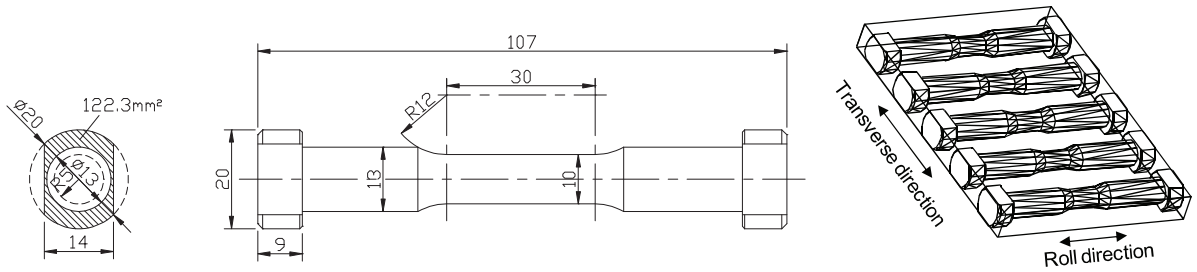

FIG. II.3 - a) Sketch of the testing specimen, b) location of the specimens in the plate.

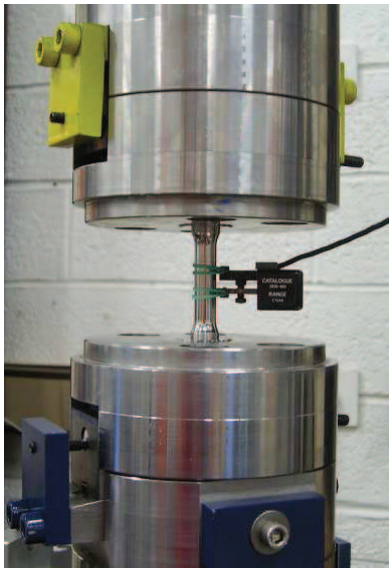

FIG. II.4 - Tension-compression grips.

II.2.3. PRESENTATION OF THE REALIZED TESTS

All tests were performed at imposed total strain and a constant total strain rate of 6.6 10^{-4} s^{-1}. The temperature was 20 °C. The monotonic tension test was performed up to 8 % of total strain. The three cyclic tests were performed with strain amplitudes ε_a of 0.3 %, 0.5 % and 0.8 % up to 1000 cycles. According to the statistical model developed in the Argonne National Laboratory of U. S. [ANL 05], the fatigue lives of wrought and cast austenitic stainless steels can be calculated through the equation below:

$$\ln(N) = 6.703 - 2.030\ln(\varepsilon_a - 0.126) \quad \text{(II-1)}$$

For the strain amplitudes ε_a of 0.3 %, 0.5 % and 0.8 %, the fatigue lives are about 28300, 6000 and 1800 cycles. So the 1000 cycles of fatigue tests represent about 3.5 % (ε_a = 0.3 %), 16.7 % (ε_a = 0.5 %) and 55.6 % (ε_a = 0.8 %) of their fatigue lives.

II.3. ANALYSIS AND EXPERIMENTAL RESULTS

II.3.1. ANALYSIS OF THE TESTS

for each loading time, the true strain and true stress were calculated using the equations:

$$\varepsilon_{true} = \ln(1 + \varepsilon) \tag{II-2}$$

where ε is the strain measured by the extensometer.

$$\sigma_{true} = \frac{F}{S_0}(1 + \varepsilon) \tag{II-3}$$

where F is the loading measured by the load cell and S_0 the initial section of the specimen.

II.3.2. RESULTS OF THE MONOTONIC TENSION TEST

The results obtained during the monotonic tensile test are plotted in FIG. II.5, showing the relationship between true stress and true strain. Since the extensometer used is limited to 10 %, a value much lower than the failure elongation, the monotonic tensile test was performed up to 8 % and the failure was not reached. The curve has an initial linear portion, which corresponds to the elastic part.

The Young's modulus measured during this test is 162.5 GPa. The yield strength at 0.02 % is 220.7 MPa.

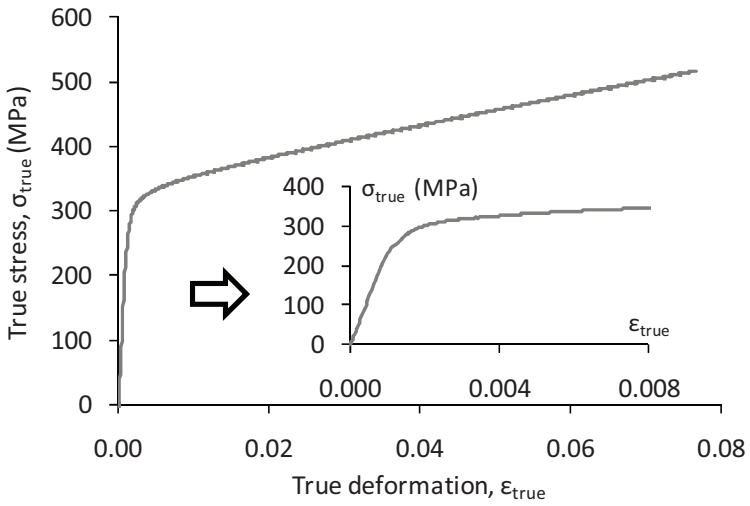

FIG. II.5 - Monotonic tension test.

II.3.3. RESULTS OF THE CYCLIC TESTS

We studied the cyclic hardening during tension-compression tests performed with total strain amplitudes of 0.3 %, 0.5 % and 0.8 %. The 3 specimens were polished before cycling in order to prevent too early fatigue crack initiation.

➢ CYCLIC HARDENING/SOFTENING

The cyclic hardening/softening curves obtained are given in FIG. II.6 and FIG. II.7 respectively. It can be seen that, for each test, a cyclic hardening occurs during the first cycles and is followed by a cyclic softening that leads to a quasi-stabilization. At ε_a = 0.3 %, the maximal stress amplitude is reached in 3 cycles. The number of cycles required to reach the maximum hardening increases with the imposed strain amplitude, and the stress amplitude increases too. At 1000 cycles, there was a clear stabilization of the stress amplitude at the imposed strain amplitude ε_a = 0.8 %, while for the two other tests, cyclic softening goes on very slowly. In steel AISI 316L at room temperature, the stabilization phase generally covers most of the lifetime [Zong 90] [Mateo 96] [Mousavi 97].

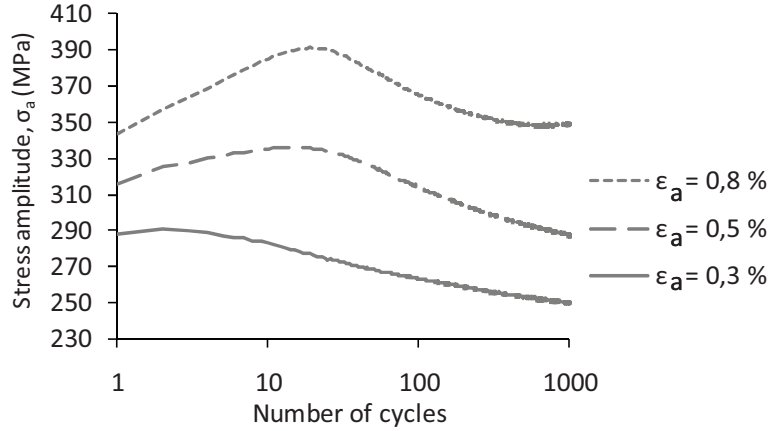

FIG. II.6 - Cyclic hardening/softening curves in semi-log diagram.

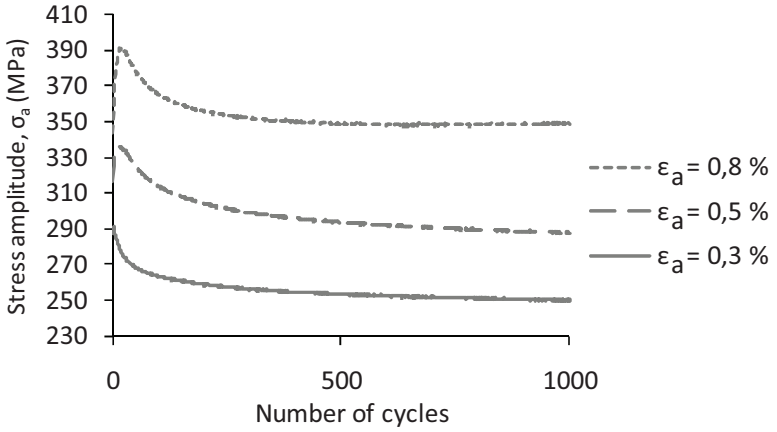

FIG. II.7 - Cyclic hardening/softening curves.

➢ HYSTERESIS LOOPS

In low-cycle fatigue, the stabilized behavior is conventionally studied at half lifetime. However, as the specimens were loaded/unloaded during only 1000 cycles and not until failure, the number of cycles to failure is not precisely known and another agreement is necessary to determine the stabilized cycle. We first checked that the variation of stress amplitude was less than 4 MPa over the last 50 cycles (950 to 1000 cycles). The difference with the first convention is only a few MPa. As fluctuations exist on the stress amplitude, it is not possible to go below this value. As the lifetime at the strain amplitudes of 0.5 % and 0.3 % are greater than 2000 cycles [Vogt 84], we chose to consider the 1000^{th} cycle as the cycle most close to the stabilized cycle. At 0.8 %, the stress amplitude varies little during cycling, so the 1000^{th} cycle was considered for simplicity.

The stress-strain hysteresis loops on the stabilized cycle are represented in FIG. II.8 for each studied amplitude. The Bauschinger effect is very important on this material, which suggests a strong kinematic hardening. This result is consistent with the literature [Choteau 99]. At the imposed total strain amplitude of 0.3 %, the loop is closer. The plastic strain amplitude is then 1.6×10^{-3}. For total strain amplitudes higher cycle opens wide. At the strain amplitudes of 0.5 % and 0.8 %, the amplitudes of plastic strain are respectively 3.2×10^{-3} and 5.9×10^{-3}.

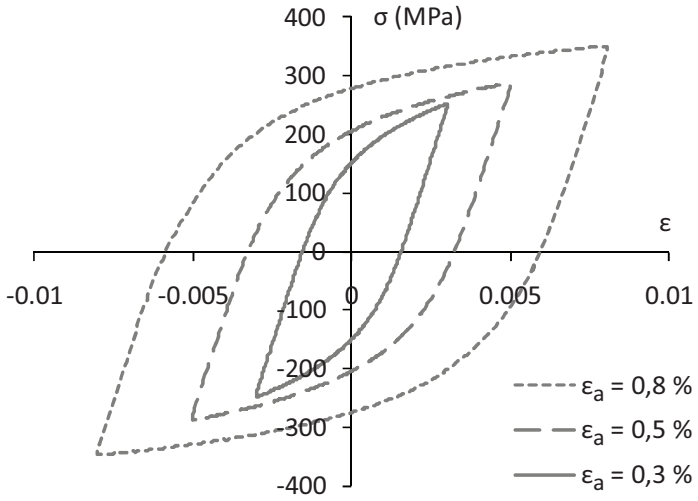

FIG. II.8 - Hysteresis loops at 1000 cycles during cyclic tension-compression tests.

➢ CYCLIC HARDENING CURVE

The stress amplitudes measured during the 1000th cycles are plotted in the tension-compression cyclic hardening curve (FIG. II.9). At the strain amplitudes of 0.3 % and 0.5 %, the stabilized stress amplitude lies slightly below the monotonic hardening curve. Cycling induces a slight softening compared to the monotonic tension. At 0.8 %, the stabilized stress amplitude is above the monotonic hardening curve. Cycling induces then a slight hardening.

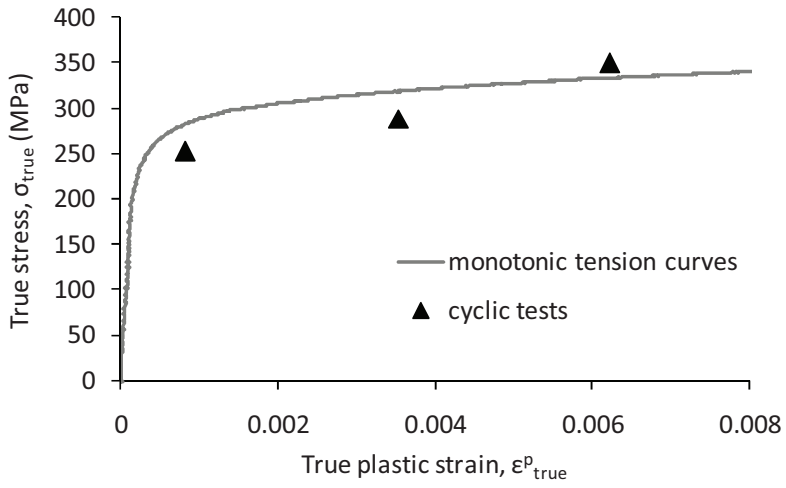

FIG. II.9 - Tension-compression cyclic hardening curve, compared to the monotonic tension curve.

➢ EVOLUTION OF THE YOUNG'S MODULUS

In order to characterize the behavior of the material and then to simulate it, it is necessary to measure the Young's modulus from the experimental elastic parts [Aubin 01]. It has been measured two times per cycle, each time the loading crosses the elastic domain, as shown in FIG. II.10a. The two Young's moduli measured in a given cycle have been called up and down. For a given measurement, only points recorded in the range $R_\varepsilon < \varepsilon < D_\varepsilon + R_\varepsilon$ are used to calculate the slope of the elastic straight line (FIG. II.10b). The first points of a loading (for which $\varepsilon < R_\varepsilon$) are scattered, so they are preferably not included. The parameter D_ε is chosen to ensure that the calculation of the Young's modulus occurs in the elastic domain and also that there are enough points for the calculation [Wu 91]. In this study, the Young's modulus is calculated using a post-treatment program developed in our laboratory [Aubin 01]. This program allows to obtain the Young's modulus with the maximal correlation coefficient.

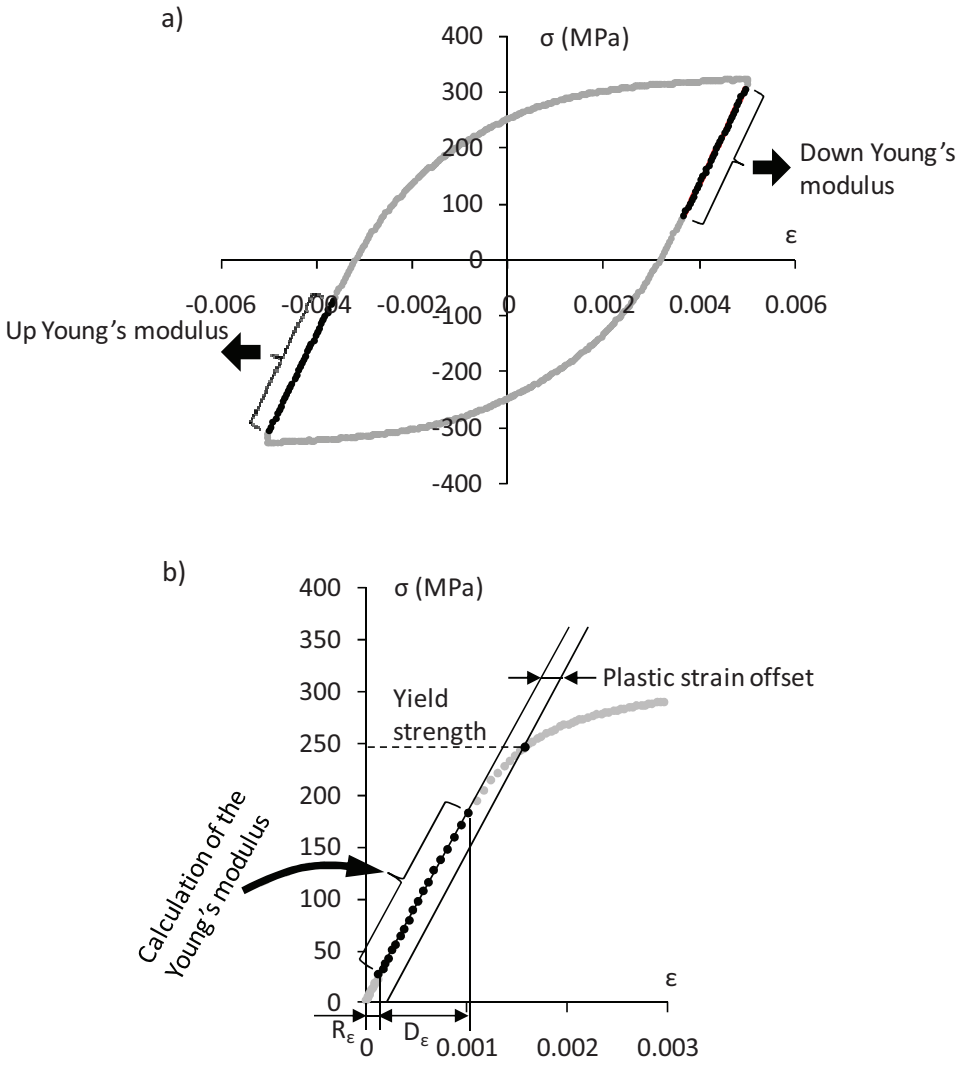

FIG. II.10 - Measurement of up and down Young's moduli a); Measurement of a Young's modulus b).

FIG. II.11 shows the evolution of the Young's modulus during the three fatigue tests. It is found that except for ε_a = 0.5 %, for which the up and down curves overlap, the up Young's modulus is always below that the down one. The difference is about 8 GPa for the test at 0.3 % and 10 to 15 GPa for the test at 0.8 %. The values obtained for the up and down Young's modulus vary between 165 and 185 GPa. For the tests at 0.3 % and 0.5 %, the modulus decreases slightly during the first cycles and then stabilizes, it then is almost constant. However, large scattering can be seen from one cycle to another for the test at 0.8 %.

For all these tests, as the Young's modulus remains constant in average during the major part of the test, it can be considered that there is no macroscopic damage during the first 1000 cycles.

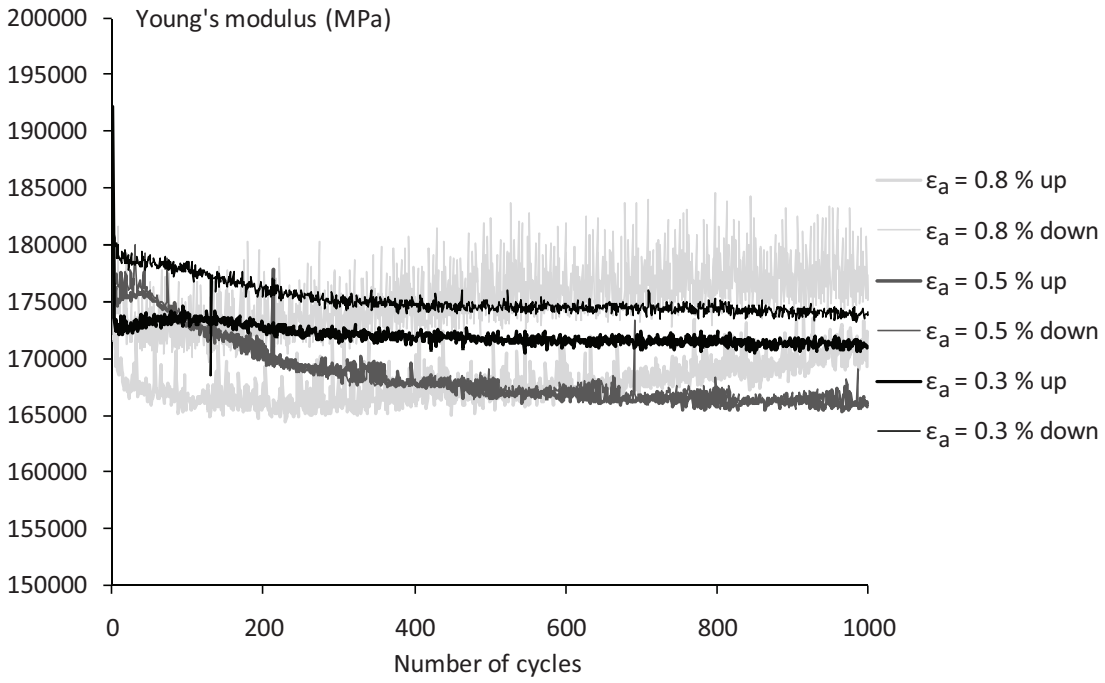

FIG. II.11 - Evolution of the Young's modulus during the three cyclic tests.

II.4. CONCLUSION

In this chapter, the fatigue behavior of an austenitic stainless steel was experimentally studied.

The chemical composition of the studied material was measured. The material has an average grain size of 50 µm and a globally isotropic microstructure. A monotonic tension test and three cyclic tension-compression tests at various total strain amplitudes were performed to characterize the mechanical behavior of this material. All tests were performed with a constant strain rate and at room temperature. After presenting the analysis method, the experimental results have been shown. A cyclic hardening/softening leading to a quasi-stabilization was observed during the cyclic tests. The hysteresis loops of the stabilized stress-strain cycle showed a strong Bauschinger effect, which is in agreement with the literature and suggests a strong kinematic hardening. The material exhibits a cyclic softening at the lowest strain amplitudes tested. The Young's modulus was also calculated two times per cycle during the cyclic test. The method for calculating the Young's modulus has been described. The Young's modulus is almost constant during cycling, indicating the absence of macroscopic damage.

III. MODEL INTRODUCED

III.1. INTRODUCTION

In the previous chapter, we saw several experimental results concerning the macroscopic mechanical behavior of the austenitic stainless steel tested. In the present chapter, the modeling of the behavior observed experimentally will be discussed. Three approaches are possible to simulate the mechanical behavior of a metal alloy:

- The macroscopic approach is based on the use of macroscopic internal variables chosen to account for the observed macroscopic phenomena [Armstrong 66] [Mroz 67] [Chaboche 83] [Chaboche 91] [Benallal 87] [Tanaka 94] [Calloch 97]. The validity of these models is often restricted to the experimental base which was used to their identification.

- The multi-scale approach, is more "physical" in the sense that internal variables are linked to physical mechanisms at the microscopic scale (here the grain scale) [Pilvin 90] [Cailletaud 92] [Gaudin 02] [Abdul-Latif 04]. This approach aims at accounting for macroscopic and microscopic phenomena.

- The Finite Element approach simulates the behavior of polycrystalline aggregates, large enough to be a representative elementary volume of the material [Barbe 01a, b] [Erieau 04].

In conclusion, links with the actual mechanisms of deformation are lacking in the macroscopic approach. The finite element approach has the major drawback of taking long computation times, incompatible with the simulation of fatigue tests. Only a few dozens of cycles can be simulated, which prevent to predict the behavior under variable amplitude conditions. In order to take the physical mechanisms into account and to limit the computation time, the multi-scale approach was then chosen in this study.

In the next sections, the principles and formulations of the multi-scale modeling of the mechanical behavior in fatigue, and the identification of the parameters used in the model will be presented.

III.2. MULTI-SCALE MODELING OF THE MECHANICAL BEHAVIOR

The multi-scale modeling method, also called homogenization method, consists in the determination of the macroscopic behavior of an equivalent homogeneous medium (EHM), which is assumed to

have the same behavior as the real heterogeneous material. The multi-scale modeling requires 4 steps (see FIG. III.1):

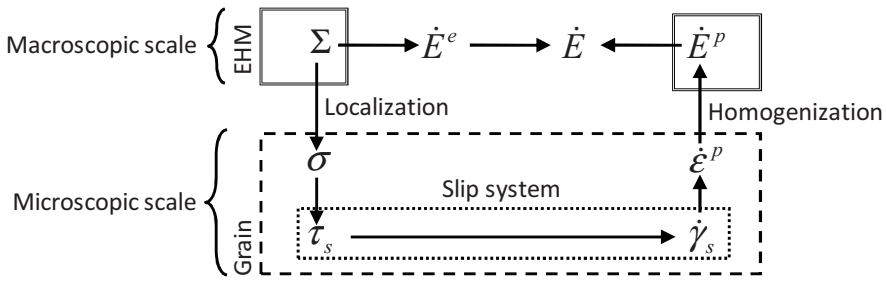

FIG. III.1 - Homogenization principle.

1. The representation is based on the description of the microstructure of the material, and describes in particular the "phases", both geometrically and mechanically. A "phase" here is an entity whose properties may be considered homogeneous. A representative volume element (RVE) of the studied material is defined in this way. The quality of modeling is based primarily on this first step. The defined RVE must satisfy the scales separation condition (homogeneous macroscopic scale and heterogeneous microscopic scale) and underline the characteristics of the microstructure and physical mechanisms of deformation.

2. The localization links stress or strain fields in each "phase" to the macroscopic stress or deformation fields.

3. The local behavior law is based, at least partly, on physical mechanisms that cause the studied behavior. A good knowledge of the physical mechanisms is then required.

4. The homogenization connects the average volume of local fields to the macroscopic fields.

The multi-scale modeling has then been applied to austenitic stainless steel AISI 316L, aiming at simulating the fatigue behavior of this material experimentally observed.

In the following, the four steps of the multi-scale modeling and the identification of parameters will be presented.

III.2.1. Analysis of steel AISI 316L

The studied stainless steel is composed of only one polycrystalline phase: austenitic phrase, with a grain size of about 50 μm. So the modeling requires two scales. One macroscopic homogeneous scale including several grains represents the macroscopic mechanical behaviors of the material. And one heterogeneous granular scale considers the micromechanical behavior. The grains in this study can be considered equiaxial. In polycrystals such as the studied steel, no grain plays a particular role compared with other grains. The best way to take into account the interactions between a grain and its neighbors is then to use a self-consistent model. In this model, each grain is surrounded by a matrix corresponding to the equivalent homogeneous medium (EHM) which is looked for (FIG. III.2). The word grain will be used here instead of phase to avoid misunderstanding with metallurgical phases. In the model, a grain does not refer to an individual physical grain but to all the physical grains having the same crystallographic orientation.

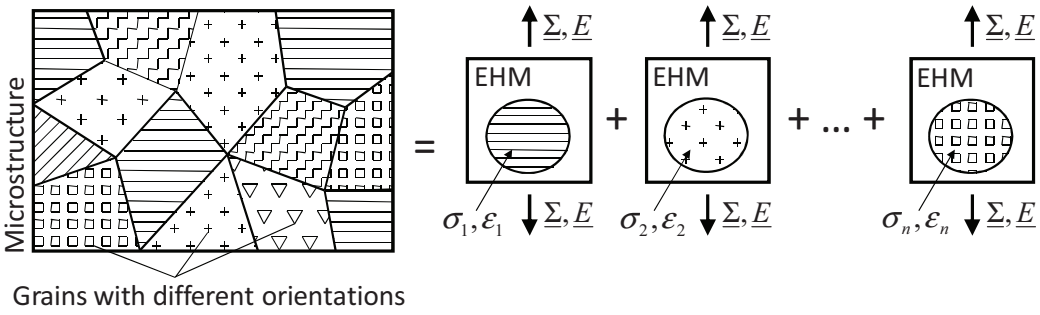

FIG. III.2 - Principle of self-consistent modeling.

The consistency conditions (global compatibility and equilibrium) require that the average of the local fields over the volume of the aggregate should equal the macroscopically imposed ones:

$$\underline{E} = \langle \underline{\varepsilon}_g \rangle = \sum_g f_g \, \underline{\varepsilon}_g \tag{III-1}$$

$$\underline{\Sigma} = \langle \underline{\sigma}_g \rangle = \sum_g f_g \, \underline{\sigma}_g \tag{III-2}$$

where $\underline{E}$ and $\underline{\Sigma}$ are the macroscopic strain and stress, respectively, f_g is the inclusion volume fraction, and ε_g and σ_g are the granular strain and stress, respectively.

Besides, a texture measurement of the studied material has been done and shows that the material studied is slightly textured. FIG. III.3 presents the pole figures in the longitudinal direction for an observation zone of the dimensions of 2.1 × 2.0 mm^2.

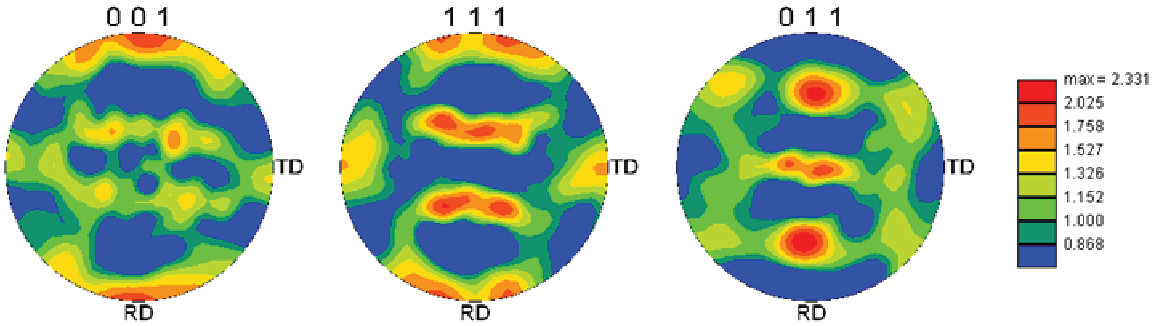

FIG. III.3 -Pole figures in the longitunal direction obtained in a zone of 2.1 × 2.0 mm^2.

An isotropic distribution of grain orientations is then needed to simulate the mechanical behavior of the materials. Two strategies exist. It is first possible to define a random distribution of grain orientations. If the number of grains is sufficient (higher than 500 for FCC materials [Lebensohn 04]), the mechanical behavior will be isotropic. The second solution is to define a distribution composed of a limited number of grains carefully chosen. Several authors have shown that isotropic distributions of orientations limited to 48 or 40 grains are capable of describing the macroscopic behavior of polycrystalline isotropic materials satisfactorily [Cailletaud 92] [Pilvin 90] [Abdul-Latif 04]. The computation time is reasonable, which is particularly interesting in the case of simulation of cyclic tests. In this study, 500 random grain orientations without texture were used to model the mechanical behavior. However, during the identification of parameters, the set of 40 grain orientations proposed by Pilvin [Pilvin 90] was used. Their distribution is shown in FIG. III.4.

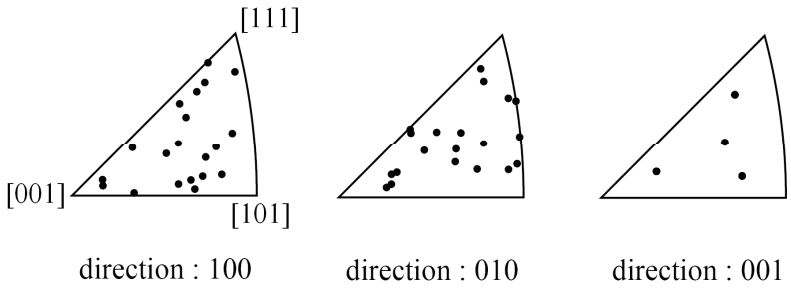

FIG. III.4 - Inverse pole figure of 40 chosen grain orientations used for the identification.

(Loading direction: 100.)

III.2.2. LOCALIZATION LAW

The physically-based modeling of plasticity in polycrystals was first carried out by Sachs [Sachs 28] and Taylor [Taylor 38]. The models of Sachs and Taylor assume respectively an uniform aggregate stress or strain equal to the macroscopic one and are known as the lower or upper bound models. Although various extensions exist for the models of Sachs and Taylor (e.g. [Lin 57] [Hutchinson 76] [Asaro 85]) in order to consider viscoplastic, elastic-viscoplastic or elastic-plastic deformations, neither of these two families of models can consider both the stress and deformation heterogeneities.

In order to consider the intergranular heterogeneities of polycrystals, self-consistent approaches were used. The principles of self-consistent modeling have been introduced in section III.2.1. Eshelby [Eshelby 57] first considered an ellipsoidal inclusion in a linear elastic matrix. Then Kröner [Kröner 61], Budianski and Wu [Budianski 62] extended Eshelby's model and proposed an elastic-plastic self-consistent model for small deformations of polycrystals. However, the models above neglect plastic interactions between the inclusion and the surrounding matrix. To account for these interactions, a generalized incremental self-consistent formulation for small elastic-plastic deformations was proposed by Hill [Hill 65]. Hill's model accounts for full anisotropy of the elastic-plastic interactions. But this model executes many explicit calculations at each time step which requires much time. For this, Berveiller and Zaoui [Berveiller 79] proposed to simplify the interaction law and account for these interactions in an isotropic way.

Besides the self-consistent models considering time-independent plasticity mentioned above, the crystal plasticity theory was also extended for time dependent plasticity, namely viscoplasticity (e.g. [Rice 71] [Brown 70] [Hutchinson 76] [Molinari 87]). In these models, both incremental and non-incremental formulations can be found. Then, several rate-dependent self-consistent models have been proposed to include elasticity in the formulation (e.g. [Weng 82] [Nemat-Nasser 86] [Kouddane 94] [Dingli 00] among many others).

In order to simulate the fatigue behavior of the material, it is necessary to choose a localization law that can be used under cyclic loadings, which is not generally the case. Evrard [Evrard 08] compared two localization laws to simulate the mechanical behavior of a duplex stainless steel under complex cyclic loadings, the first one was proposed by Abdul-Latif *et al*. [Abdul-Latif 02] and the second one by Cailletaud [Cailletaud 92] and Pilvin [Pilvin 90]. Both laws showed good capacity in predicting the mechanical behaviors under complex cyclic loadings. However, the latter was found to be able to

better simulate Bauschinger effect and to have a less simulation cost, with a same crystalline constitutive law. The localization law of Cailletaud-Pilvin has thus been adopted in this study.

In the localization law of Cailletaud-Pilvin, the following hypotheses are considered:

- grains are spherical,
- the behavior of the Equivalent Homogeneous Medium (EHM) is elastoplastic and isotropic,

In order to simulate cyclic or non-radial tests, viz. non-proportional tests, Cailletaud and Pilvin introduced phenomenological intergranular accommodation variables $\underline{\beta}^g$ in the expression proposed by Kröner. The localization law is then written as:

$$\underline{\sigma}^g = \underline{\Sigma} + \mu\left(\underline{B} - \underline{\beta}^g\right) \tag{III-3}$$

where $\underline{B}$ is the average of intergranular accommodation variables $\underline{\beta}^g$ in all the grains:

$$\underline{B} = \sum_g^{N_g} f^g \underline{\beta}^g \tag{III-4}$$

Here f^g is the volume fraction of each grain (1/40 or 1/500). The variable $\underline{\beta}^g$ plays the role of a kinematic hardening. In order to consider correctly the response under cyclic loadings, Cailletaud and Pilvin proposed to give to $\underline{\beta}^g$ an evolution similar to the Armstrong-Frederick kinematic hardening law [Armstrong 66] [Lemaitre 88]:

$$\dot{\underline{\beta}}^g = \dot{\underline{\varepsilon}}^{pg} - D\left(\underline{\beta}^g - \delta\underline{\varepsilon}^{pg}\right)\left\|\dot{\underline{\varepsilon}}^{pg}\right\| \tag{III-5}$$

where D and δ are two parameters to be identified.

It should be mentioned that the consistency condition in stress, EQ. III-2, is not automatically validated for the localization law of Cailletaud-Pilvin. Attemps are made to satisfy the consistency condition by two methods. One method consists in identifying the parameters in two steps using the localization law of Berveiller-Zaoui [Berveiller 79] [Evrard 08]. Another way is to verify the self-consistency condition after the numerical simulation. This second way was chosen here and will be explained in the discussion part of this chapter.

III.2.3. LOCAL BEHAVIOR LAW

The purpose of this work is the modeling of the plastic deformation of a metal alloy. The main mechanism of plastic deformation is the dislocation slip on crystal planes in grains of the polycrystal. It is thus necessary to know the crystal lattice of the material and the nature of the associated slip systems, and then to write a constitutive behavior law physically based at the scale of slip systems.

- CRYSTAL STRUCTURE

Face-centered cubic crystals (FCC) as austenite have four {111} slip planes with three <110> slip directions in each, and therefore have twelve {111}<110> slip systems, as seen in FIG. III.5 and TAB. III.1.

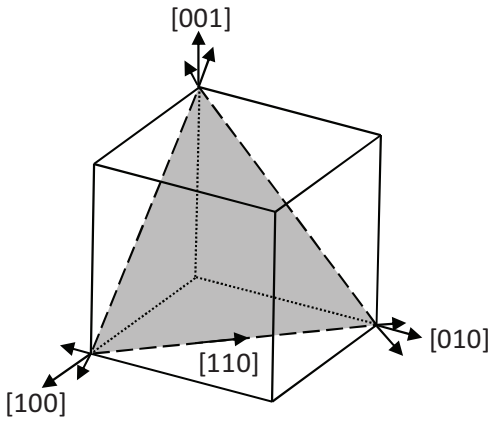

FIG. III.5 - Slip systems in a FCC structure.

Slip plane	Slip directions						Possible slip systems		
A:(-111)							A2	A3	A6
B:(111)	1	2	3	4	5	6	B2	B4	B5
C:(-1-11)	[011]	[0-11]	[101]	[-101]	[-110]	[110]	C1	C3	C5
D:(1-11)							D1	D4	D6

TAB. III.1 - Notations of Schmid and Boas of slip systems {111}<110> .

➢ CRYSTAL ELASTICITY

In section I.4.2, elastic anisotropy of crystals has been presented. The elastic anisotropy of austenite is very high, as the ratio of extremum elastic moduli is about 3. It may be possible to take this elastic anisotropy into account, for example, in modifying the isotropic localization law of Abdul-Latif *et al.* [Dingli 00] who simplified that of Molinari *et al.* [Molinari 97]. However it has been shown that, for austenitic stainless steel, the elastic anisotropy plays an important role at low plastic strain, but at a strain larger than 0.2 %, this influence becomes negligible [Osterstock 08]. Taking into account the elastic anisotropy would thus not significantly improve the results in the range of plastic strains studied [0.15 % - 0.60 %]. The elasticity has thus be considered as isotropic.

➢ CRYSTAL LAW BASED ON DISLOCATION DENSITIES

In FCC crystals, the slip planes have a normal of type {111} (dense planes), and slip directions are defined by the Burgers vectors of type <110> (FIG. 1.12). Each slip direction belongs to two slip planes. There are 12 slip systems in total. The shear stress τ^s on slip system s is obtained by projecting geometrically the granular stress σ^g on the slip system considered:

$$\tau^s = \sigma^g : m_g^s = \sigma^g : \frac{1}{2}\left(\overrightarrow{n^s} \otimes \overrightarrow{b^s} + \overrightarrow{b^s} \otimes \overrightarrow{n^s}\right) \quad \text{(III-6)}$$

where $\overrightarrow{b^s}$ and $\overrightarrow{n^s}$ are respectively the Burgers vector and the unit vector normal to the slip plan.

Various models can be used to describe the plasticity in a slip system. One of them is a thermodynamical model [Cailletaud 92]. This model contains an isotropic hardening variable and a kinematic hardening variable, and introduces a free energy, a dissipation potential, and a viscous potential in order to define a phenomenological viscoplastic constitutive law. However, this thermodynamical model introduces parameters without any physical meaning. In this study, a physical model based on internal variables (the density of dislocations on each slip plane), which has evidently physical meaning, will be used and presented below.

In a given state, a high number of dislocations are present in the crystal. These dislocations belong to different slip systems and entangle with each other.

In order to take into account the interactions of a given dislocation with the dislocations of the "forest", the critical shear stress on a given slip system s, τ_c^s, can be related to the density of dislocations stored on other slip systems:

$$\tau_c^s = \tau^0 + \mu b \sqrt{\sum_t h^{ts} \rho^t} \quad \text{(III-7)}$$

with τ^0 the initial shear stress on the slip system, b the norm of the Burgers vector, μ the shear modulus and ρ^t the density of dislocations stored on the slip system t. The matrix h^{ts} permits to distinguish the interactions of the different slip systems between them [Franciosi 84]. The form of this matrix depends on the crystallographic structure of the material [Franciosi 85]. For FCC crystals, it is a 12 × 12 matrix. A simple form of this matrix is chosen, which introduces only one parameter for the non-diagonal terms (characterizing the latent hardening), h, whereas the diagonal terms (corresponding to the self-hardening) are equal to 1 [Tabourot 01] [Evrard 08].

The slip occurs when the shear stress on one or several slip systems reaches the critical shear stress. The rule is simple to state but requires sophisticated criteria to select the active slip systems, the multiple slip can lead to numerical indeterminacies. A numerically simpler solution consists in writing a viscoplastic-type power law as:

$$\dot{\gamma}^s = \langle \frac{|\tau^s| - \tau_c^s}{K} \rangle^n \operatorname{sign}(\tau^s) \text{ if } |\tau^s| \geq \tau_c^s \text{ if not } \dot{\gamma}^s = 0 \qquad \text{(III-8)}$$

where τ_c^s is the critical shear stress on slip system s, K and n are material viscosity parameters. The power laws were originally developed for the polycrystals of a FCC structure [Asaro 85] [Tabourot 97] [Kalidindi 01]. They were subsequently used in polycrystals of BCC structure [Paquin 01] [Hoc 01]. The primary interest of this type of law is its simplicity, because it requires only 3 parameters and allows to remove the numerical indeterminacies on active systems induced by the plasticity which is independent of time. It should be noted that when $n \to \infty$, the behavior tends to plasticity independent of time, with τ_c^s as threshold shear stress.

At last, the granular plastic strain rate is calculated as:

$$\dot{\varepsilon}^{pg} = \sum_s m_g^s \dot{\gamma}^s \qquad \text{(III-9)}$$

Let us now make the density of dislocations to evolve as a function of the deformations stored in a grain. For this purpose, the total dislocations density on slip system s, ρ^s, is considered. Some of these dislocations are mobile while others are immobile, or stored.

$$\rho^s = \rho_{imm}^s + \rho_{mob}^s \qquad \text{(III-10)}$$

Mobile dislocations can accommodate plastic deformation. Experimentally, it was shown that the density of mobile dislocations is much lower than the density of immobile dislocations [Tabourot 01]. We therefore consider that:

$$\rho^s = \rho_{imm}^s \qquad \text{(III-11)}$$

The evolution of dislocation densities is related to three mechanisms. Dislocations are produced by Franck-Read mechanism from dislocation segments anchored at their ends, they interact with dislocations of other systems and are therefore likely to be immobilized [Franciosi 82]. Dislocations of the same system but of opposite directions annihilate when they intersect with each other at a distance less than the capture radius [Fridel 64]. Moreover, experimental observations have shown that for quasi-static tests in which the temperature varies slowly, the mobile dislocation density is constant [Mecking 70]. We have then:

$$\dot{\rho}^s = \dot{\rho}^s_{imm} = \dot{r}^s_{imm\,p} - \dot{r}^s_{imm\,a} \tag{III-12}$$

where $\dot{r}^s_{imm\,p}$ and $\dot{r}^s_{imm\,a}$ are respectively the production rate of immobile dislocations (that is to say, the immobilization rate of mobile dislocations) and the annihilation rate of immobile dislocations.

The immobilization rate of mobile dislocations is calculated from the mean free path of a dislocation:

$$\dot{r}^s_{imm\,p} = \frac{1}{b}\left(\frac{\sqrt{\sum_{t\neq s}\rho^t}}{L}\right)|\dot{\gamma}^s| \tag{III-13}$$

where L is a parameter characterizing the dislocation production.

The annihilation rate of dislocations $\dot{r}^s_{imm\,a}$ is obtained by evaluating the number of dislocations that may cross the annihilation volume around a given dislocation.

$$\dot{r}^s_{imm\,p} = \frac{2y_c\rho^s}{b}|\dot{\gamma}^s| \tag{III-14}$$

with y_c a parameter controlling the annihilation of stored dislocations.

The evolution of dislocation density is thus expressed as [Essmann 79]:

$$\dot{\rho}^s = \frac{1}{b}\left(\frac{\sqrt{\sum_{t\neq s}\rho^t}}{L} - 2y_c\rho^s\right)\dot{\gamma}^s \text{ with } \rho^s(\gamma^s = 0) = \rho^0 \tag{III-15}$$

The crystal law based on dislocation densities introduces only one internal variable (the density of dislocations) per slip system. It should be noted that no kinematic hardening variable is introduced in slip systems. The kinematic hardening is thus only considered through the localization law. It has been shown by [Pilvin 90] and [Evrard 08] that may be sufficient to describe the macroscopic mechanical behavior, although only the intergranular kinematic hardening is taken into account and not the intragranular kinematic hardening. In order to take this intragranular kinematic hardening, specific laws have to be developed at the grain size, using the last developments of dislocation dynamics simulations [Manole 10].

III.2.4. HOMOGENIZATION LAW

The homogenization law defines the macroscopic strain rate as a function of the microscopic strain rates. The macroscopic plastic strain rate is obtained as the average of the microscopic strains:

$$\underline{\dot{E}}^{p} = \sum_{g} f^{g} \underline{\dot{\varepsilon}}^{pg} \tag{III-16}$$

The total strain rate is thus defined as:

$$\underline{\dot{E}} = \underline{\dot{E}}^{e} + \underline{\dot{E}}^{p} \tag{III-17}$$

where the elastic strain rate is written as:

$$\underline{\dot{E}}^{e} = \frac{1}{2\mu}\left(\tilde{I} - \frac{\nu}{1+\nu}\underline{1}\otimes\underline{1}\right)\underline{E} \tag{III-18}$$

III.3. IDENTIFICATION OF PARAMETERS

III.3.1. INTRODUCTION

The number of parameters to be identified is shown in TAB. III.2. The identification of the parameters is carried out in two steps. First, the elasticity parameters are measured based on the experimental results and most of the parameters of crystal plasticity are obtained from the literature. Then, the remaining crystal plasticity parameters and the parameters of the localization law are obtained by inverse method. In the next paragraphs, the identification process of these parameters will be given.

Parameter type	Number of parameters	Name
Elasticity	2	λ, μ
Crystal plasticity	8	$b, \rho, K, n, L, \tau^0, h, y_c$
Localization	2	D, δ

TAB. III.2 - Parameters to be identified.

III.3.2. IDENTIFICATION OF PARAMETERS

- PARAMETERS OF ELASTICITY

The modulus of elasticity E is measured on the first ¼ cycle of the tension-compression fatigue test with a strain amplitude of 0.5 %, see chapter II. The slop of the least square trendline corresponding

to the linear part was calculated. The correlation coefficient was also calculated in order to verify if the points chosen are all in the linear part. The measured elastic modulus is then 184 401 MPa.

The standard value of Poisson's ratio for steels is 0.3. The Lamé's elasticity coefficients are then calculated:

$$\lambda = \frac{E\upsilon}{(1+\upsilon)(1-2\upsilon)} = 106385 \text{ MPa} \quad \text{(III-19)}$$

$$\mu = \frac{E}{2(1+\upsilon)} = 70923 \text{ MPa} \quad \text{(III-20)}$$

➢ PARAMETERS OF CRYSTAL LAW AND LOCALIZATION LAW

The values of some crystalline parameters can be found in the literature. The Burgers vector for an austenitic crystal is: $b = 2.58 \times 10^{-10}$ m [Frost 82]. As the material is laminated, the initial dislocation density is taken as: $\rho^0 = 10^{-12}$ m^2 [François 91]. The values of the viscosity parameters are those proposed by [Cailletaud 91] for an austenitic stainless steel: $K = 20$ MPa.s^{-1} and $n = 10$. The parameter controlling the production of dislocations, L, is calculated with the formula proposed by Rauch and Thuillier [Rauch 93]:

$$d = \frac{L}{\sqrt{11\rho^0}} \quad \text{(III-21)}$$

where the grain size for this austenitic steel, $\bar{d}$, equals to 50 µm. The EBSD measurement permits to obtain the distribution of the grain size in an observation zone of dimensions 2.1 × 2.0 mm^2, as seen in FIG. III.6. The crystal twins were considered as entire grains. Most grains have a grain size between 10 and 135 µm, and they have a normal distribution.

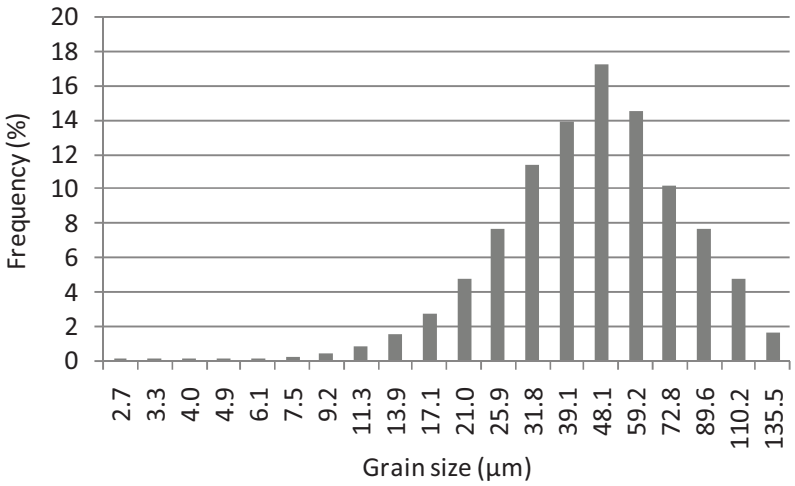

FIG. III.6 - Distribution of grain size in an observation zone of dimensions 2.1 × 2.0 mm^2.

➢ IDENTIFICATION BY INVERSE METHOD

The rest of parameters cannot be measured, so an inverse method was adopted to identify them. It was decided to use a genetic algorithm to find the best parameter set. Genetic algorithms are a particular class of evolutionary algorithms (EA) that use techniques inspired by the process of evolution through natural selection suggested by Darwin. They are powerful search techniques used in computing to find exact or approximate solutions to optimization and search problems (see e.g. [Furukawa 02] [Qu 05] among many others). GAs are based on the collective learning process within a population of individuals, each of which represents a search point in the space of potential solutions to a given problem [Furukawa 97]. Nowadays, these algorithms are often used, leading to good results and performance, in the solution of structural problems or the characterization of constitutive models [Lagaros 05] [Jiménez 06] [Andrade-Campos 07] [Pyrz 07].

The principle of the parameter identification is shown in FIG. III.7. First, an initial population is generated. Each member of this population corresponds to a parameter set (the genes). These parameter sets are obtained at random inside the ranges defined by the upper and lower limits of each parameter. Then the mechanical model is used for the calculation. It should be noted that a Rungekutta method of second order is used during the integration. The macroscopic stress at each time point is calculated from the input data of macroscopic strain. A cost function F is then defined for each parameter set A by comparing the simulated results with the experimental ones

$$\mathrm{F}(\mathrm{A}) = \sum_{\mathrm{t}} (\mathrm{Z}^{\mathrm{exp}}(\mathrm{t}) - \mathrm{Z}^{\mathrm{sim}}(\mathrm{A}, \mathrm{t})) \qquad \text{(III-22)}$$

where $\mathrm{Z}^{\mathrm{exp}}$ and $\mathrm{Z}^{\mathrm{sim}}$ are respectively the experimental and simulated results. The aim is then to find the parameter set A minimizing this function. The population will evolve at each generation in order to let appear better parameter sets in the sense of the function F. There are 3 possibilities to let the population evolve (FIG. III.7):

- A given proportion of the initial population is kept. Set of parameters having a lower cost function have a higher probability to be selected. This is called succession.
- Two individuals can exchange some of their genes. This is called cross-over.
- A gene of a given individual changes randomly. This is called mutation

Cross-over and mutation allow to explore new sets of parameters which did not exist in the initial population. Several generations are produced in that way. The process terminates after a given number of generations, or if a given value of the cost function is reached.

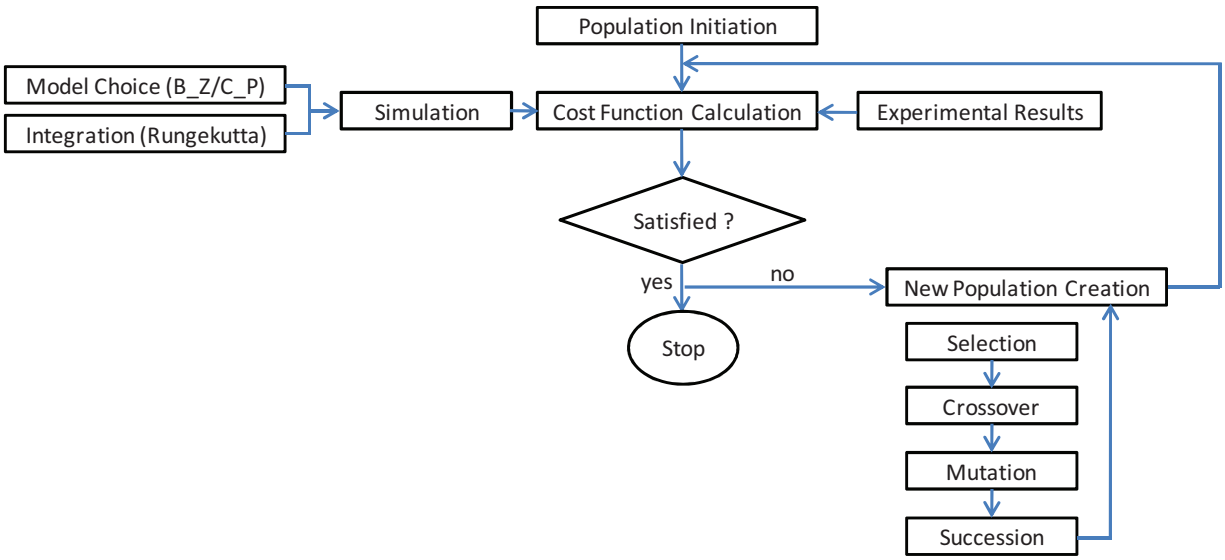

FIG. III.7 - Flow chart of parameter identification with a genetic algorithm.

In this study, the identification with genetic algorithm was carried out with an initial population of 200 parameter sets and 100 generations. Crossover, mutation and succession probabilities were 0.8, 0.25 and 0.8 respectively.

Before optimization, upper and lower limits of the parameters have to be firstly fixed in order to obtain values with physical meaning. These limits are given in TAB. III.3 with the references used.

Parameters	Limits	References
τ^0	70 MPa < τ^0 < 120 MPa	[Baczmański 04]
h	$h < 1$	[Madec 01]
y_c	y_c < 20 nm	[Hoc 01]

TAB. III.3 - Limits of the parameters used for identification.

The identification of the 5 parameters of the crystalline behavior law, τ^0, h, y_c, D and δ, is carried out using the localization law of Cailletaud-Pilvin. The self-consistency condition (EQ. III-1, III-2) is supposed to be respected [Cailletaud 92]. The first 5 cycles of the hysteresis loops of the fatigue test at the strain amplitude of 0.5 % are used in the identification. The values of the identified parameters are shown in TAB. III.4. The simulated first 5 cycles of the hysteresis loops are shown together with the experimental ones (FIG. III.8). The experimental and simulated results are globally in good agreement, except near yield stresses where the curvature of the simulated curve is too sharp.

Parameter	Note	Value	Reference
λ	parameters of elasticity	106 385 MPa	Measured
μ		70 923 MPa	
b	Burgers vector	2.58×10^{-10} m	[Frost 82]
ρ^0	initial dislocation density	10^{12} m^{-2}	[François 91]
K	viscosity parameters	20 MPa.$s^{1/n}$	[Cailletaud 91]
n		10	
L	parameter controlling the production of dislocations	165	[Rauch 93] + identification
τ^0	initial shear stress	73.0 MPa	Identification
h	component of the interaction matrix	0.12	
y_c	parameter homogeneous to the distance of annihilation of dislocation dipoles	8.0×10^{-9} m	
D	parameters of the localization law of Cailletaud Pilvin	171 MPa	
δ		2.50	

TAB. III.4 - Values of the parameters.

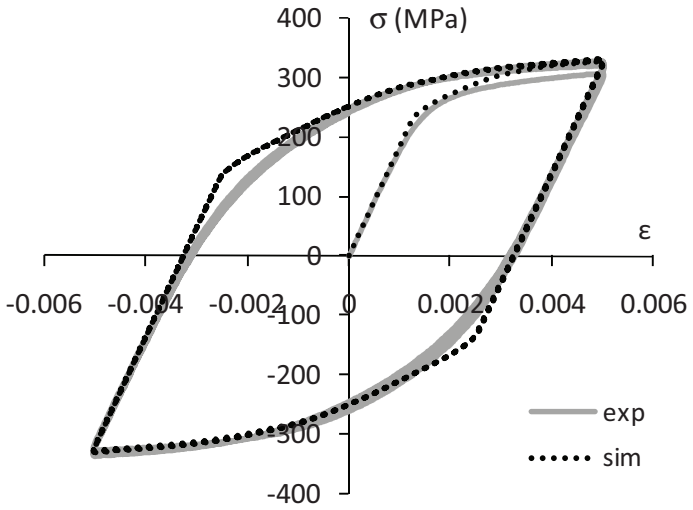

FIG. III.8 - Comparison of experiments and simulated results during the first 5 cycles of a cyclic test with a strain amplitude of 0.5 %.

III.3.3. Discussion and conclusion

➢ Analysis of the self-consistency condition

The localization law of Cailletaud-Pilvin (called CP localization law) does not satisfy automatically the self-consistency condition [Cailletaud 92] [Evrard 08]. On the contrary, this condition is verified by the localization law of Berveiller-Zaoui (referred as BZ law below) [Berveiller 79] [Besson 01]. This is

the reason why some authors recommend to identify first the parameters of the crystalline behavior law with the BZ localization law, as this law does not introduce any parameter to identify and then identify the two parameters of the CP localization law on a radial loading[1] simulated with the BZ localization law [Evrard 08] so that the self-consistency condition is verified at least in these conditions.

The Berveiller-Zaoui localization law is based on the model of Kröner, so grains are considered as spherical. EHM is assumed isotropic and elastoplastic. The BZ law can then be written:

$$\underline{\sigma}^{g} = \underline{\Sigma} + \mu\xi\left(\underline{E}^{p} - \underline{\varepsilon}^{pg}\right) \tag{III-23}$$

where ξ is a scalar function of isotropic plastic accommodation:

$$\frac{1}{\xi} = 1 + \frac{3}{2}\mu\frac{\|\underline{E}^{p}\|}{J_2(\Sigma)} \tag{III-24}$$

It should be noted that the BZ law is valid only for a radial and monotonous loading.

This strategy was tried on the material studied. In a first step, the four parameters needed in the crystal laws, τ^0, h, y_c were first identified using BZ law and the experimental results of the first ¼ cycle. As shown in FIG. III.9, a good agreement can be seen. In a second step, the two parameters of the CP law, D and δ, were identified using both the simulated curve of the first ¼ cycle using BZ law and the experimental results of the first cycle. As the localization law plays also the role of a kinematic hardening, it is necessary to use a cyclic test to identify its parameters and properly describe the Bauschinger effect. Simulated results of the first cycle are compared to the experimental ones in FIG. III.10. As shown in this figure, the slope of the plastic parts is overestimated by the simulation, but it was not possible to obtain a better set of parameters D and δ. FIG. III.11 shows the first 20 cycles of this cyclic test continuing. As the cycling continues, the hardening grows cyclically without saturation. This is the reason why we chose to identify all the parameters (crystalline +CP localization law) in one step on several cycles, as presented above. However, the condition of self-consistency still remains to be verified.

[1] The radial loading is the only loading path that can be simulated with the BZ localization law.

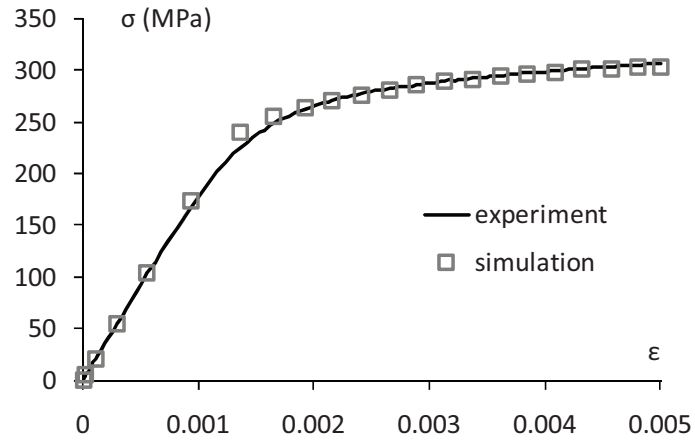

FIG. III.9 -Comparison of an experimental monotonic tension test and its simulation with the BZ localization law.

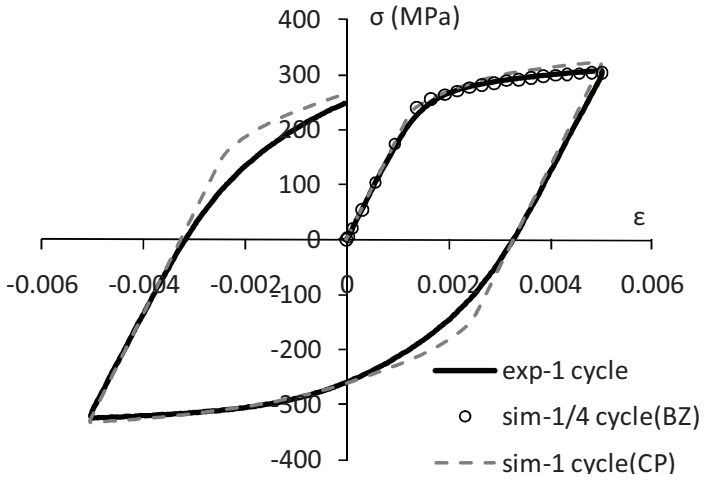

FIG. III.10 - Comparison of the experimental results obtained during the 1st cycle with ε = 0.5 % and the simulated ones using BZ and CP localization laws.

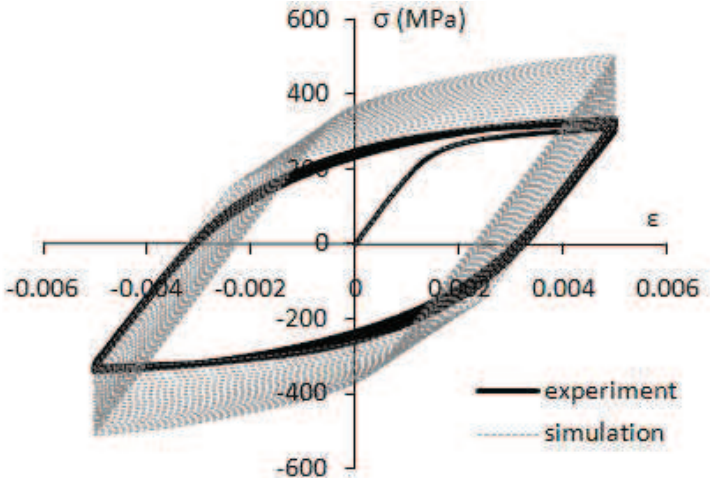

FIG. III.11 - Simulation of the first 20 cycles of a tension-compression test with ε = 0.5 % using the CP localization law.

After carrying the identification shown previously in III.3.2, the self-consistency condition is analyzed using the localization law of Cailletaud-Pilvin. First, the macroscopic stress is calculated :

$$\Sigma_{11} = E\left(E_{11} - E_{11}^{p}\right) + \nu\left(E_{22} + E_{33}\right) \quad \text{(III-25)}$$

where E is the elastic modulus, Σ_{11}, E_{11}, E_{22}, E_{33} and E_{11}^{p} are components of macroscopic stress, strain and plastic strain.

The other components of Σ are zeros because of the tension-compression uniaxial loading condition considered in this study:

$$\Sigma_{22} = \Sigma_{33} = \Sigma_{12} = \Sigma_{13} = \Sigma_{23} = 0 \quad \text{(III-26)}$$

According to the self-consistency condition, the macroscopic stresses are calculated by:

$$\underline{\Sigma} = \langle \underline{\sigma}_g \rangle = \sum_g f_g \, \underline{\sigma}_g \quad \text{(III-27)}$$

Components of $\underline{\Sigma}$ calculated with macroscopic conditions (EQ. III-25 and EQ. III-26) are compared to the average of granular stresses obtained from EQ. III-27. A maximal difference of 1×10^{-13} can be seen in the first 192 cycles. So the self-consistency condition in stress can be considered as satisfied using the Cailletaud-Pilvin localization law.

Moreover, it should be noted that the self-consistency condition in strain using the Cailletaud-Pilvin localization law is not verified in this study. However, this condition is satisfied at least for plastic strains, because of the homogenization step adopted in this study, as seen in EQ. III-16.

➢ CONCLUSION

In this chapter, a self-consistent model has been chosen to simulate the mechanical behavior of the austenitic stainless steel studied. The analysis of the material microstructure led to choose an isotropic distribution of spherical grains to describe the elementary homogeneous volume. The localization law proposed by Cailletaud and Pilvin was selected to simulate the cyclic experimental tests. In order to favor a numerical description based on physical mechanisms, a crystalline constitutive law based on the evolution of dislocation densities in slip planes was selected.

The parameters introduced were identified using three ways: direct measurement on experimental results (E), obtained from the literature ($\upsilon, b, \rho, K, n, L$), or identified with an inverse method based on a genetic algorithm ($\tau^0, h, y_c, D, \delta$). This last method was carried out using the first 5 cycles of a tension-compression cyclic test with a strain amplitude of 0.5 %. Simulated results are in globally good agreement with the experimental ones. Moreover, the self-consistent condition has been verified during the simulation of a cyclic test.

IV. EXPERIMENTAL ANALYSIS OF THE CRACK INITIATION

This chapter aims at analyzing the plasticity and crack initiation in the material studied during low-cycle fatigue. A specific device was used to observe the surface of the specimen during the fatigue test without demounting it. In order to establish grain orientations and positions in the surface zone analyzed, a scan of this zone using Electron Back Scatter Diffraction (EBSD) was carried out after the test. The sites for crack initiation were identified. Attention was specifically focused on intragranular crack initiation, in order to establish experimental data aiming at validating a crack initiation criterion at the grain scale. For this purpose, a large surface was studied, which enables to use a large statistical experimental data set. The orientations of slip systems associated to microcracks were analyzed. Digital image correlation was used to calculate displacement fields at the grain scale between images taken during the test in order to determine the time of crack initiation. Moreover, the influence of various orientation criteria on plasticity and crack initiation was also studied.

IV.1. EXPERIMENTAL PROCEDURE

IV.1.1. LOW-CYCLE FATIGUE TEST

Only one test was performed to analyze the crack initiation during low-cycle fatigue. As the Laboratory of Mechanics of Lille does not own any EBSD system, the measurement of crystallographic orientations lies on collaborations with other laboratories which is more time-consumer. Having at our disposal only one test with the crystallographic orientations, we made the choice to carry it out at a strain amplitude for which data exist in the literature in order to compare the results obtained.

The fatigue test was carried out on a servohydraulic tension-compression testing machine (FIG. IV.1) in Rosario, Argentina. The load cell had a capacity of 100 kN and the range for the extensometer was 10 %. A plate specimen was machined from the as-received sheet, following the sketch given in FIG. IV.2. The specimen had a useful part of 23.72 mm in length, 6 mm in width, and 3.6 mm in depth. It was mechanically polished down to 1 µm grade diamond paste. In order to reveal grain boundaries, the specimen was then chemically etched in a solution composed of 3 vol HCl, 1 vol HNO_3 for 40 s. The time for chemical etching should be carefully controlled in order that the grain boundaries or twin boundaries are not too much attacked, which may be the preferential crack initiation sites.

The test was controlled in longitudinal strain measured by an extensometer with a gauge length of 20 mm. The cyclic test was carried out under total strain control. The waveform of the fatigue cycle was symmetrical triangular with a strain rate of 6.6×10^{-4} s^{-1} and strain amplitude of 0.5 %. Load and strain were recorded simultaneously during the cycling. The specimen was loaded/unloaded until 2000 cycles. The test was interrupted every 100 cycles (every 200 cycles after 1400 cycles) in order to take images of the surface of the specimen. The interruptions were done when $\varepsilon_a = 0$. At each interruption, 48 photos were taken. According to [Lindstedt 98], under the same strain amplitude, the crack density in austenitic stainless steels increases until about 1500 cycles and stabilizes. According to [Bataille 94], under a plastic strain amplitude of 4×10^{-3} (close to the maximal plastic strain amplitude in this study), after 2000 cycles, about 50 % of the cracks of type I will initiate. So observations after 2000 cycles should allow to highlight enough crack nucleation sites for the analysis.

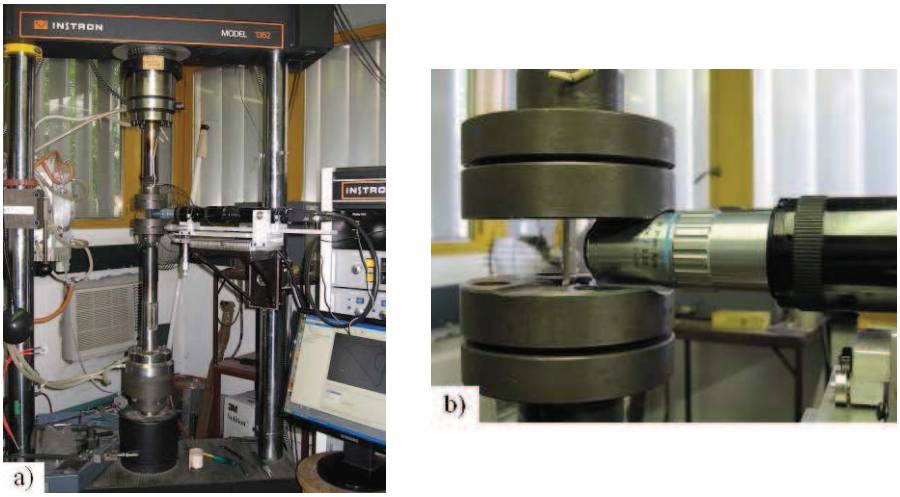

FIG. IV.1 - a) Experimental equipment; b) Specimen mounted in the grips and objective zoom.

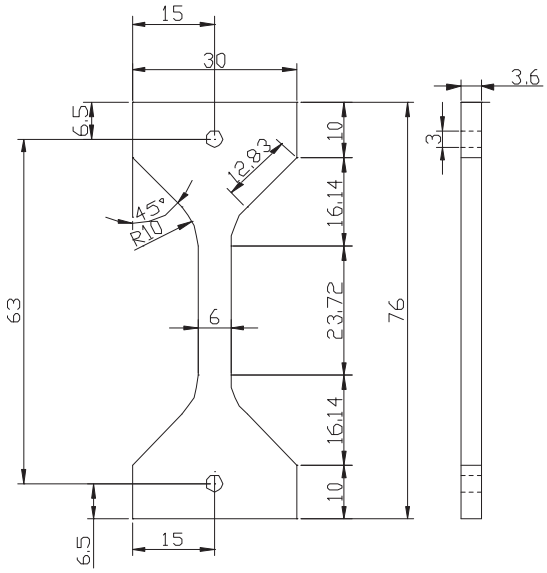

FIG. IV.2 - Drawing of the specimen.

The cyclic hardening/softening curve obtained during the test is shown in FIG. IV.3. The result is compared to the cyclic curve obtained without interruptions. It can be seen that the loading interruptions during the test do not modify the cyclic behavior of the material.

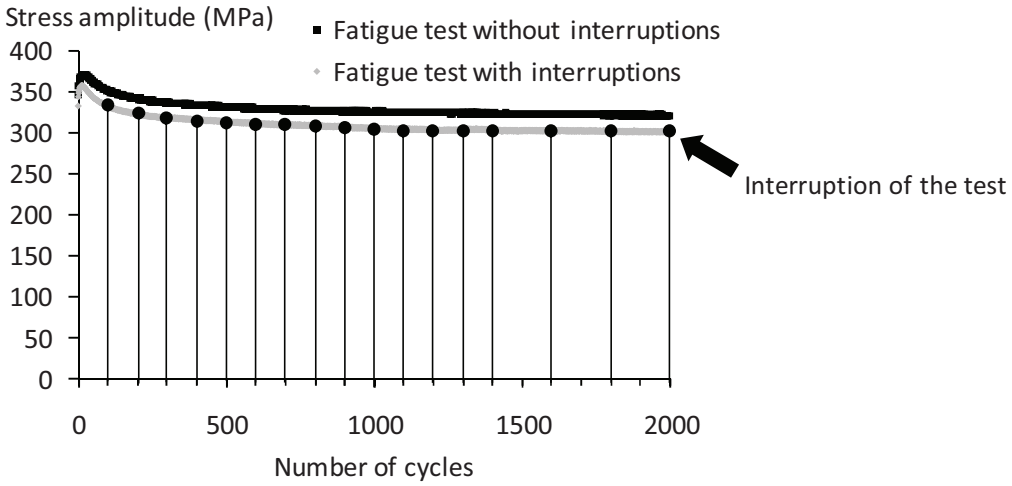

FIG. IV.3 - Cyclic hardening/softening curve obtained during the test presented here.

IV.1.2. OBSERVATION OF THE SPECIMEN SURFACE

In order to follow the surface damage evolution during the low-cycle fatigue test in real time and to acquire images at the microstructural scale, an in situ microscopy device was used [El Bartali 09]. This device consists of a 10-bit charge-coupled device (CCD) camera (1040 × 518 pixels) equipped with coaxial objective and zoom allowing to observe a zone of 140 µm × 70 µm at the objective magnification of 1.5 (see FIG. IV.1). This zone was enough small to reveal the fatigue damage at a microstructural scale, and enough large to see several grains in one image. This zone also ensured an acceptable quality of the images acquired, as the lighting is relatively homogeneous. The in situ observation device was mounted on the frame of the testing machine (FIG. IV.1a). Two displacement tables permitted to move the camera on a plan parallel to the studied specimen surface. The working distance (the distance between camera lens and object) of the system is only 13 mm. The grips were then machined in order to put the observation system at the right position. The movements of the camera are then very limited. The depth of field is less than 1 µm. This very small value requires a careful mechanical polishing and a slight chemical etching in order to avoid any roughness of the surface.

FIG. IV.4 shows an example of optical image taken after 2000 cycles. The grain boundaries, twin boundaries and slip markings appeared during the cycling can be seen. During the test, a domain of 8 × 6 (horizontal no. × vertical no.) images was observed. The total dimensions of the observation domain were 1080 µm × 400 µm. Images of this domain were first acquired before the test. Then, during the test, the machine was stopped every 100 cycles and 8 × 6 images were taken. Every image of a given zone was taken with a lot of precautions in order to represent exactly the same zone of the specimen, which enables to observe the fatigue damage changes at the specimen surface directly.

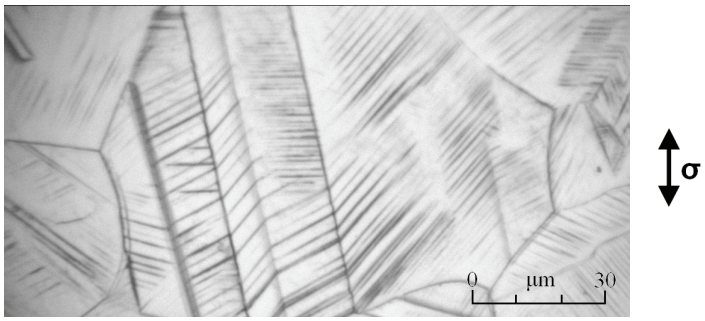

FIG. IV.4 - An optical image taken after 2000 cycles.

In order to verify the presence of initiated fatigue cracks, and also to identify the crack orientations, the same observation zone was then observed using a scanning electron microscope (SEM). Observations in this study were done in a scanning electron microscope HITACHI S3600, mainly on secondary electrons, in an accelerating voltage of 15 kV.

The optical observation zone was limited (1.08 mm × 0.4 mm), only three cracks initiated in this zone. In order to have enough cracks for a statistical analysis, two bigger zones (2.1 mm × 2.0 mm) were observed in SEM, the first one including the optical observation zone. 4 micro-indentations were made at the surface of specimen to precisely localize optical and SEM zones.

EBSD measurements were performed on the specimen surface after the mechanical test to obtain crystallographic orientations of surface grains and the grain boundary arrangement. EBSD scans were performed in beam control mode with a spatial resolution of 4 µm/step. The two zones (2.1 × 2.0 mm^2) observed in SEM were scanned, they contained about 12000 grains. FIG. IV.5b shows the orientations of the grains of one of the analyzed zone.

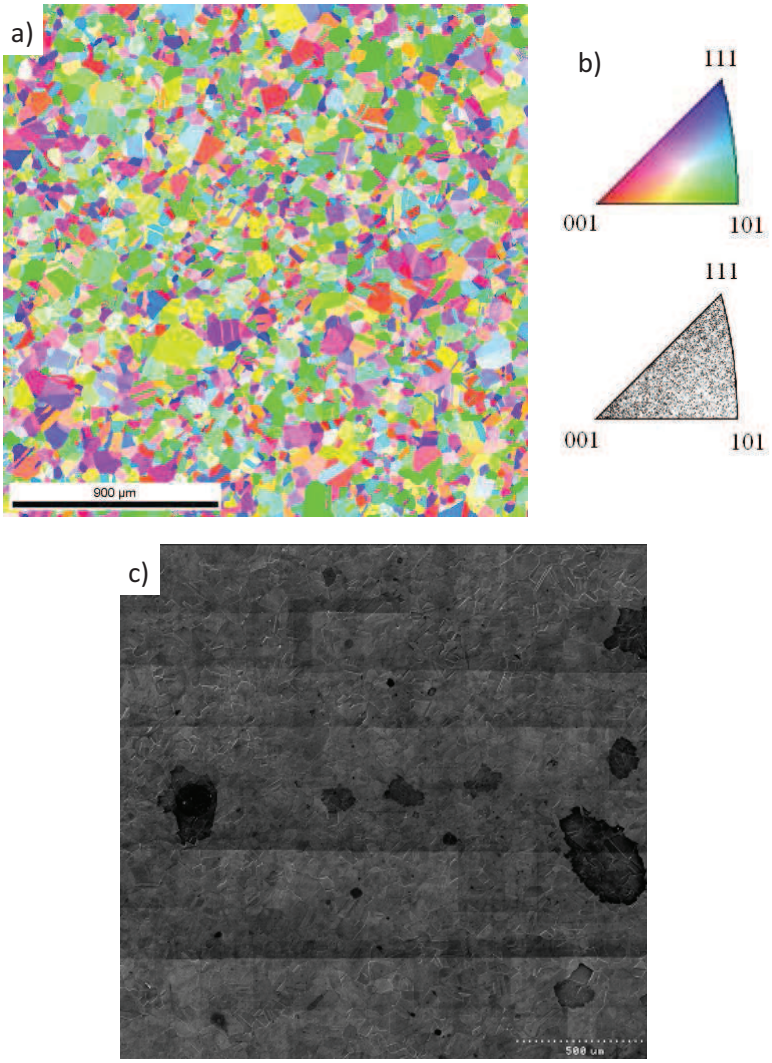

FIG. IV.5 - a) Grain crystallographic orientation following the transverse direction, b) grain locations in inverse pole figure [001], c) SEM image of the same zone taken at the end of test (2000 cycles)

IV.2. DEFINITION OF CRYSTALLOGRAPHIC CRITERIA

The orientation of a given crystal is generally known through its Euler angles with respect to the specimen reference. These angles are illustrated in FIG. IV.6, where (x, y, z) (resp. (X, Y, Z)) is the standard basis associated to the specimen (resp. the crystal). In this study, Y is the direction of macroscopic stress, Z is the normal to the specimen surface and X completes the direct orthonormal triad and corresponds to the transverse direction. The intersection of the xy and the XY coordinate planes is called the line of nodes (N). In other words, the line of nodes is the line perpendicular to both z and Z axis. φ_1, Φ, φ_2 correspond to three Euler angles defined by Bunge [Bunge 82] according to FIG. IV.6. φ_1 is the angle between the x-axis and the line of nodes. Φ is the angle between the z-

axis and the Z-axis. φ_2 is the angle between the line of nodes and the X-axis. φ_1 and φ_2 are defined between 0 and 2π and Φ between 0 and π.

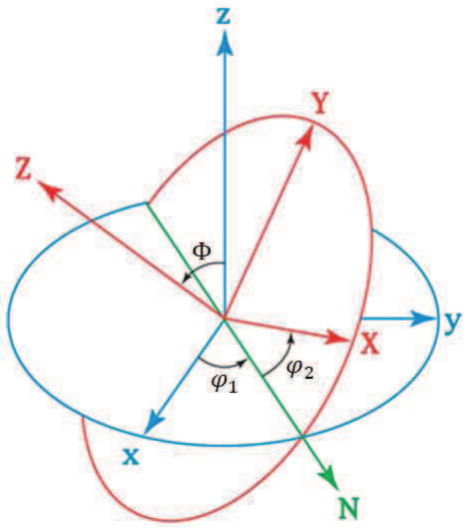

FIG. IV.6 - Euler angles.

The orientation matrix, $\underline{\underline{G}}$, transforms the global coordinates (x, y, z) into the local ones (X, Y, Z), based on the three Euler angles:

$$\underline{X}_{local} = \underline{\underline{G}} \cdot \underline{X}_{global} \tag{IV-1}$$

with

$$\underline{\underline{G}} = \begin{bmatrix} g_{11} & g_{12} & g_{13} \\ g_{21} & g_{22} & g_{23} \\ g_{31} & g_{32} & g_{33} \end{bmatrix} =$$

$$\begin{bmatrix} \cos\varphi_1 \cos\varphi_2 - \cos\Phi \sin\varphi_1 \sin\varphi_2 & \cos\varphi_2 \sin\varphi_1 + \cos\varphi_1 \cos\Phi \sin\varphi_2 & \sin\Phi \sin\varphi_2 \\ -\cos\Phi \cos\varphi_2 \sin\varphi_1 - \cos\varphi_1 \sin\varphi_2 & \cos\varphi_1 \cos\Phi \cos\varphi_2 - \sin\varphi_1 \sin\varphi_2 & \cos\varphi_2 \sin\Phi \\ \sin\varphi_1 \sin\Phi & -\cos\varphi_1 \sin\Phi & \cos\Phi \end{bmatrix} \tag{IV-2}$$

The inverse matrix of $\underline{\underline{G}}$, $\underline{\underline{G}}^{-1}$, transforms the local coordinates (X, Y, Z) into the global ones (x, y, z):

$$\underline{X}_{global} = \underline{\underline{G}}^{-1} \cdot \underline{X}_{local} \tag{IV-3}$$

with

$$\underline{\underline{G}}^{-1} = \underline{\underline{G}}^{T} = \begin{bmatrix} g_{11}^{-1} & g_{12}^{-1} & g_{13}^{-1} \\ g_{21}^{-1} & g_{22}^{-1} & g_{23}^{-1} \\ g_{31}^{-1} & g_{32}^{-1} & g_{33}^{-1} \end{bmatrix} =$$

$$\begin{bmatrix} \cos\varphi_1 \cos\varphi_2 - \cos\Phi \sin\varphi_1 \sin\varphi_2 & -\cos\Phi \cos\varphi_2 \sin\varphi_1 - \cos\varphi_1 \sin\varphi_2 & \sin\varphi_1 \sin\Phi \\ \cos\varphi_2 \sin\varphi_1 + \cos\varphi_1 \cos\Phi \sin\varphi_2 & \cos\varphi_1 \cos\Phi \cos\varphi_2 - \sin\varphi_1 \sin\varphi_2 & -\cos\varphi_1 \sin\Phi \\ \sin\Phi \sin\varphi_2 & \cos\varphi_2 \sin\Phi & \cos\Phi \end{bmatrix} \quad \text{(IV-4)}$$

In order to evaluate the influence of the orientation of a given grain on its facility to show crack initiation, three other angles or criteria have to be calculated: the Schmid factor, μ, the angle between slip markings at the surface and the loading axis, Π, and the angle between the gliding direction and the normal to the free surface, β.

The Schmid factor is used to determine the relation between the stress in the direction of the loading axis and the shear stress on a slip plane. As shown in FIG. IV.7, under the force F in the direction of the loading axis, the shear stress on the slip plane, τ, is expressed as:

$$\tau = \cos\chi \cdot \cos\theta \cdot F/S_0 \quad \text{(IV-5)}$$

where χ is the angle between the loading axis and the normal to the slip plane, θ is the angle between the slip direction and the loading axis, S_0 is the surface of the projected plane of the slip plane in the direction perpendicular to the loading axis. So the Schmid factor is:

$$\mu = \frac{\tau}{F/S_0} = \cos\chi \cos\theta = \left(\frac{\underline{n}_{sp}}{\|\underline{n}_{sp}\|} \cdot \frac{\underline{\sigma}}{\|\underline{\sigma}\|}\right) \cdot \left(\frac{\underline{SD}}{\|\underline{SD}\|} \cdot \frac{\underline{\sigma}}{\|\underline{\sigma}\|}\right) \quad \text{(IV-6)}$$

where $\underline{n}_{sp}$ is the normal to the slip plan, $\underline{SD}$ is the slip direction, and $\underline{\sigma}$ is the stress normal to the slip plane.

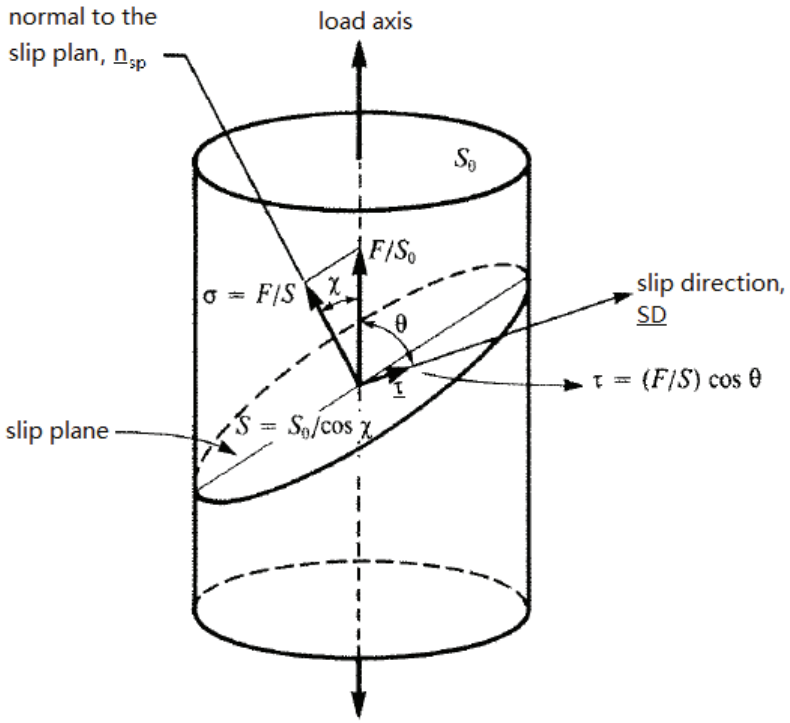

FIG. IV.7 - Necessary angles and vectors for the calculation of Schmid factor [Schmid 50].

In a grain of an austenitic strainless steel, there are 12 potential slip systems to be activated under load. For example, under tensile stress if the loading axis is the global axis $\underline{Y}$, the unit tensile stress can be expressed in the local coordinates as:

$$\underline{\sigma} = \underline{Y} = \underline{\underline{G}} \cdot \begin{pmatrix} 0 \\ 1 \\ 0 \end{pmatrix} = \begin{pmatrix} g_{12} \\ g_{22} \\ g_{32} \end{pmatrix} \qquad \text{(IV-7)}$$

FIG. IV.8 shows the angle between, on the one hand, the intersection of the slip plane and the surface and, on the other hand, the loading axis, Π.

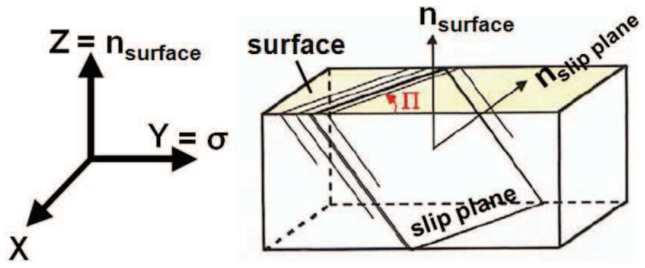

FIG. IV.8 - Angle between the intersection of the slip plane and the surface and the loading axis, Π [Mineur 00a].

As seen in FIG. IV.8, the intersection of the slip plane and the surface can be obtained by calculating the cross product of $\underline{n}_{sp}$ and $\underline{n}_{surface}$. The loading axis, $\underline{\sigma} = \underline{Y}$. So $\cos\Pi$ can be calculated as:

$$\cos\Pi = \frac{(\underline{n}_{sp} \wedge \underline{n}_{surface}) \cdot \underline{\sigma}}{\|\underline{n}_{sp} \wedge \underline{n}_{surface}\| \cdot \|\underline{\sigma}\|} = \frac{(\underline{n}_{sp} \wedge \underline{n}_{surface}) \cdot \underline{Y}}{\|\underline{n}_{sp} \wedge \underline{n}_{surface}\| \cdot \|\underline{Y}\|} \tag{IV-8}$$

In order to fix Π, $\sin\Pi$ is needed, which is equal to $\cos(90° - \Pi)$. It can be seen from FIG. IV.8 that $(90° - \Pi)$ is the angle between the intersection of the slip plane and the surface and the transverse axis X. So,

$$\sin\Pi = \cos(90° - \Pi) = \frac{(\underline{n}_{sp} \wedge \underline{n}_{surface}) \cdot \underline{X}}{\|\underline{n}_{sp} \wedge \underline{n}_{surface}\| \cdot \|\underline{X}\|} \tag{IV-9}$$

The normal to the surface, $\underline{n}_{surface}$, and the transverse axis, $\underline{X}$, in the local coordinates are respectively:

$$\underline{n}_{surface} = \underline{Z} = \underline{\underline{G}} \cdot \begin{pmatrix} 0 \\ 0 \\ 1 \end{pmatrix} = \begin{pmatrix} g_{13} \\ g_{23} \\ g_{33} \end{pmatrix} \tag{IV-10}$$

$$\underline{X} = \underline{\underline{G}} \cdot \begin{pmatrix} 1 \\ 0 \\ 0 \end{pmatrix} = \begin{pmatrix} g_{11} \\ g_{21} \\ g_{31} \end{pmatrix} \tag{IV-11}$$

The loading axis $\underline{\sigma}$ in the local coordinates is calculated in EQ. IV-7.

The 3rd parameter under research is the angle between the slip direction and the normal to the free surface, β, as seen in FIG. IV.9.

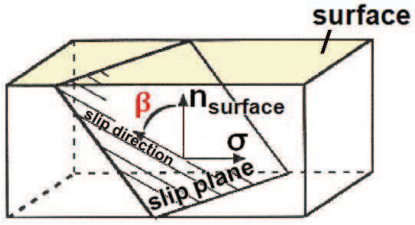

FIG. IV.9 - Angle between the slip direction and the normal to the surface, β [Mineur 00a].

The calculation of the angle β is similar to that of angle Π:

$$\cos\beta = \frac{\underline{SD} \cdot \underline{n}_{surface}}{\|\underline{SD}\| \cdot \|\underline{n}_{surface}\|} \tag{IV-12}$$

In order to simplify the calculation, the global coordinates are used and only $\cos\beta$ was calculated.

If angle β obtained from EQ. IV-12 lies within $(\pi/2, \pi]$, $(\pi - \beta)$ will be chosen as β. This treatment facilitates the analysis of the distribution of β within the domain of $[0, \pi/2]$.

IV.3. ANALYSIS OF THE SURFACE PLASTICITY

A domain of 1080 µm × 400 µm was followed during the test using the in situ microscopy device. Images of a same zone obtained before the test, after 500 cycles, and after 2000 cycles are shown in FIG. IV.10. These images show the fatigue changes in an observation zone during the cyclic test. Before the test, only grain boundaries and twin boundaries could be seen. After 500 cycles, several slip lines appeared in some grains. After 2000 cycles, slip lines intensified and could be seen in almost all grains. In some grains, several slip systems were activated.

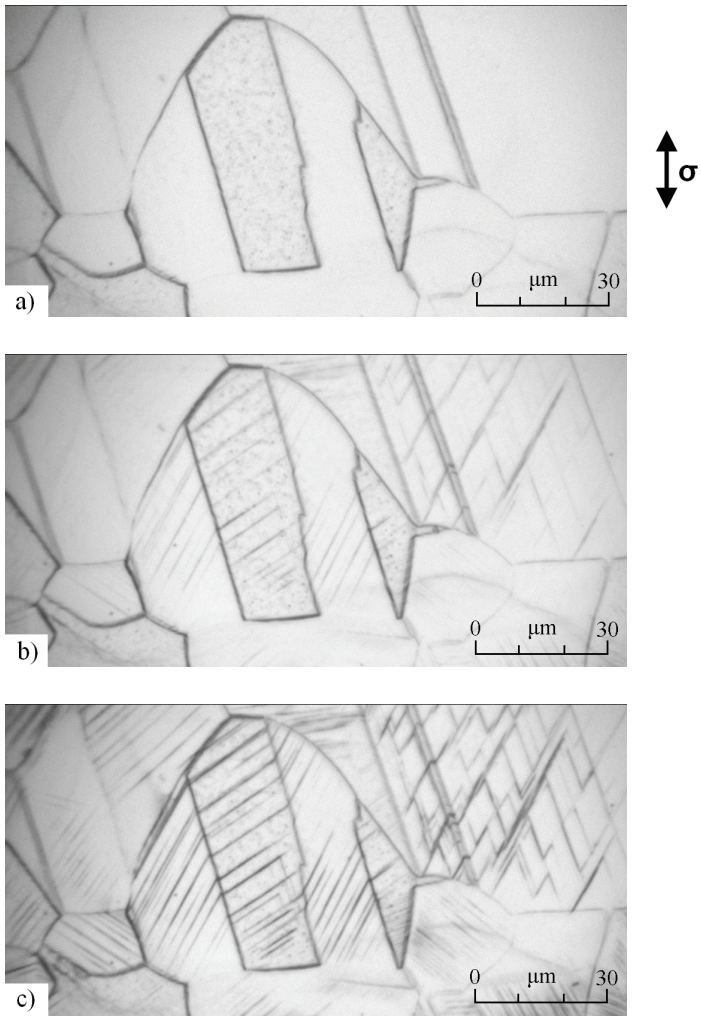

FIG. IV.10 - Optical images of a same zone taken before the test a), after 500 cycles b) and 2000 cycles c).

The analysis of these images allowed to characterize the plastic activity during the cycling. At various numbers of cycles, the number of grains showing slip markings was counted (among the 366 grains of the observation zone); the results are shown in FIG. IV.11. About two thirds of the grains showed

plastic activity after 300 cycles, they were about 90 % after 2000 cycles. As slip markings are not clear in some grains, the uncertainty of the data is also calculated, which decreases when the number of cycles increases.

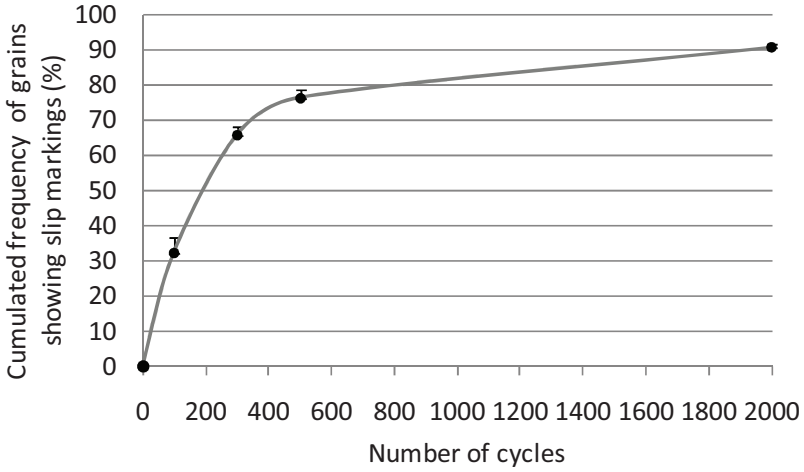

FIG. IV.11 - Percentage of grains showing slip markings during cycling.

Using high magnification SEM images obtained after 2000 cycles, the slip systems activated can be identified in each grain of the observed zone. From Euler angles measured, for each potential slip system (12 systems), the Schmid factor μ and the angle Π between the possible slip markings appeared at the free surface and the loading axis were calculated. A slip system is supposed to be activated when associated slip markings are observed at the surface. For each slip marking, the experimentally measured angle Π was compared to those calculated above. The slip plan with the Schmid factor closest to the measured value of Π was considered activated. The slip direction is determined making the assumption that the activated slip system is that with the highest Schmid factor in the three possible slip systems.

In most grains, only 1 or 2 slip systems are activated. The activated slip system usually has the highest Schmid factor, except in some rare cases. It is important to note that the grains in a polycrystal are in a triaxial state and their deformations are also influenced by the deformations of neighbour grains. This can explain the activation of a slip system of which the Schmid factor is not the highest.

FIG. IV.12 presents the cumulative frequency of the highest Schmid factors of all potential slip systems in the analyzed zone. It can be seen that for the grains of the analyzed zone, the highest Schmid factor is always higher than 0.30. This distribution was compared with that of the highest Schmid factors of the activated slip systems in 178 grains showing plasticity activity. The two

distributions are globally in good agreement confirming the validity of the criterion of the highest Schmit factor for slip system activation.

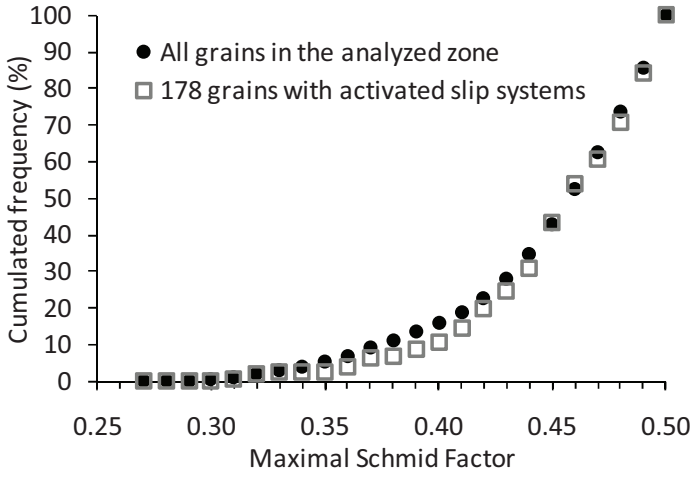

FIG. IV.12 - Curves of cumulative frequency of, in the one hand, the maximal Schmid factor obtained in all the grains of the analyzed zone and, in the other hand, the Schmid factor of the activated slip system in 178 grains showing plastic activity.

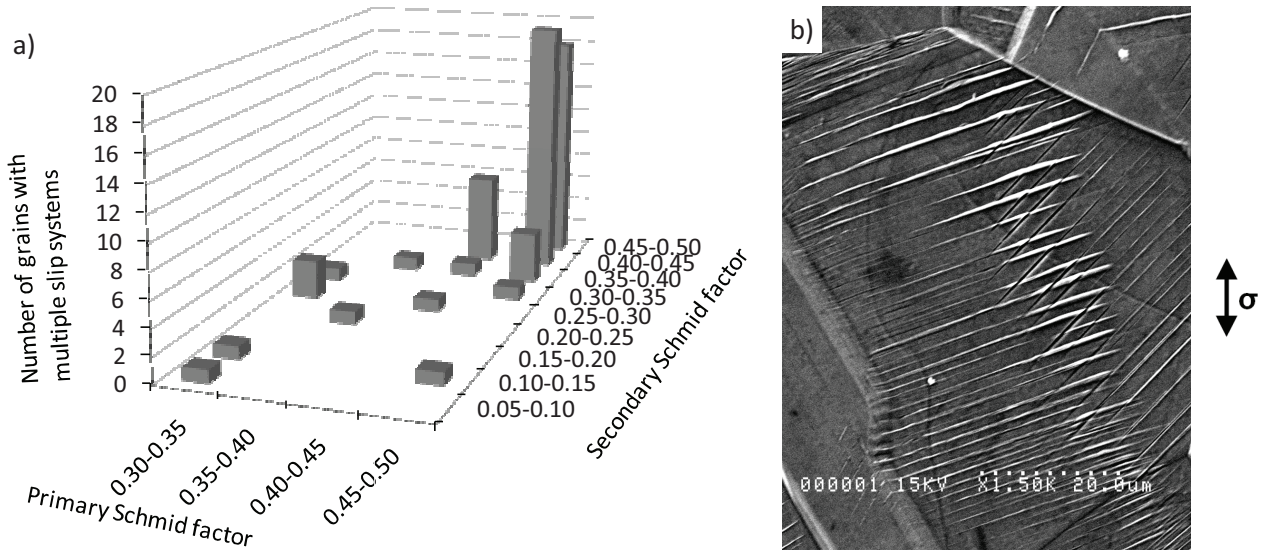

FIG. IV.13 - a) Distribution of primary and secondary Schmid factors in grains showing multiple slip systems activated, b) a grain with two activated slip systems observed in SEM.

Some grains of the analyzed zone present multiple slip. Their Schmid factors have been specifically analyzed. It can be seen in FIG. IV.13 that the primary Schmid factor was always higher than 0.40, and in 76% of the grains showing multiple slip, the secondary Schmid factor was also higher than 0.40. As it can be seen in FIG. IV.10 and FIG. IV.14a, the slip markings are straight and fine, parallel to each other. These characteristics are typical of the dislocation planar slip, which occurs in austenitic steels (FCC crystallographic structures) all the more easily when the nitrogen content is high [Mateo 96] [Degallaix 84] [Degallaix 95] [Kruml 97]. Although the content in nitrogen of the studied alloy is not known, these observations indicate that it should be relatively high. Moreover, the fact that several slip systems with very high Schmid factors activate confirms this assumption. As the cross-slip is not easy, in certain grains, two slip systems are activated to accommodate the plastic deformation.

IV.4. CRACK INITIATION

IV.4.1. CRACK INITIATION SITES

All cracks in the SEM observation zone were looked for and analyzed, which represents a zone of 8.4 mm^2. The crack density after 2000 cycles was 12 cracks /mm^2. It depends on the loading conditions (strain amplitude, environment) [Mineur 00a, b] and on the material (grain size, nitrogen content) [Lindstedt 98]. Four crack initiation origins were found: crack initiated in persistent slip bands (PSB) (FIG. IV.14a), in grain boundaries (GB) (FIG. IV.14b), in twin boundaries (TB) (FIG. IV.14c), and from inclusions (FIG. IV.14d). Examples of these various crack origins are shown in FIG. IV.14. As only few cracks initiated from inclusions, this crack origin has not been considered. The distributions of PSB, GB and TB cracks are shown FIG. IV.15. It can be seen that, at room temperature, under a medium strain amplitude ($\varepsilon_a = 5 \times 10^{-3}$, $\varepsilon_a^p \approx 3.3 \times 10^{-3}$) after 2000 cycles, cracks appear mainly in PSBs (51.3 %) and in grain boundaries (42.5 %). Cracks initiated in twin boundaries (6.2 %) occupy only a very little proportion. The results for zone 1 and zone 2 are also shown, respectively. It can be seen that there is a difference of about 10 % in the percentage of PSB and GB cracks in these two big zones, which means that the surface of only 4.2 mm^2 is not enough to establish statistics for the distribution of crack sites. A bigger zone is then needed. In this study, the results of the zones 1 and 2 are used. However, in order to be sure that the surface of the two zones, 8.4 mm^2, is enough and representative to establish statistics, it would be necessary to establish statistics on zones of increasing size.

These results can be compared to those of Mineur [Mineur 00a] and Kamaya [Kamaya 09], both obtained in cyclically strained type AISI 316 austenitic stainless steels under various strain amplitudes.

It can be noted that the highest the strain amplitude, the less cracks initiate in persistent slip bands, which is consistent with observations showing that in the high cycle fatigue domain cracks initiate mainly from PSBs [Mughrabi 83].

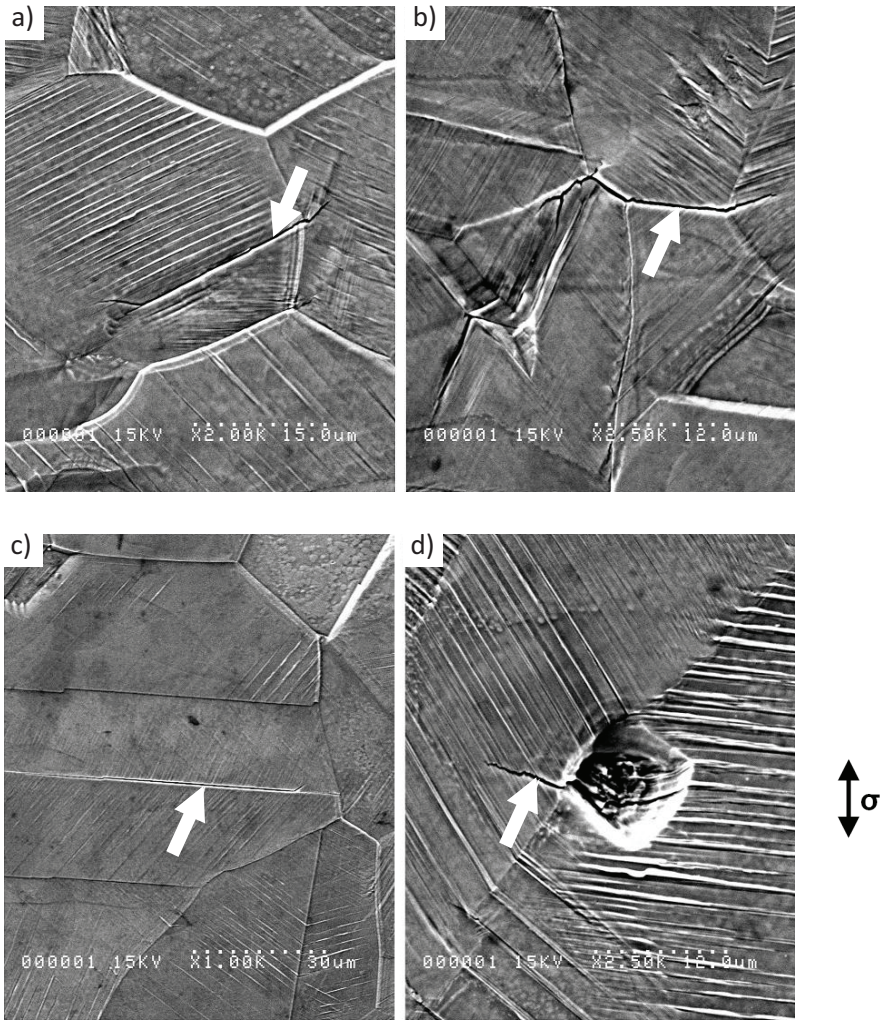

FIG. IV.14 - Cracks initiated in a PSB a), in grain boundaries b), in twin boundaries c), and from an inclusion d). Cracks are indicated by white arrows.

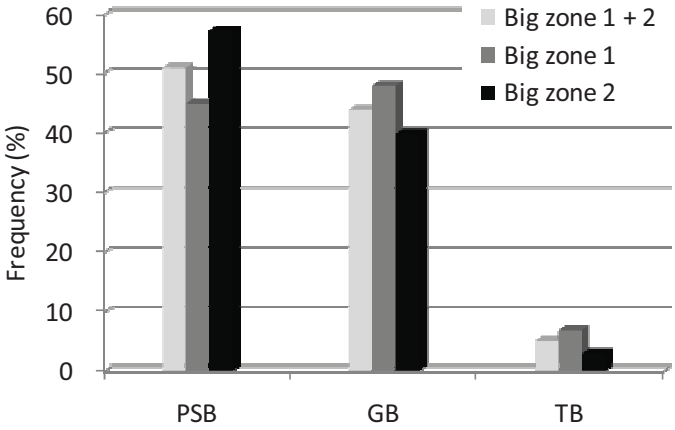

FIG. IV.15 - Distribution of various crack initiation sites observed in big zones 1 and 2.

IV.4.2. ANALYSIS OF CRYSTALLOGRAPHIC CRITERIA

In this section, the crack initiation will be studied from the crystallographic point of view. The results concerning three crystallographic parameters in section IV.2 and their combinations will be shown:

- Orientation of slip system towards the loadings axis: Schmid factor μ
- Orientation of the cracks on the surface: angle between the intersection of the slip plane and the surface and the loading axis Π
- Orientation of slip system towards the normal to the free surface: angle between the slip direction and the normal to the free surface β

Before presenting the results, it is necessary to introduce some notations. In the analysis below, the maximal Schmid factor (SF_{max}) is the maximal one within those of all the 12 slip systems in a grain. We called 1st and 2nd Schmid factors the maximal and the second maximal Schmid factors corresponding to the initiated cracks in a grain.

➢ ORIENTATION OF SLIP SYSTEM TOWARDS THE LOADINGS AXIS, μ

FIG. IV.16 shows the cumulated frequency of the maximal Schmid factor, in the one hand, in all the grains in the zone studied, and, in the other hand, in the 91 grains showing PSB cracks. It can be seen that no crack initiated in a grain with a maximal Schmid factor less than 0.40. All the grains showing cracks are then oriented for single slip. The cumulated frequency of maximal Schmid factor in grains showing PSB cracks is much lower than that obtained in all grains, there are many grains showing cracks with a very high maximal Schmid factor. This means that crack initiation is much easier in grains with very high maximal Schmid factors.

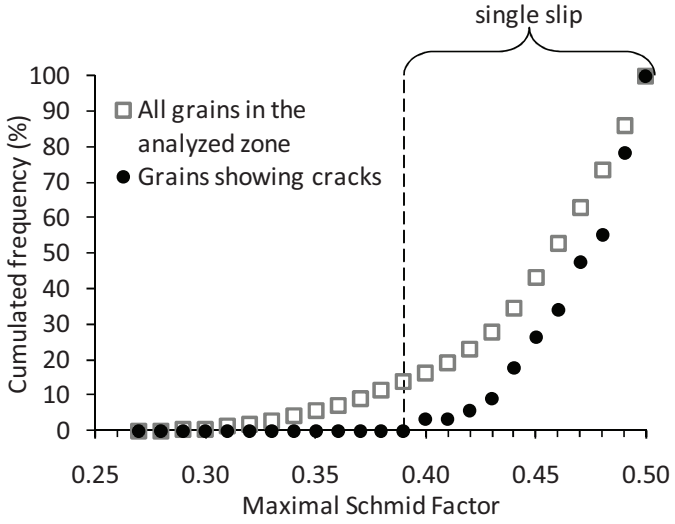

FIG. IV.16 - Cumulated frequency of maximal Schmid factors of, in the one hand, all the grains, and, in the other hand, the grains showing PSB cracks.

In FIG. IV.17, the Schmid factors associated to cracked slip systems for the grains showing PSB cracks are compared to the maximal Schmid factors of all grains in the studied zone. On the contrary to FIG. IV.16, the two curves are in good agreement. This shows that in many grains, the slip system which leads to crack initiation is not the slip system with the maximal Schmid factor. The Schmid factor is thus not the only criterion to be considered to explain crack initiation.

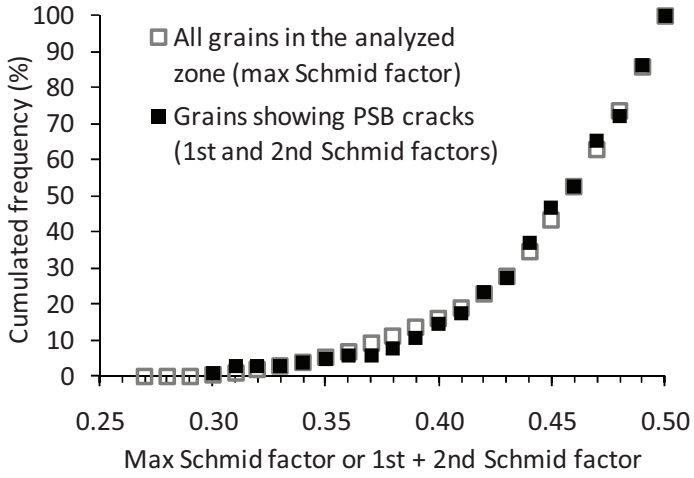

FIG. IV.17 - Cumulated max SF in all grains and SF associated to cracked slip system in grains showing PSB cracks.

In order to evaluate how many crack appear on the best oriented slip system (in the sense of the Schmid factor), grains were divided into three groups, depending on the value of the Schmid factor of the slip system where crack initiated. Grains of the 1^{rst} group are grains where cracks initiated in the slip system with the maximal Schmid factor.

$$SF_{crack} = SF_{max} \quad \text{(IV-13)}$$

Grains of the second group are grains where cracks initiated in slip system with high Schmid factor, but less than the maximal Schmid factor in the grain.

$$SF_{max} - 0.035 < SF_{crack} < SF_{max} \quad \text{(IV-14)}$$

Grains of the third group show cracks initiated in bad oriented slip systems.

$$SF_{crack} < SF_{max} - 0.035 \quad \text{(IV-15)}$$

FIG. IV.18 and FIG. IV.19 present the cumulated Schmid factors and the distribution of Schmid factors of the slips systems associated to the crack in grains showing PSB cracks, considering these three groups. Most of the cracks (64 %) initiate on the slip system with the highest Schmid factor, 18 % of

the cracks have a Schmid factor close to the maximal Schmid factor, and 19 % of the cracks have a Schmid factor lower than SF_{max} - 0.035. These figures show that cracks having the maximal Schmid factor (1st group) have SF mainly in the range [0.44, 0.50]. For the 2nd group, they are mainly in the range [0.44, 0.48] and for the 3rd group, in the range [0.30, 0.44].

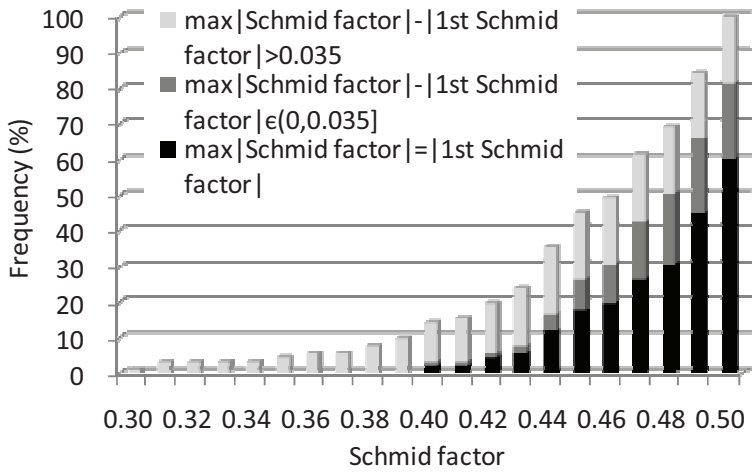

FIG. IV.18 - Cumulated frequency of Schmid factors associated to cracked slip systems in the grains showing PSB cracks. Grains have been divided into three groups, depending of their Schmid factor value.

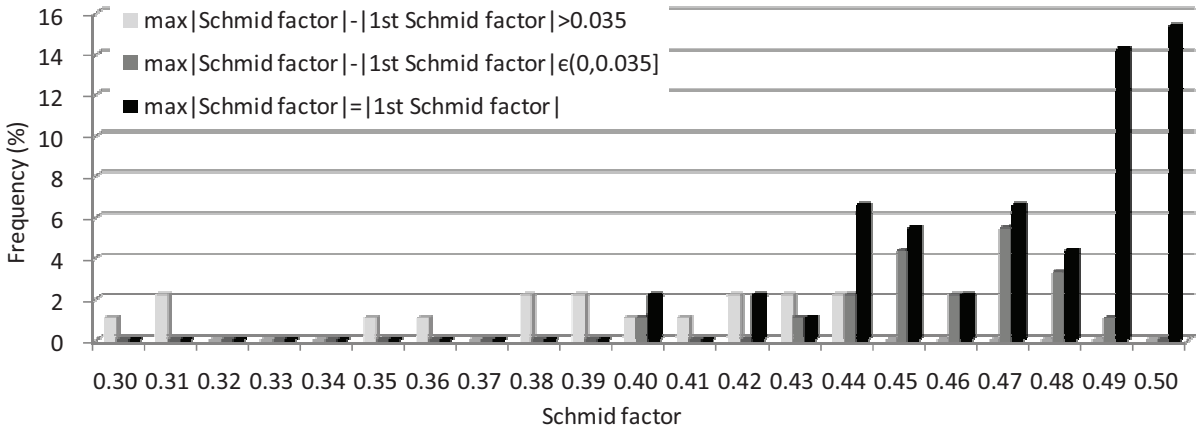

FIG. IV.19 - Distribution of Schmid factors associated to cracked slip systems in the grains showing PSB cracks. Grains have been divided into three groups, depending of their Schmid factor value.

➢ ORIENTATION OF THE CRACKS ON THE SURFACE, Π

FIG. IV.20 presents the crack orientation distribution of cracks initiated in PSBs in the two zones analysed. 91 PSB cracks initiated in 91 grains were analyzed. Angle Π between the loading axis and each crack was measured. Quasi no crack initiated in the domain $\Pi \in [0, 40°]$. A quasi-symmetrical triangular distribution can be observed, centered around the range [60, 70°], which represents about 25 % of the cracks initiated in PSBs. About 70 % of the cracks initiate with an angle $\Pi \in [50, 80°]$.

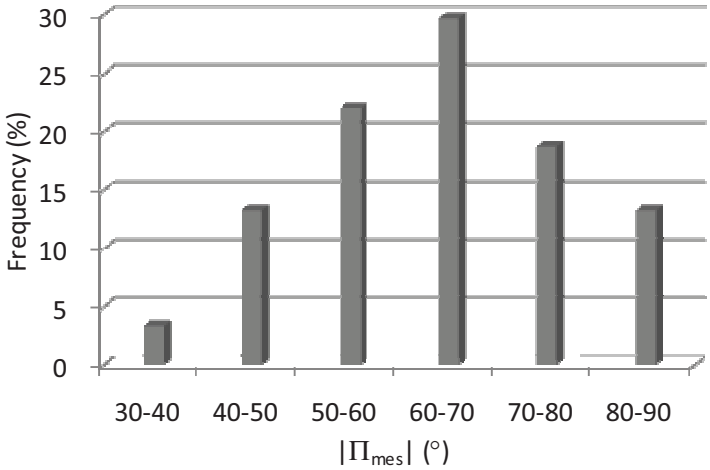

FIG. IV.20 - Crack orientation distribution (for cracks initiated in PSBs).

Schmid factors of slip systems associated to these cracks were systematically calculated. The crack orientation distribution is plotted in FIG. IV.21 with respect to the Schmid factor of the slip system associated to the crack. For the cracks with low Schmid factors (3rd group), $\Pi \in [60, 90°]$.

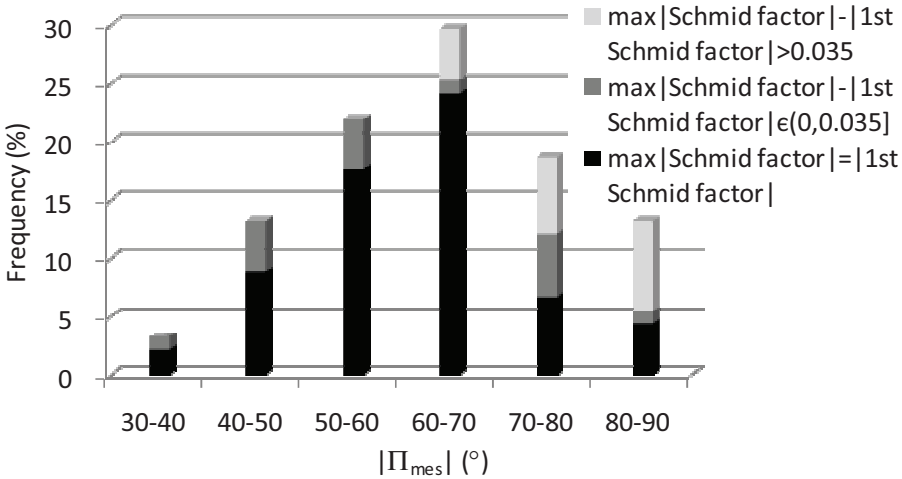

FIG. IV.21 - Crack orientation distribution with respect to the Schmid factor (for cracks initiated in PSBs). Cracks are split into three groups depending on the value of the Schmid factor associated to the crack compared to the highest Schmid factor of the grain.

FIG. IV.22 shows the distribution of angles Π of the slip systems with highest Schmid factor in grains showing PSB crack. These slip systems are split into two categories: slip systems showing cracks or not. It can be seen that the slip systems with the highest Schmid factor showing no crack are not distributed homogeneously, they are much more numerous in the range Π belonging to [30, 50°]. In other words, on the one hand, if the slip system with the maximal Schmid factor makes an angle Π near or less than 45° to the loading direction, it will probably not lead to a crack, which will appear on a different slip system. On the other hand, if it makes an angle Π higher than 45°, a crack may likely initiate in this slip system. These observations agree with the classification introduced by Miller [Miller 73]. Among slip systems good oriented to simple gliding, he showed that two slip systems have a particular orientation toward the surface: systems A and B. In both cases, slip plans make an angle of 45° to the direction of loading, but the slip direction changes. For system A, the slip direction is parallel to the free surface, and no intrusion-extrusion is created during the gliding (FIG. IV.23a). On the contrary, for system B, the slip direction makes an angle of 45° to the free surface, and the gliding along this slip system will create roughness at the free surface (FIG. IV.23b), where micro cracks can initiate.

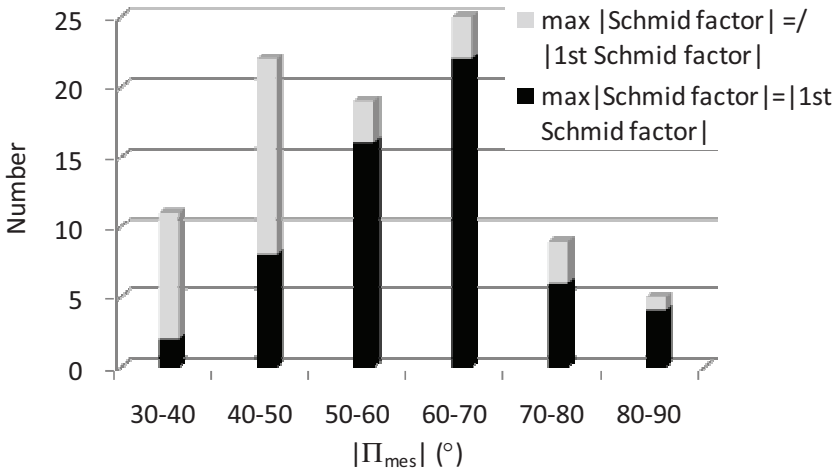

FIG. IV.22 - Distribution of angles Π of the slip systems with highest Schmid factor in grains showing PSB crack.

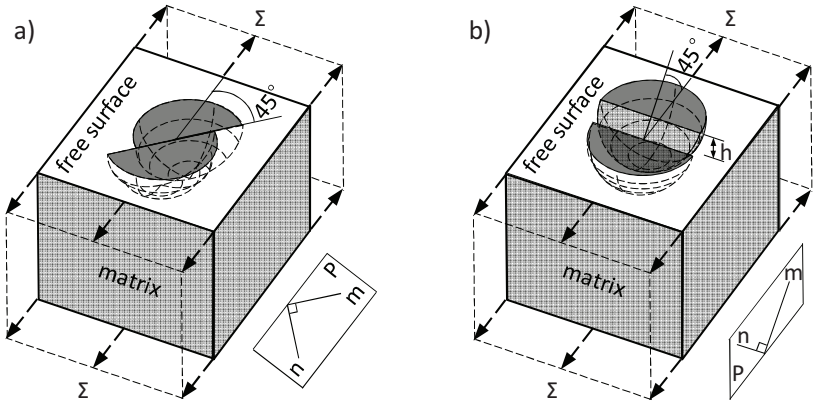

FIG. IV.23 - a) System A; b) System B (m, slip direction; n, normal of slip plane h, step height).

➢ ORIENTATION OF SLIP SYSTEM TOWARDS THE NORMAL TO THE FREE SURFACE, β

In this section, the study on angle β, the angle between slip direction and the normal to the free surface, is carried out. As above, 91 PSB cracks initiated in 91 grains of the two zones were analyzed. Quasi no crack initiated in the domain β Є [0, 20°]. A quasi-symmetrical triangular distribution can be observed, centered around the range [50, 60°], which represents about 25 % of the cracks initiated in PSBs. Over 70 % of the cracks initiated with an angle β in the domain [40, 70°]. These results are in good agreement with results of the literature obtained on isotropic specimens [Mineur 00b]. However, the texture of the material has also great influence on the crack distribution, as shown by Mineur [Mineur 00b].

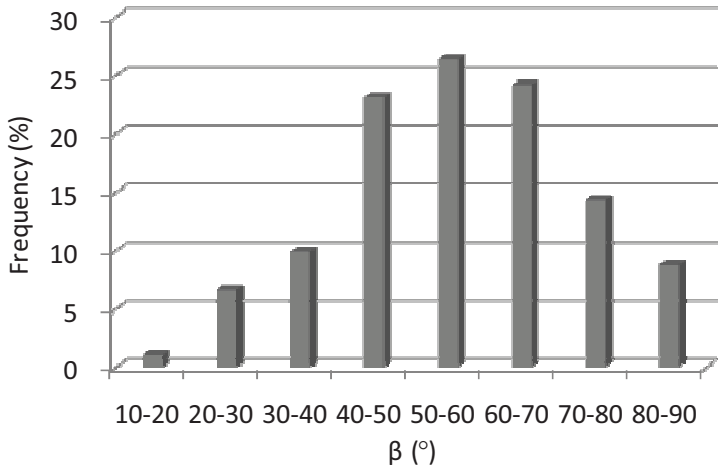

FIG. IV.24 - Distribution of angles β in the grains showing cracks.

The orientation distribution of the slip direction toward the normal to the surface (β) is plotted in FIG. IV.25a with respect to the Schmid factor of the slip system associated to the crack. For the cracks with low Schmid factors (3rd group), angle β belongs to [10, 70°]. It can be seen in FIG. IV.25b that in these grains, the slip systems having the highest Schmid factor have a slip direction mostly in the range [60, 90°], which corresponds to slip systems having a small emerging volume (FIG. IV.26) and are also systems of type B. Using dynamic dislocation simulations, Déprés proposed a criterion for crack initiation under biaxial cyclic loadings in slips system oriented for double glide and having the highest emerging volume.

Slip systems showing crack initiation in our case are not oriented for double glide, but the rule of the maximum emerging volume is still valid, as it can be seen in FIG. IV.25 that the majority of slip systems too badly oriented in the sense of this criterion does not lead to crack initiation which occurs in a different slip system. Under uniaxial loading, the rule of the maximum emerging volume is equivalent to the analysis proposed by Miller.

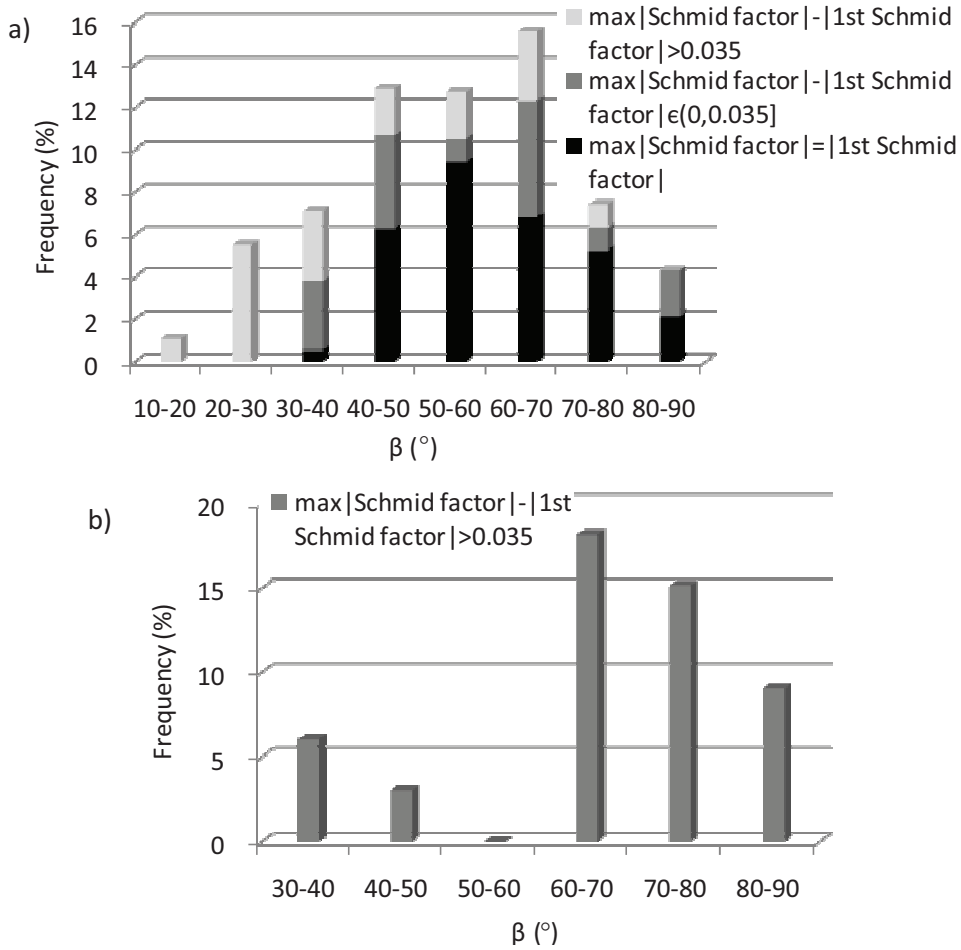

FIG. IV.25 - a) Distribution of angles β of the slip systems associated to cracks with respect to the Schmid factor (for cracks initiated in PSBs). Cracks are split into three groups depending on the value of the Schmid factor associated to the crack compared to the highest Schmid factor of the grain. b) Distribution of β of the slip systems having the highest Schmid factor in grains showing cracks.

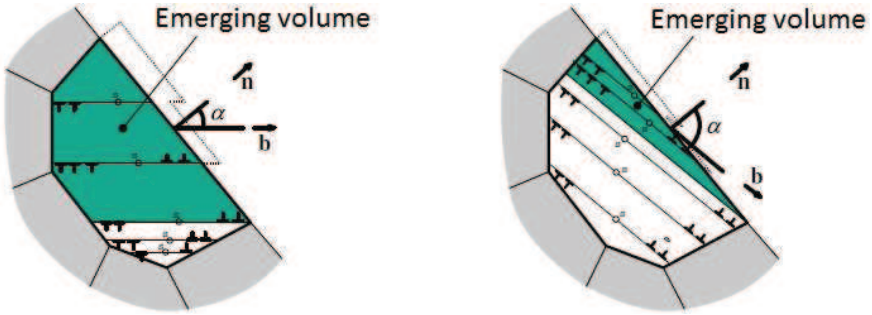

FIG. IV.26 - Assumption of the maximum emerging volume [Déspres 04].

It is interesting to consider the effect of coupling angles β and Π on crack initiation. FIG. IV.27 shows the combined distribution of these two angles, in the one hand, for the best oriented slip system in all the grains and, in the other hand, for slip systems associated to initiated PSB cracks. Values of β and Π of slip systems with the highest Schmid factor cover a large domain (FIG. IV.27a), highlighted by the white dotted lines. It is clear that cracks initiated only in a smaller domain limited by the white dotted lines in FIG. IV.27b. The maximum is obtained when 50° < β < 60° and 60° < Π < 70°. This clearly indicates a correlation between the values of β and Π for crack initiation. However, in the lower right corner of this domain, where β is maximal but Π minimal, there exists a small domain with only few initiated cracks.

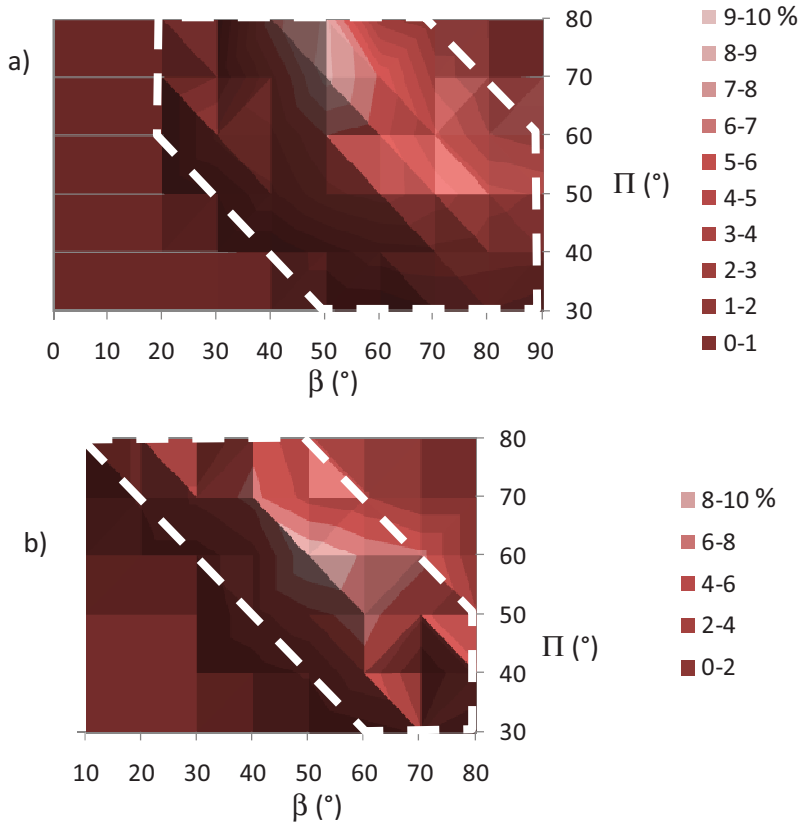

FIG. IV.27 - Distribution of angles β and Π of a) slip system with the highest Schmid factor and b) initiated PSB cracks.

The distribution of the angles β and Π of slip systems having the maximal Schmid factor of their grain but not turned into cracks is also analyzed. As shown in FIG. IV.28, most cracks with β ∈ [60, 90°] and Π ∈ [30, 50°] (zone limited by white dotted lines) did not initiate during the fatigue test. This corresponds to the domain showing few slip systems in the lower right corner in FIG. IV.27.

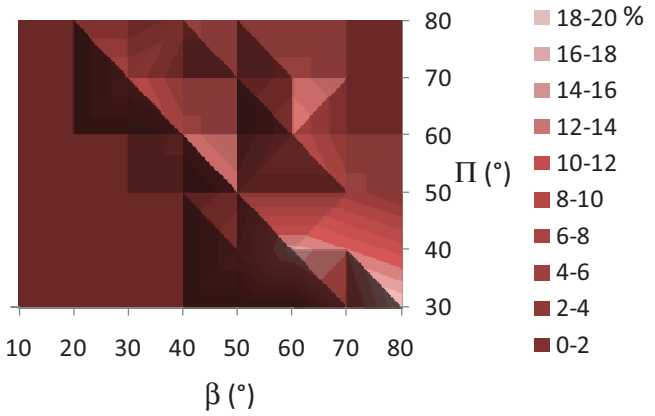

FIG. IV.28 - Combination of angles β and Π of slip systems, in grains showing cracks, corresponding to maximal Schmid factors but not turned into cracks.

IV.4.3. Crack initiation time - kinematical measurements

It is not possible to determine in the optical images taken during the test if cracks have already appeared or not. For that reason, in order to determine the number of cycles to crack initiation, displacement field calculations were performed at the grain scale. The final aim of this study is the analysis of the damage in low cycle fatigue. As this damage occurs on the surface, it was not possible to mark the surface, because that would have favored an early damage, or to paint it, as it would prevent to link kinematic fields to grain or phase shape or to slip systems activated. In that context, grid techniques were not considered (e.g. [Schroeter 03] [Moulart 09] [Badulescu 11]) as they need marks or painting on the surface and a solution by digital image correlation (DIC) was chosen [Besnard 06] [Hild 06] [Efstathiou 10] [Saai 10]. These two techniques have both been used to provide displacement and strain fields at the grain scale [Moulart 09] [Saai 10] [Efstathiou 10] [Héripré 07] [Schroeter 03] [Raabe 03] [El Bartali 09].

For that reason, in order to determine the number of cycles to crack initiation, displacement field calculations were performed by a digital image correlation technique, using software CorreliQ4 developed by Hild [Hild 02] [Hild 06]. The principle of this technique consists in comparing two

images of the same specimen surface area taken at two different times. The first image (called reference image) is subdivided into several elementary zones (l x l pixels), which form a mesh (FIG. IV.29). The position of each elementary zone is then searched in the second image (deformed image) and a correlation method is used to match an elementary zone in the initial image to the same elementary zone of the second image [Besnard 06].

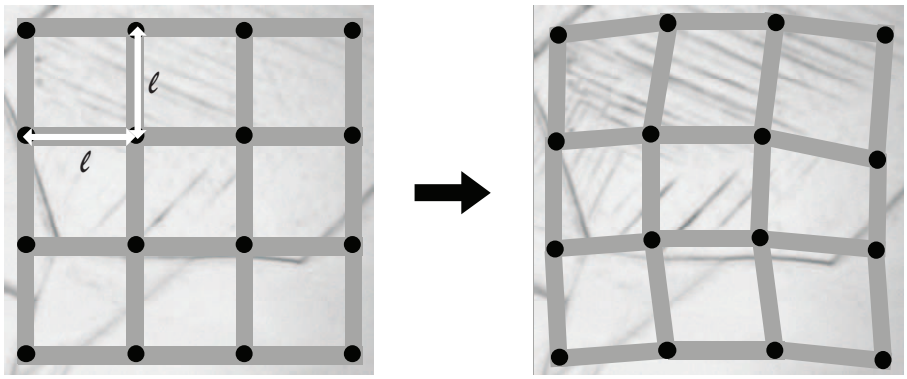

FIG. IV.29 - Meshing for the digital image correlation technique, reference image (left), deformed image (right), l is the elementary zone size.

The random surface texture necessary for the image correlation was obtained by a slightly electrochemical etching of the specimen. Performances of the displacement and strain field calculations in terms of resolution and accuracy were evaluated on images obtained during this test. The mesh size was optimized in order to limit uncertainties when keeping a space resolution compatible with intragranular strain heterogeneities and the grain size.

FIG. IV.30 shows the variation of uncertainty as a function of the imposed displacement. This uncertainty is determined by evaluating the standard error on all prescribed displacements. The results show that the standard uncertainty decreases when the correlation parameter (l, mesh size) increases. It reaches a maximum when the prescribed displacement is 0.5 pixel but remains below 0.09 pixel. If we trace in a logarithmic graph the average uncertainty on all prescribed displacements as a function of the mesh size (FIG. IV.31), it shows a linear trend. The relation between the average displacement uncertainty, σ_u, and the mesh size, l, is then of the type

$$\sigma_u = A^{\alpha+l} l^{-\alpha} \qquad \text{(IV-16)}$$

where A is a constant and α is the slope of the trend line. Here, A and α are equal to 0.7787 pixel and 1.309, respectively. The value of α shows that the uncertainty is sensible to the mesh size, l. The value obtained for α is a criterion of the quality of surface texture. In the literature, parameter α is generally around 1. The value obtained here can be compared to that obtained by El Bartali on a duplex stainless steel at the grain scale using natural surface texture, in that case, α was only 0.16 [El

Bartali 09]. Images obtained in this study are thus of sufficient quality to perform digital image correlation, although the texture does not appear on the images.

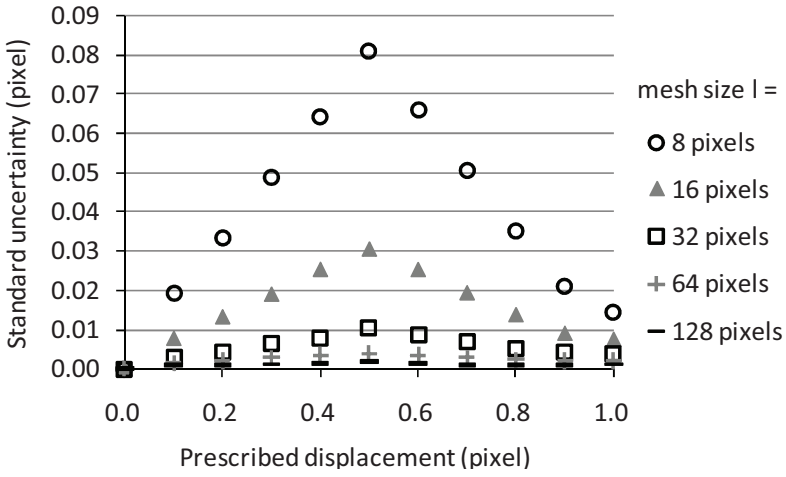

FIG. IV.30 - Variation of standard displacement uncertainty on function of the prescribed displacement (l, mesh size).

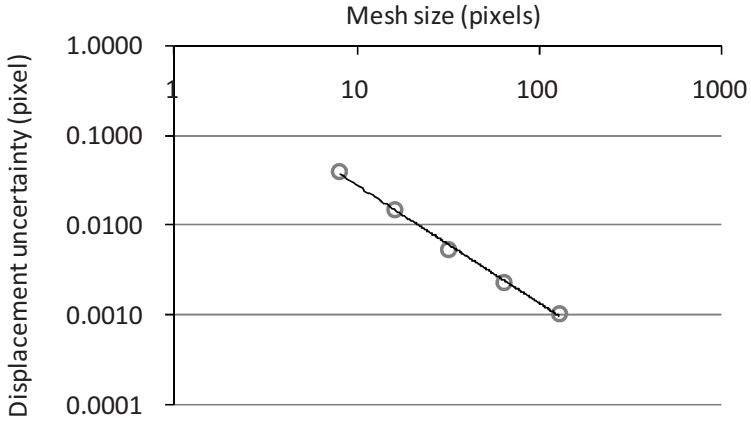

FIG. IV.31 - Displacement uncertainty as a function of mesh size.

Once the displacement uncertainty is known, the strain uncertainty can be approximated according to the relation [Surrel 04]

$$\sigma_\varepsilon \approx \frac{\sqrt{2}\sigma_u}{\Delta x} \qquad \text{(IV-17)}$$

where Δx is the spatial resolution, that worth 2l [Bergonnier 05].

For this study, an elementary zone of 32 x 32 pixels has been chosen, which represents about 4.4 x 4.4 μm^2. This size is a good compromise between enough measurement points and a low displacement uncertainty. With this mesh size, the displacement uncertainty was evaluated to 0.0054 pixel and the corresponding strain uncertainty is 1.2×10^{-4}.

FIG. IV.32 shows the optical images taken before the fatigue test, the initiation sites of two PSB cracks A and B are visible. Optical images were taken regularly during the fatigue test at $\varepsilon = 0$. FIG. IV.33 and FIG. IV.34 present the displacement and strain maps measured in the zones showing cracks A and B at various times of the fatigue test.

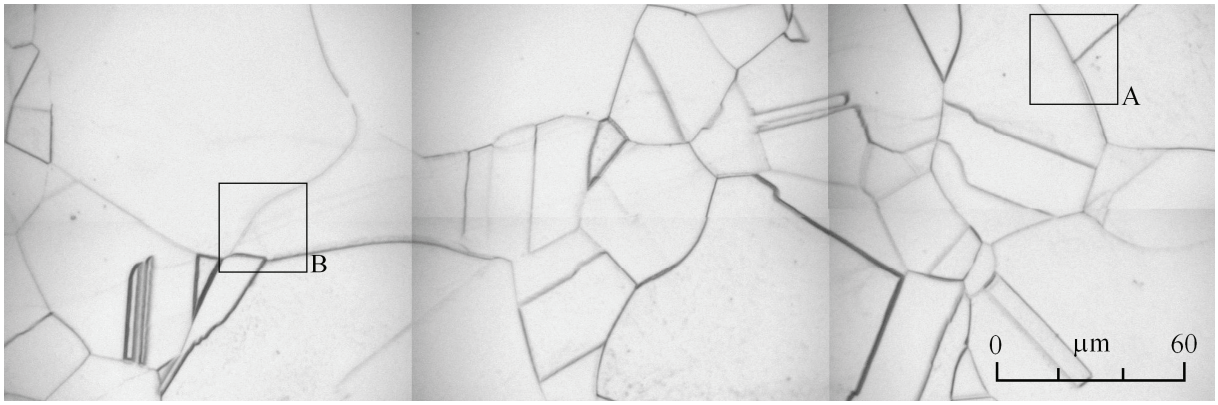

FIG. IV.32 - Optical images taken before the test, the initiation sites of PSB cracks A and B are visible.

FIG. IV.33 shows displacement and strain fields calculated between images taken at the beginning (a, b), at the middle (c), and at the end (d, e) of the fatigue test in the zone around crack A. Displacement and strain fields obtained in similar conditions in the zone around crack B can be seen in FIG. IV.34. It can be seen that before 500/600 cycles, as shown in FIG. IV.33a and b and in FIG. IV.34a and b, the displacement was quasi-homogeneous in each grain, and the strain localized in grain boundaries. Between 600 and 1400 cycles, as can be seen in FIG. IV.33c, the strain fields were relatively homogeneous. The strain level was relatively low compared to those in FIG. IV.34b and c. After 1400 cycles, as shown in FIG. IV.33d and e, strong displacement heterogeneities and strain localization can be seen. The site showing a strong displacement gradient and a strain localization marked by black arrows in FIG. IV.33d and e corresponds to the initiation site of crack A. Observing the optical images taken at all interruptions (ref FIG. IV.36) and analyzing the displacement heterogeneities, it can be concluded that crack A initiated between cycles 1400 and 1600. FIG. IV.35 shows the displacement field under vector form obtained in the zone around crack A. The calculation was done using the images taken respectively at cycles 1400 and 1600. It can be seen that the displacement vectors at the two sides of crack A are both vertical to the crack direction, however, they have opposite directions: the vectors at the upper right of crack A move towards the upper right, whereas the vectors at the lower left of crack A move to the lower left. It can be stated that between 1400 and 1600 cycles, the displacements in opposite directions at the two sides of crack A opened the crack. Concerning crack B, no similar conclusion can be drawn, as the calculation of displacement field did not converge with images taken after 1400 cycles (ref FIG. IV.37).

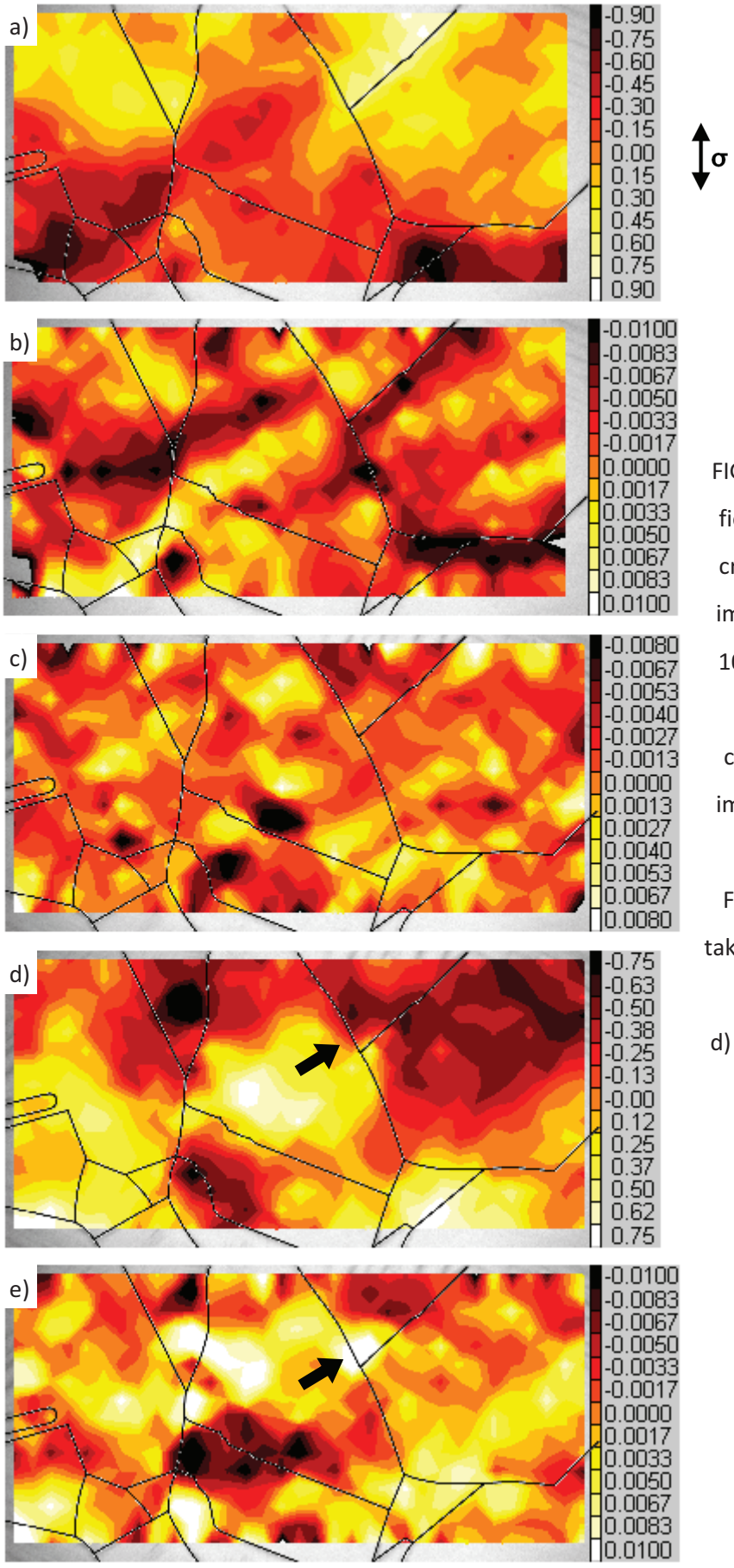

FIG. IV.33 - Displacement and strain fields obtained in the zone around crack A. Fields calculated between images taken respectively at cycles 100 and 200 a) displacement field, b) strain field.

c) Strain field calculated between images taken respectively at cycles 1200 and 1300.

Fields calculated between images taken respectively at cycles 1400 and 1600

d) displacement field, e) strain field.

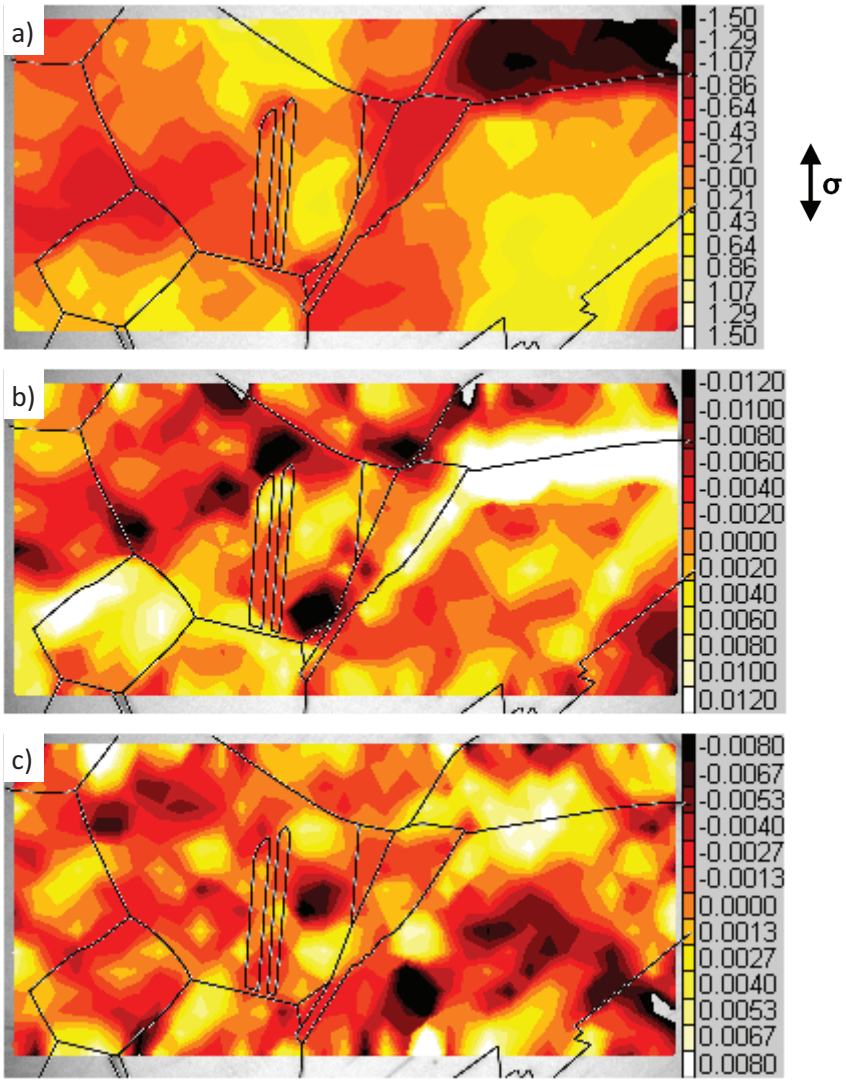

FIG. IV.34 - Displacement and strain fields obtained in the zone around crack B. Fields calculated between images taken respectively at cycles 200 and 300 a) displacement field, b) strain field. Strain field calculated between images taken respectively at cycles 1100 and 1200 c).

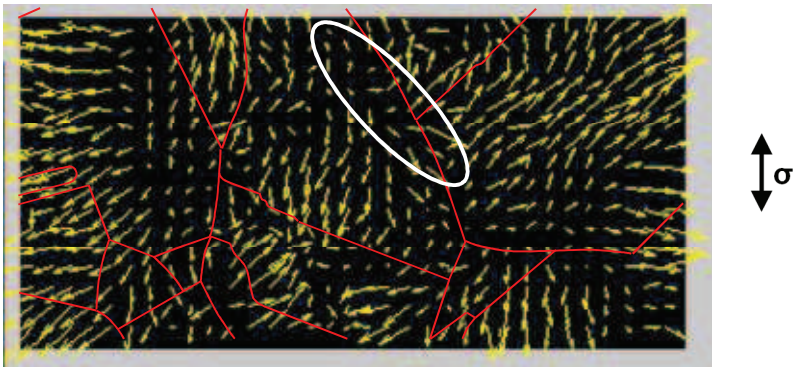

FIG. IV.35 - Displacement field obtained in the zone around crack A. Field calculated between images taken respectively at cycles 1400 and 1600.

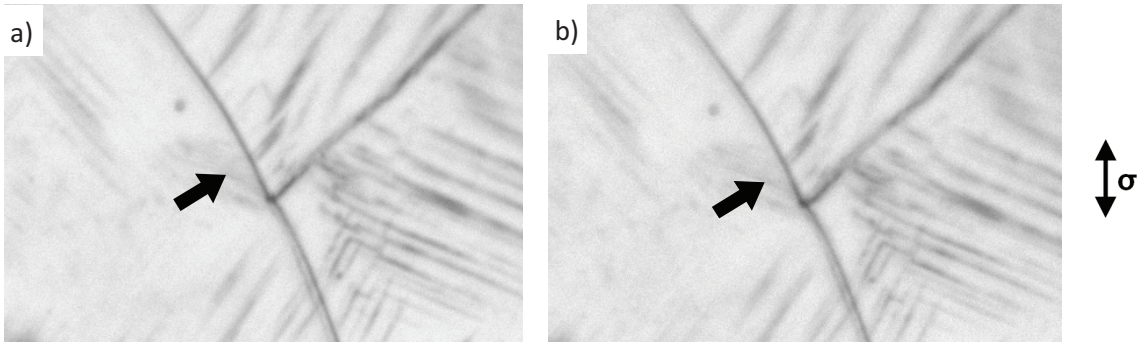

FIG. IV.36 - Images of zone around crack A taken at cycles 1400 a) and 1600 b).

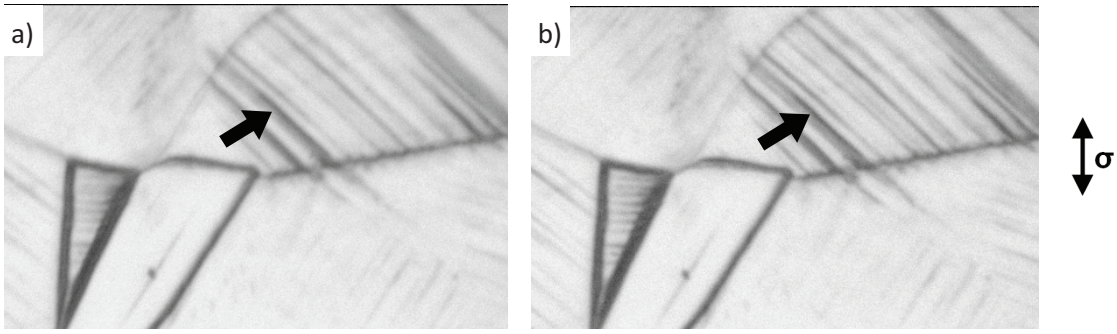

FIG. IV.37 - Images of zone around crack B taken at cycles 1400 a) and 1600 b).

IV.5. CONCLUSION

In this chapter, a tension-compression fatigue test was carried out; the surface of the specimen was observed during the test with an in situ microscope and after the test by SEM. Crystallographic orientations of the grains were obtained by EBSD after the mechanical test. It can be seen that the plastic activity appears very early during cycling, as over 75 % of the slip markings appear before 500 cycles. In crack initiation, the first various crack initiation sites were studied. 94 % of cracks initiated in slip bands or in grain boundaries. Crack orientations were measured and analyzed; and slip systems associated to cracks have been identified by comparing the measured crack orientations to the orientations of all potential slip systems. It was shown that about 2/3 of cracks make an angle with the loading axis in the range [50, 80°] and that about 2/3 cracks initiate in slips systems with the highest Schmid Factor. It was also found that if a slip system with the maximal Schmid factor in a grain has an orientation of about 45° with respect to the load axis, which is the case of grain A, there is a big chance that other slip systems will be activated. At last, digital image correlation was successfully used in the identification of the number of cycles to crack initiation.

V. SURFACE MICROPLASTICITY AND CRACK INITIATION MODELING

V.1. INTRODUCTION

Grains at the surface are less constrained than grains in the bulk, which makes possible larger strains in these grains than in grains in the bulk having the same orientation. These larger strains favor crack initiation. The objective of this chapter is to establish criterion of crack initiation. This objective requires two steps. First of all, it is necessary to determine stresses and strains in grains located at the surface. After presenting the problem of stress localization in a surface inclusion, a specific localization law for surface grains was thus studied, as the self-consistent model studied in chapter III is not still valid for surface grains. Secondly, some indicators extracted from fatigue life models and crack initiation models of the literature are evaluated and compared to the experimental results obtained in the previous chapter.

V.2. LOCALIZATION LAW FOR SURFACE GRAINS

V.2.1. NECESSITY OF A SPECIFIC LOCALIZATION LAW FOR SURFACE GRAINS

Not only in the case of technically rough surfaces, but also for finely polished specimens, crack initiation is predominantly found at the surface [Pokluda 94] [Suresh 98], excepted in case of large defaults (precipitates, pores) or under very high cycle fatigue [Stanzl-Tschegg 07] [Krupp 07]. Grains at the surface are in fact in plane-stress condition, which makes the development of microplasticity easier than in the bulk. Micro-cracks can then easily initiate at the surface. Considering the elements presented above, a localization law specific to surface grains is needed to correctly reflect the mechanical behavior of grains at the surface.

V.2.2. LOCALIZATION AT THE SURFACE

➢ LOCALIZATION LAWS

As presented in chapter III, several localization laws were proposed by Eshelby [Eshelby 57], Kröner [Kroner 61], Berveiller and Zaoui [Berveiller 79], Cailletaud and Pilvin [Cailletaud 92] and others to calculate the stresses in an inclusion surrounded by an elastic or elasto-plastic infinite matrix. As these laws are not adapted to grains located at a free surface, some researchers have studied the

mechanical behavior of an inclusion at the surface of an elastic semi-infinite matrix (FIG. V.1a). Lee and Hsu calculated the stresses in a parallelepiped inclusion located at the free surface and submitted to an isotropic thermal dilatation [Lee 89]. Cox has accomplished the calculations on a semi-ellipsoidal inclusion under different free strains imposed [Cox 89]. He used the functions of Boussinesq and Cerruti in order to modify the method proposed by Eshelby and to satisfy the condition of free surface. Deperrois and Dang Van studied the same problems but paid special attention to the plastic strains in slip systems of type A and B [Deperrois 90] [Deperrois 91], see FIG. V.1b and c.

- INFLUENCE OF ORIENTATION, DEPTH AND THE DISCONTINUITY AND HETEROGENEITY AT THE SURFACE

Influence of the depth. The surface effect is evanescent with the depth once the distance from the center of the spherical grain to the free surface is higher than the diameter of the grain [Deperrois 91]. Other research concerning spherical inclusions concluded that the influence of depth existed in the order of the grain diameter [Lee 92] [Jasiuk 97]. However, this quantitative result should be nuanced. According to Masumura and Chou [Masumura 82], the form ratio for an ellipsoid is an important parameter: for the inclusions prolonged in the direction parallel to the surface, the influence of surface effect extends over several inclusion diameters. Chiu presented that for the cubic inclusions, a surface effect until 3 diameters (according to the type of free deformation) should be considered [Chiu 78]. At last, with an elasto-plastic matrix, Pilvin highlighted a surface effect of 3 to 4 diameters of grain (of spherical form) [Pilvin 97]. In summary, in any loading and with any grain form, the impact depth is at most 4 diameters of grain.

Influence of the interface. Concerning the stress fields at the surface, it should be noted that a discontinuity may appear along the interface grain-matrix. This discontinuity was highlighted by Bui and Taheri who called it singularity Epine [Bui 89]. Assuming the isotropy of the material, the authors investigated the stress singularity near the crossing point between the free surface of the body and a surface of discontinuity in thermal and plastic strains. A very localized singularity of the stress field was found.

Kouris and Mura worked on the problem of the heterogeneity at the surface [Kouris 89]. An elastic hemispherical inclusion at the free surface of an elastic semi-infinite body is considered. The inclusion and the matrix have different isotropic elastic constants and the loading conditions are either equibiaxial tension at infinity, or uniform equibiaxial eigenstrains in the inclusion. The interface between the inclusion and the matrix assumes perfect bonding, sliding or intermediate

situations between them. They calculated the stress field induced by a free deformation and used Airy functions to write the displacement, which was decomposed into series according to Legendre polynomials. The coefficients were determined by using the limit conditions at infinity, at the free surface and at the interface inclusion-matrix. They showed that the heterogeneity in stresses and strains is governed by the ratio in shear moduli between matrix and inclusion and by the type of interface.

Influence of the orientation. The orientation of the activated slip system is an important parameter in the study of the surface effect. As the plastic behavior of the grain is based on simple gliding, grains most favorably oriented for the gliding have the highest Schmid factor. However, the Schmid factor is not sufficient to predict the risk of crack initiation. It is necessary to consider the possibility to create intrusions-extrusions at the surface on a given slip system. Among slip systems good oriented to simple gliding, two slip systems have a particular orientation toward the surface: systems A and B [Miller 73]. In both cases, slip plans make an angle of 45° to the direction of loading, but the slip direction changes. For system A, the slip direction is parallel to the free surface, and no intrusion-extrusion is created during the gliding (FIG. V.1 b). On the contrary, for system B, the slip direction makes an angle of 45° to the free surface, and the gliding along this slip system will create steps at the free surface (FIG. V.1 c), where micro cracks can initiate. In a semi-spherical grain at the surface, a plastic slip of type A introduces stresses very close to those obtained in a spherical grain in the bulk [Cox 89]. However, for a surface grain of type B, the solution is different with that obtained in the bulk [Deperrois 90]. Using a plasticity criterion, Deperrois deducted an increase of plastic slip in the grains having a slip system of type B.

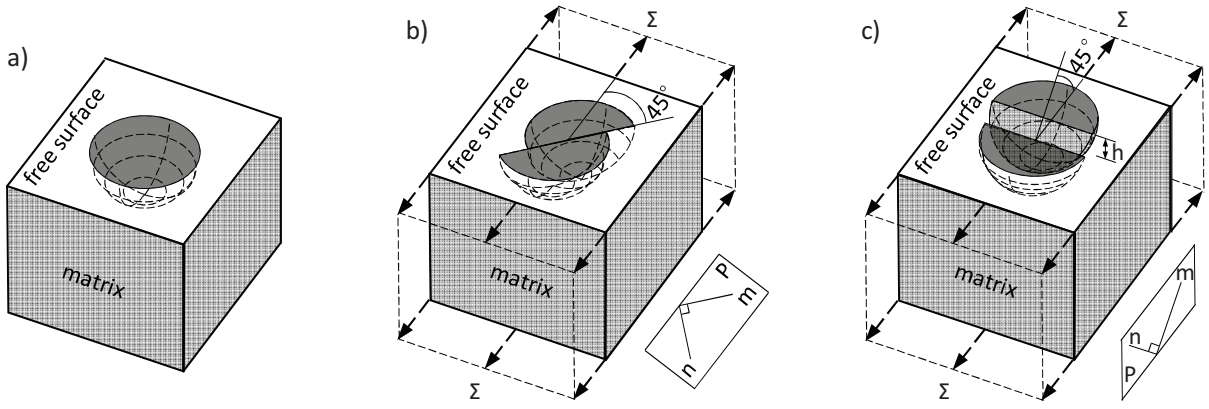

FIG. V.1 - a) Grain at the surface; b) System A; c) System B
(m, slip direction; n, normal of slip plan; h, step height).

Elasto-plastic behavior. At last, Pilvin studied the problem of surface grains in an elasto-plastic matrix for monotonic loadings above the yield stress [Pilvin 97]. He gave an elastoplastic behavior to a spherical grain located at different depths of a semi-infinite elasto-plastic matrix. The constitutive laws of the matrix were of macroscopic type. Finite element calculations were done for a finite mass containing a small inclusion. Strain amplitudes of 0.1, 0.3% and 0.5% were applied. The author illustrated a significant heterogeneity of the plastic slip at the surface and a stress concentration in the grain. The effect disappears with a depth of 3 or 4 grain sizes.

V.2.3. Formulation of a localization law for BCC materials

A localization law was proposed by Sauzay for surface grains considering a crystalline plastic behavior of an inclusion at the surface of a semi-inifinite body [Sauzay 00a]. He used and compared two methods: an analytical one and a finite element one. The analytical method is based on thermoelasticity and supposes that the plastic strain is uniform in the surface grain [Sauzay 00b] [Sauzay 99a, b]. The finite element method supposes that the matrix is elastoplastic (no longer elastic as in the analytical method) but have no hypothesis on plastic deformation uniformity [Sauzay 00b, c]. These two methods consider especially the BCC crystals at low temperature. Therefore the applicability of these methods to other crystal structures, especially FCC crystals, remains to be verified.

Considering that a grain in the bulk has the same stiffness tensor C as the elastic matrix in which the grain is embedded, when a uniform plastic strain ε^{p} is applied to the grain, the corresponding stress will be linear to ε^{p}. In an idealized ellipsoidal grain, the stress σ and total strain ε are uniform and given by [Eshelby 57]:

$$\sigma = \Sigma - \mathrm{C} : (\mathrm{I} - \mathrm{S}) : \varepsilon^{\mathrm{p}} \tag{V-1}$$

$$\varepsilon = \mathrm{E} + \mathrm{S} : \varepsilon^{\mathrm{p}} \tag{V-2}$$

where Σ and E are the macroscopic stress and strain that are applied additionally. The fourth-order Eshelby tensor S depends only on the Poisson's ratio ν and on the aspect ratios of the ellipsoidal grain, and I denotes the unit fourth-order tensor. If the grain is spherical, EQ. V-1 simplifies into

$$\sigma = \Sigma - 2\mu\,(1 - \beta)\,\varepsilon^{\mathrm{p}} \tag{V-3}$$

where μ is the shear modulus,

$$\mu = \frac{\mathrm{E}}{2(1+\nu)} \tag{V-4}$$

and

$$\beta = \frac{2(4-5\nu)}{15(1-\nu)} \tag{V-5}$$

If a surface grain (FIG. V.2) is subjected to a given uniform ε^p, the induced stress and strain are no more uniform, but they are still linear to ε^p [Sauzay 99a] [Sauzay 00c]:

$$\sigma(x) = \Sigma - 2\mu\,(1-\beta)\,M(x) : \varepsilon^p \tag{V-6}$$

$$\varepsilon(x) = E + S_{surf}(x) : \varepsilon^p \tag{V-7}$$

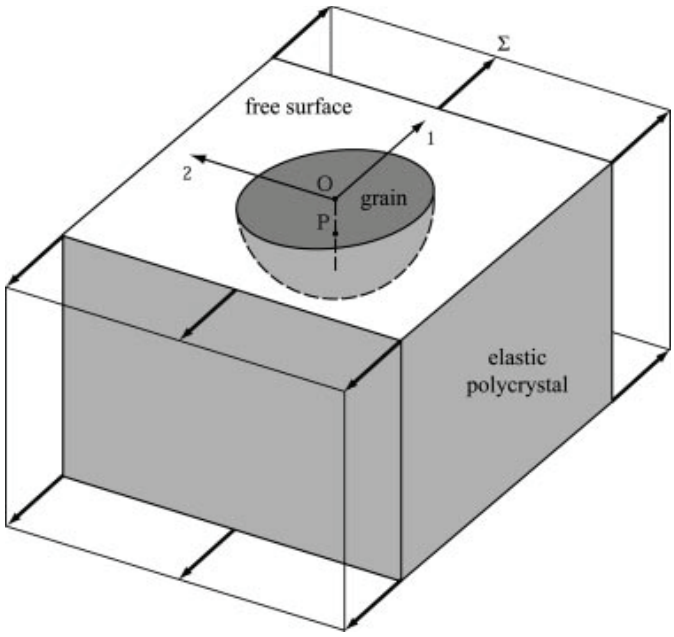

FIG. V.2 - A surface grain embedded in a semi-infinite matrix. Point O is at the free surface and point P is at half-depth of the surface.

The dimensionless fourth-order tensors $M(x)$ and $S_{surf}(x)$ depend on point x in the grain, on Poisson's ratio ν and on the grain shape.

A prescribed uniform deviatoric thermal strain was applied over a hemispherical volume of an approximately semi-infinite elastic medium (FIG. V.3). The mechanical behavior of the matrix was considered elastic (E = 200 GPa, ν = 0.3). The inclusion consists of a BCC crystal having a slip system of {110}<111> type oriented for single slip.

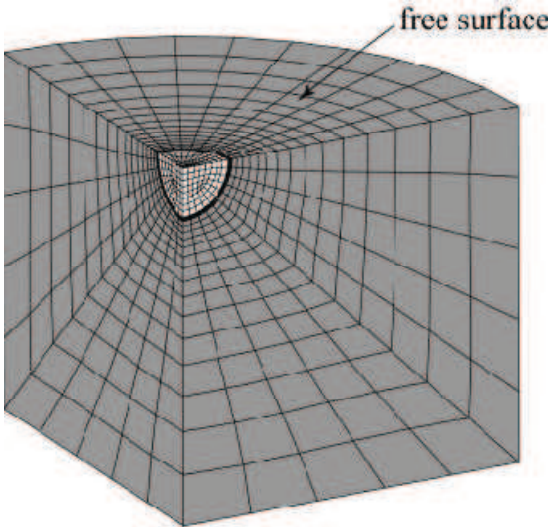

FIG. V.3 - ABAQUS mesh of the inclusion embedded in a semi-matrix [Sauzay 00a].

The finite element method shows the following results. First, the plastic slip and the stresses are heterogeneous in the grain. The strain is maximal at mid-depth of the surface grain but the displacements are maximal on the free surface. The plastic deformation seems maximal in the slip bands at 45º. Compared with the plastic strain amplitude in inner grains, the plastic strain amplitude at the most stressed point of the surface grain (point P in FIG. V.2) is multiplied by about 1.55, and the average value ε^p of all points in the surface grain is multiplied by 1.35.

As the tensor $M(x)$ is built in respecting the symmetry of the tensor of Eshelby S:

$$M_{ijkl} = M_{jikl} = M_{jilk} = M_{ijlk} \tag{V-8}$$

EQ. V-6 can be simplified as:

$$\sigma_{11} = \Sigma_{11} - 2\mu\,(1-\beta)\,M_{1111}\,\varepsilon^p_{11} - 2\mu\,(1-\beta)\,M_{1122}\,\varepsilon^p_{22}$$

$$\sigma_{22} = \Sigma_{22} - 2\mu\,(1-\beta)\,M_{1122}\,\varepsilon^p_{11} - 2\mu\,(1-\beta)\,M_{1111}\,\varepsilon^p_{22}$$

$$\sigma_{12} = \Sigma_{12} - 2\mu\,(1-\beta)\,M_{1212}\,2\,\varepsilon^p_{12}$$

$$\sigma_{13} = -2\mu\,(1-\beta)\,M_{1313}\,2\,\varepsilon^p_{13}$$

$$\sigma_{23} = -2\mu\,(1-\beta)M_{1313}\,2\,\varepsilon^p_{13}$$

$$\sigma_{33} = -2\mu\,(1-\beta)\,M_{3311}\left(\varepsilon^p_{11} + \varepsilon^p_{22}\right) \tag{V-9}$$

where M_{ijkl} are components of the M tensor. Their values are listed in TAB. V.1. The components of the M_{ij33} are zero because ε^p_{33} $(= -\varepsilon^p_{11} - \varepsilon^p_{22})$ was eliminated. Because M depends on position of point x, only its mean value over the hemispherical grain is given in TAB. V.1.

Component	M_{1111}	M_{1122}	M_{1212}	M_{1313}	M_{3311}
Mean value	1.24	0.24	0.5	0.26	-0.24

TAB. V.1 - Normalized stress localization factors giving the mean stress value over the grain.

V.2.4. FORMULATION OF THE LOCALIZATION LAW USED IN THIS STUDY

In order to determine the localization law of an inclusion at the surface of a semi-infinite matrix, a FE calculation was conducted in the same conditions, representing a semi-spherical inclusion embedded in a matrix having the equivalent homogeneous behavior (EHM). A three-dimensional mesh with eight-node hexahedric elements was carefully designed and checked (FIG. V.4). Fine discretization was done in the grain and the interface grain-matrix. In order to make the assumption of a semi-infinite matrix, the dimensions of the matrix are 25 times those of the grain. The mechanical behavior of the matrix is considered as isotropic elastoplastic, whereas the grain has a crystalline elastoplastic behavior. As the grain may have any orientation, no symmetry of the problem can be assumed, and the whole semi-spherical grain and semi-infinite matrix were meshed. The mesh owns 12440 elements in the matrix and 1100 elements in the grain.

A perfect tie was imposed at the interface between grain and matrix and boundary conditions were imposed to the matrix (FIG. V.5). On Surf1, displacement $u_3 = 0$; on Line1, displacement $u_2 = 0$; on Line2, displacement $u_1 = 0$. A triangular cyclic displacement u_3 was imposed on Surf2 in order to simulate a total strain imposed in the matrix of 0.5 %.

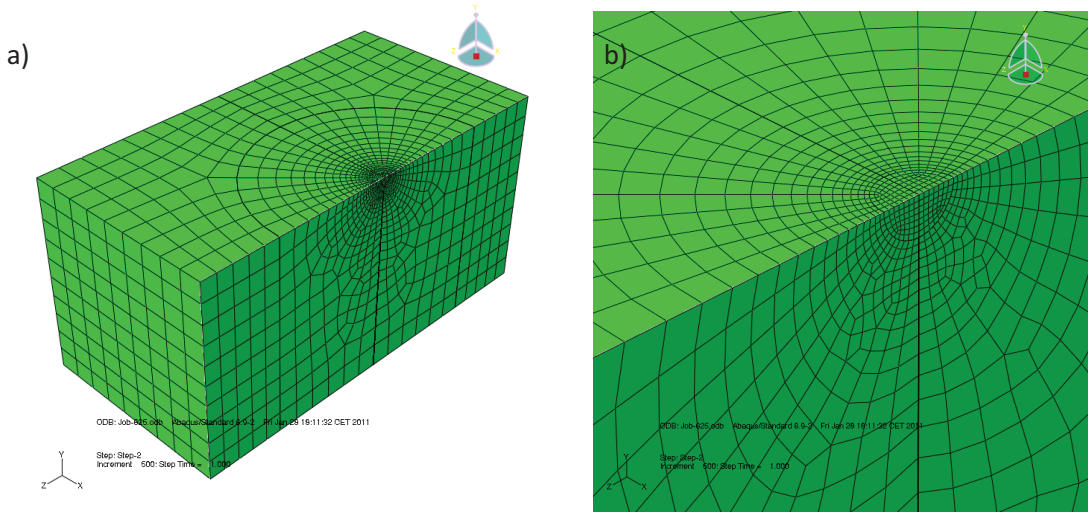

FIG. V.4 - ABAQUS mesh of the inclusion at the surface of a matrix, a) half of the total mesh, b) detail of the inclusion mesh.

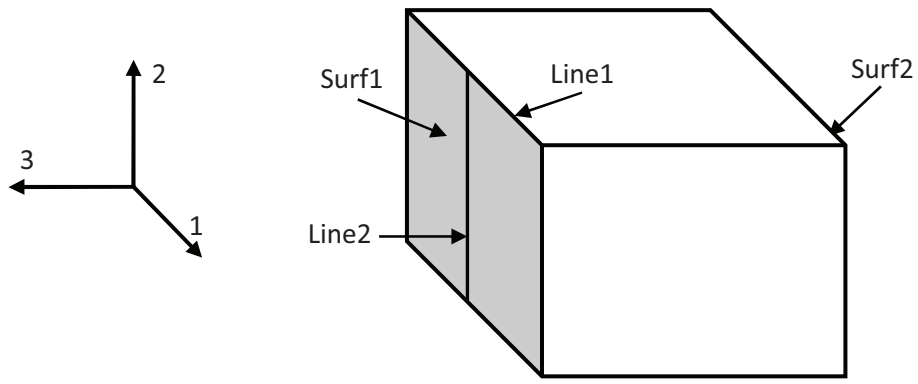

FIG. V.5 - Boundary conditions imposed to the matrix.

The grain has a crystalline elasto-plastic behavior. As the influence of anisotropic elasticity is limited in plastic fatigue [Osterstock 08] and to remain consistent with the self-consistent model adopted in the bulk, crystalline elasticity was considered isotropic. The elastic constants are defined as follows:

$$C_{11} = \frac{E(1-\upsilon)}{(1+\upsilon)(1-2\upsilon)} \tag{V-10}$$

$$C_{12} = \frac{E\upsilon}{(1+\upsilon)(1-2\upsilon)} \tag{V-11}$$

$$C_{44} = \frac{E}{(1+\upsilon)} \tag{V-12}$$

The crystalline plastic behavior of the grain was defined in chapter III, the parameters are given in TAB. III.4.

The mechanical behavior of the matrix was considered elasto-plastic. The constitutive law uses a yield function given below:

$$f(\sigma - X) = \sqrt{\frac{3}{2}(s - X):(s - X)} - k \tag{V-13}$$

where X is a kinematic hardening component, s is the deviatoric part of σ and k is the initial yield stress.

X is defined as the sum of two different kinematic hardenings, as

$$X = X_1 + X_2 \tag{V-14}$$

The evolution of each kinematic hardening component is defined by:

$$\dot{X}_i = \frac{2}{3} C_i \dot{\varepsilon}^p - \gamma_i X_i \dot{p} \qquad \text{(V-15)}$$

where p is the cumulative equivalent plastic strain.

This model needs 5 parameters: E, ν, k, C_1, γ_1, C_2 and γ_2. The elastic parameters are identical to that of the grain. The plastic parameters were identified on the first cycle of the cyclic test with a strain amplitude of 0.5 % and their values are given in TAB. V.2.

Parameter	k	C_1	γ_1	C_2	γ_2
Value	86 MPa	616200 MPa	7640	140000MPa	955

TAB. V.2 - Parameters of the plastic behavior of the matrix.

An ABAQUS user's material routine developed in MSSMat was used to describe the crystalline plastic behavior [Evrard 08] [Erieau 04]. The simulations have been carried out for 11 random orientations of the grain. The finite element simulations showed that stress and strain fields are heterogeneous in the grain (FIG. V.6 and FIG. V.7). The position of the maximal strain depends on the orientation of the grain. Shear strains are of the same order of magnitude as tension strain ε_{33} imposed on the matrix (FIG. V.7). In the most loaded point, the von Mises equivalent total strain reaches 1.65 times the tension strain imposed to the matrix after a monotonous loading (FIG. V.7c).

a) b)

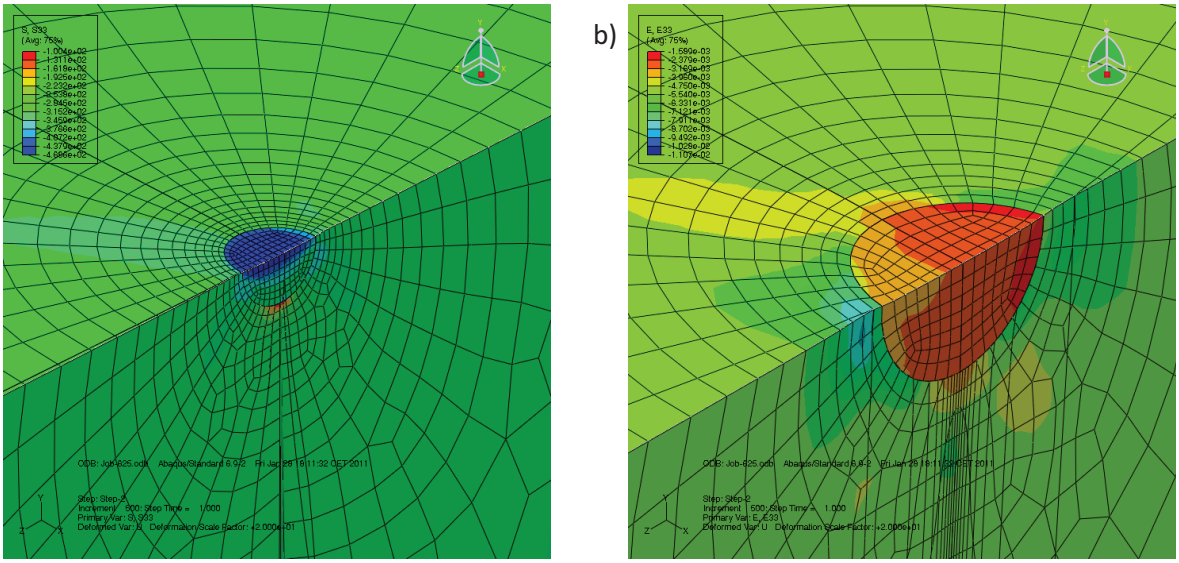

FIG. V.6 - Heterogeneity of stress and strain fields in and around the inclusion under a macroscopic strain imposed ε_{33} = -0.5 %, a) σ_{33}, b) ε_{33}.

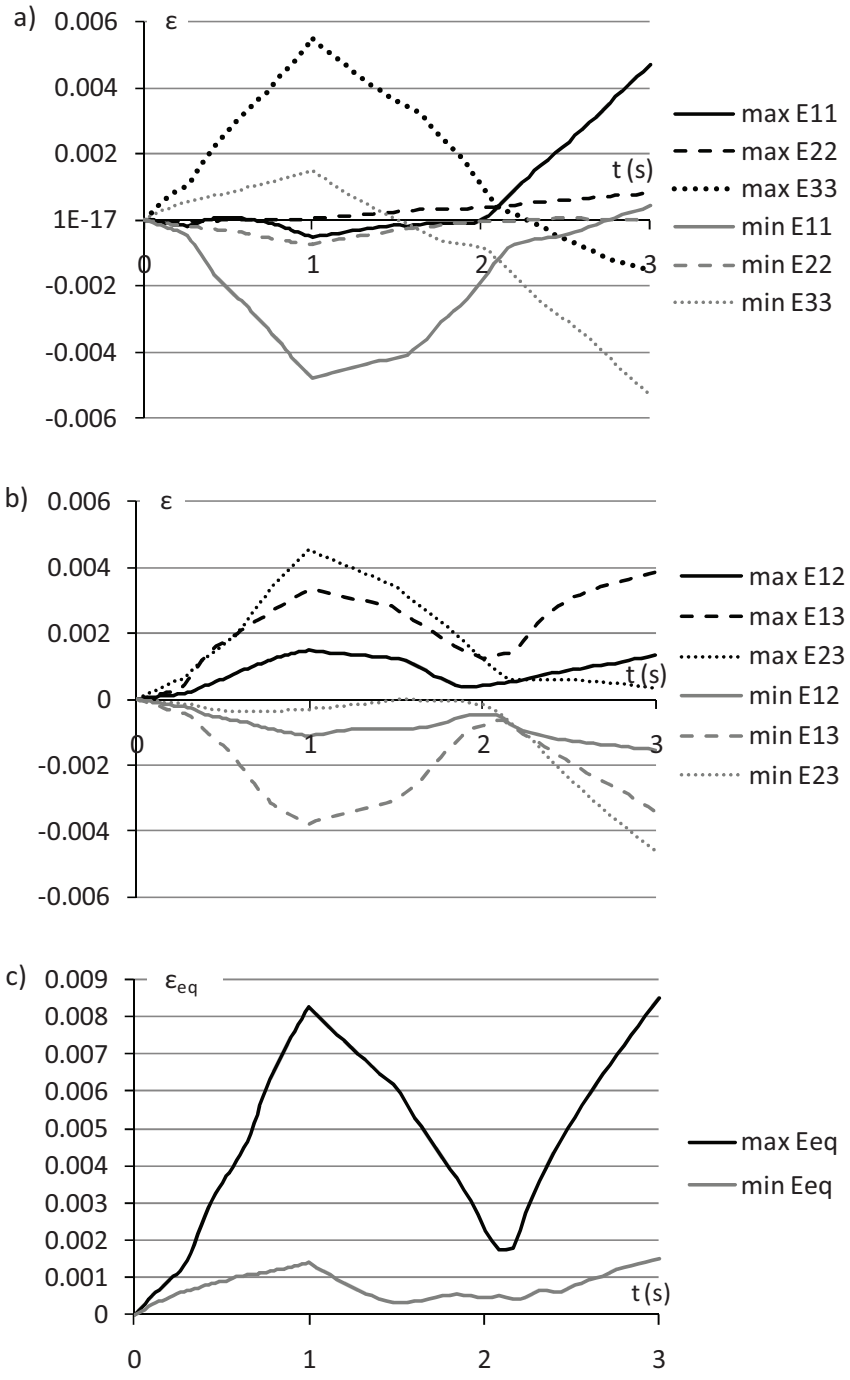

FIG. V.7 - Example of the evolutions of strains in grain #21 during 1 cycle,
a) normal strains, b) shear strains, c) von Mises equivalent strain.

The average stress and strain tensors were calculated for all grain orientations. Two localization laws were tested and identified on the numerical results. Although it is valuable only for monotonic loadings, the localization law proposed by Sauzay was tested.

$$\sigma(x) = \Sigma - 2\mu\,(1-\beta)\,M(x) : \varepsilon^{p} \qquad \text{(V-16)}$$

As the parameters in TAB. V.1 are valid only for an elastic matrix, the components of fourth-order tensor M have to be identified. A cost function F was defined for each parameter set A by comparing the simulated results with the Finite Element ones with summations on all grains tested and on the time, as:

$$\mathrm{F(A)} = \sum_{\mathrm{gr}} \sum_{\mathrm{t}} (\mathrm{Z^{FE}(t)} - \mathrm{Z^{sim}(A,t)})^2 \qquad \text{(V-17)}$$

After identification, the maximal error in stresses during a monotonic tension up to 0.5 % was 57 MPa on component σ_{33}. The components of tensor M are given in TAB. V.3.

Component	$\mathrm{M_{1133}}$	$\mathrm{M_{1313}}$	$\mathrm{M_{2233}}$	$\mathrm{M_{2323}}$	$\mathrm{M_{3333}}$
Value	0.21	0.129	-0.237	0.043	0.308

TAB. V.3 - Components of fourth-order tensor M.

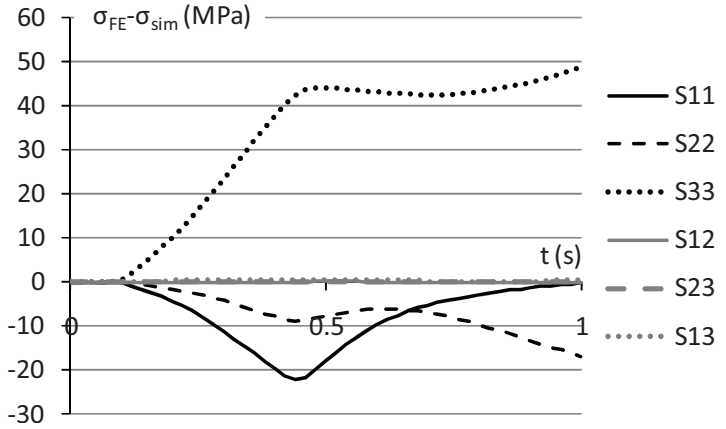

FIG. V.8 - Example of the evolutions of the prediction error of stresses in grain #15 during a monotonous loading.

However, this localization law is not valuable for non-monotonous loadings; a new localization law was defined, having the same form as the law proposed by Cailletaud and Pilvin for self-consistent modeling [Pilvin 92]

$$\underline{\sigma}^{\mathrm{g}} = \underline{\Sigma} + \mu\left(\underline{\mathrm{C}} - \underline{\gamma}^{\mathrm{g}}\right) \qquad \text{(V-18)}$$

where $\underline{\Sigma}$ is a plane stress defined by the following expression if axis 2 is normal to the free surface

$$\underline{\Sigma} = \begin{bmatrix} \Sigma_{11} & 0 & \Sigma_{13} \\ 0 & 0 & 0 \\ \Sigma_{13} & 0 & \Sigma_{33} \end{bmatrix} \tag{V-19}$$

$\underline{C}$ is the average of intergranular accommodation variables $\underline{\gamma}^g$ in all the grains.

$$\underline{C} = \sum_g^{N_g} f^g \underline{\gamma}^g \tag{V-20}$$

f^g is the volume fraction of each grain (1/11 during the identification process). Variable $\underline{\gamma}^g$ plays the role of a kinematic hardening. The same evolution was taken as the evolution of variable $\underline{\beta}^g$ used to describe the intergranular interaction in self-consistent modeling (see chapter III) [Pilvin 92]

$$\dot{\underline{\gamma}}^g = \dot{\underline{\varepsilon}}^{pg} - K\left(\underline{\gamma}^g - \kappa \underline{\varepsilon}^{pg}\right) \left\| \dot{\underline{\varepsilon}}^{pg} \right\| \tag{V-21}$$

Two parameters are introduced in this formulation: K and κ. These two parameters were identified using the average stress and strain tensors calculated in various grains with the Finite Element method presented above and minimizing the cost function defined in EQ. V-17. After identification, K = 1800 and κ = 0.059. The maximal error on the prediction of granular stress tensor during one cycle is still on component σ_{33} and reaches 47 MPa.

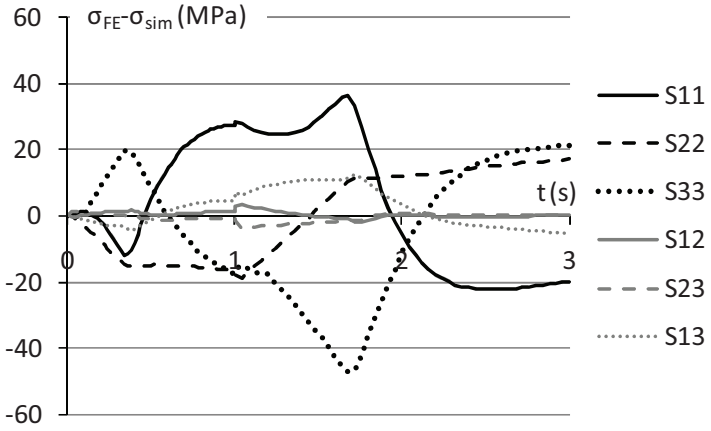

FIG. V.9 - Example of the evolutions of the prediction error of stresses in grain #29 during 1 cycle.

Once the granular stresses in surface grains are calculated through the localization law introduced above, shear stresses and strains in each slip system can be obtained using the crystal law introduced in chapter III for volume grains. These shear stresses and strains will then be used to study the number of cycles to crack initiation. Crack initiation models will be introduced in the next section.

V.3. DEFINING INDICATORS FROM FATIGUE LIFE AND CRACK INITIATION MODELS

V.3.1. INTRODUCTION

Big efforts have been done to more and more accurate fatigue life models able to predict the number of cycles of fatigue failure of a given structure. Most of them are addressed to predict the total fatigue life under cyclic loading but the variables on which they are built may give some indications also on the number of cycles to crack initiation although it was not their initial purpose. In this section, some fatigue life models will be presented and their predictions compared to experimental observations. Some crack initiation models have also been proposed in the literature. Two of them will be analyzed and compared to experimental data.

- FATIGUE LIFE CRITERIA

A high number of fatigue damage models have been addressed during the last 170 years. A full review of these models and approaches has been done by Brown and Miller [Brown 73], Krempl [Krempl 74], Garud [Garud 81a], Socie [Socie 93], Macha and Sonsino [Macha 99], and Carpinteri and Spagnoli [Carpinteri 01]. Fatigue criteria can be divided into three main groups below.

Strain-based criteria. The first criterion to be mentioned was proposed by Manson [Manson 53] and Coffin [Coffin 54]. It is based on the equivalent plastic strain range, and its accuracy was experimentally proved on numerous materials in low-cycle fatigue. Its simplicity has led to a wide used in various applications.

On the other side, numerous criteria for low-cycle fatigue make the assumption of a critical plane. The critical plane is generally the plane in which the normal or shear strain (or a combination of them) is maximal. Damage accumulation is then estimated by using mean and maximal values of normal and shear strains related to the critical plane. This type of criterion was first proposed by [Findley 56] and developed by [Brown 73] [Leese 81] [Kandil 82] [Fatemi 88] [Socie 93] [Zhang 03] etc.

Strain-based criteria. Stress based models are usually used in the high-cycle fatigue domain. The stress based approach can be divided into three main groups: stress invariant criteria, critical plane criteria and average stress criteria. The most used stress invariant criterion are due to Sines [Sines 55] and Crossland [Crossland 56]. In the critical plane criteria, it is assumed that the maximal loaded material plane through the point in question is decisive for fatigue, such criteria can be seen in [Findley 59] [Dang Van 89] [McDiarmid 90] etc. In the average stress criteria, it is suggested that the average stresses on all planes through a given point can be used as a measure of the effective stress

[Grubisic 76] [Liu 03]. Dang Van model was later improved by introducing an average stress quantity on the critical plane [Papadopoulos 95].

Energetic criteria. In order to overcome the drawbacks of the approach in strain or in stress, a unified approach in energy was proposed to predict low-cycle fatigue as well as high-cycle fatigue. This approach combines variables σ and ε and introduces the energy.

Global energy can be used as damage parameter, as seen in [Halford 66] [Mroz 67] [Garud 81b] [Golоś 87] [Golоś 88] [Ellyin 93a, b] [McDowell 92] [Jahed 06] among many others.

In a symmetric way like the criteria based on strain or stress, criteria defined from the energy density related to the critical plane were also proposed [Glinka 95] [Lagoda 01] [Varvani-Farahani 00]. An alternative formulation of energy (rather: stress-strain) condition associated with critical plane was presented in [Chu 93] [Glinka 95], etc.

- CRACK INITIATION CRITERIA

The fatigue life criteria presented above are used to predict the appearance of macrocracks, the dimension of which can be several millimeters. The crack initiation criteria which will be presented below intend to predict the initiation of a microcrack (several micrometers) in a grain of the material. These crack initiation criteria can be divided into three groups:

The first group includes the criteria based on the physical mechanisms of plastic deformation (PSB, dislocations, vacancies, etc.). An energetic model predicting crack initiation from slip bands was proposed by Tanaka and Mura based on the assumption that the micro-cracks are initiated by irreversible dislocation pile-ups in slip bands [Tanaka 81]. Chauvot *et al.* replaced the local plastic shear strain amplitude by macroscopic plastic strain amplitudes for engineering purposes [Chauvot 00]. Glodež *et al.* improved Tanaka and Mura model in three aspects: multiple slip bands in each grain, micro-crack coalescence by connection of existing micro-cracks along grain boundaries into a macro-crack, and segmented multiple-step micro-crack generation [Glodež 10].

Bhat and Fine considered the initial formation of a fatigue crack as a nucleation process due to random fluctuations of a metastable assembly of defect structures generated during cycling [Bhat 01]. By minimizing the Gibbs free energy change, the critical number of cycles required to nucleate fatigue cracks is estimated as a function of strain amplitude. Sangid *et al.* modeled the energy of a PSB structure and used its stability with respect to dislocation motion as a crack initiation criterion [Sangid 11]. Risbet *et al.* illustrated a recent measurement of plastic strain irreversibility obtained with atomic force microscopy (AFM), which can be used to discuss the opportunity to define fatigue

crack initiation in terms of a critical value of plastic strain irreversibility [Risbet 08]. A so-called local irreversible plastic strain accumulated in the band, $\gamma_{\mathrm{irr,loc.pl}}$, which was a function of critical height of the extrusion and grain size, was taken as the critical value to induce crack initiation. Manonukul *et al.* proposed a fatigue crack initiation criterion simply based on a critical accumulated slip, which is easy to identify with only one experimental test [Manonukul 04]. When this critical slip is achieved within the microstructure, crack initiation is assumed to occur.

The second group uses some originally macroscopic parameters in the microscopic scale. Continuum mechanics have been adopted in these criteria. Lim *et al.* presented a methodology of life prediction of fatigue crack initiation by modifying Neuber's rule and Glinka's equivalent strain energy density (ESED) method for incremental application [Lim 05]. The prediction of fatigue crack initiation life was carried out by adopting plastic strain energy density (PSED) as a fatigue parameter. Cheong defined the local energy dissipation in a grain and used it as an indicator of fatigue crack initiation [Cheong 07].

The third group of crack initiation criteria considers crack initiation as a procedure of crack propagation. These criteria use indicators originally used in crack propagation criteria. Provan *et al.* proposed an analytical model of stage-I fatigue crack initiation based on a plastic strain intensity factor, $\Delta \mathrm{K_p}$ [Provan 91]. This model simplified the stage-I crack initiation process as a straight line on a log-log plot of da/dN against $\Delta \mathrm{K_p}$, and the integration of the crack growth rate yields a fatigue crack initiation life. Lynn *et al.* developed a damage accumulation model based on the growth and closure mechanisms of microcracks, incorporating a parameter called the "net effective strain range $\Delta\varepsilon^*$" (strain range over which small intrinsic cracks at surface and sub-surface remain open), and used this model for crack initiation prediction [Lynn 02].

In the next sections, instead of testing directly the fatigue criteria presented above, the analysis of various indicators extracted from these fatigue damage models will be done using the characteristics of the grains showing cracks observed in chapter IV.

V.3.2. Analysis of crack initiation indicators

The fatigue criteria presented above are based on a limited number of indicators. Instead of testing all these criteria one by one, only the role these criteria play in crack initiation has been tested and compared to experimental data. For this, the values of some indicators calculated for an experimental distribution of grain orientations were analyzed.

The simulation requires two steps. First of all, the mechanical behavior of the austenitic stainless steel is simulated with the self-consistent model presented and identified in Chapter III. Secondly, the stress-strain relationship in some surface grains is simulated using the surface localization law identified above. This means that, at each time step, two localization laws are used, one for simulating the average behavior of the material representing the grains of the bulk and a second one for predicting stress in surface grains (FIG. V.10).

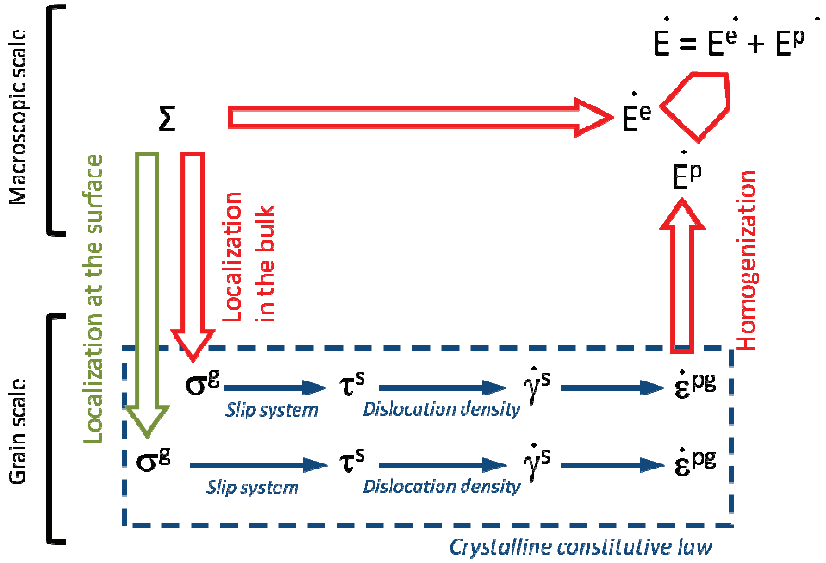

FIG. V.10 - Methodology of simulation of the mechanical relationships in the one hand, in grains of the bulk representing the homogeneous behavior of the material and, in the other hand, of grains at the surface.

From a given macroscopic stress Σ, stress tensor σ^g is calculated in each grain of the RVE (representing the bulk) using the bulk localization law (law in β^g). The rate of the plastic strain ε^{pg} in this grain is the evaluated through the crystalline constitutive law, which allows to determine the rate of the total macroscopic strain E, and then the macroscopic stress of the following time increment. From the same macroscopic stress, stress tensor in each surface grain is calculated using the surface localization law (law in γ^g). The rate of the plastic strain ε^{pg} in this surface grain is the evaluated through the crystalline constitutive law. The same parameters for the crystalline constitutive law are used in surface grains as in bulk grains.

Concerning surface grains, calculations were carried out with two types of grains: on the one hand, 12 orientations of grains where big cracks have been seen after the fatigue test presented in chapter IV and, in the other hand, 488 orientations of grains without any crack.

Indicator distributions were compared for these two groups of grains. In the next sections, the analysis will be carried out for 8 indicators. Some of these indicators are originally used at the

macroscopic scale, e.g. the macroscopic equivalent deformation amplitude $\Delta\varepsilon_{eq}$. In this study, the corresponding indicator at the grain scale is analyzed. There are also some indicators which are not used by any criteria at present. However, according to their physical senses, these indicators may play an important role in fatigue damage, e.g. the dislocation density ρ. So their results are also shown in this study, which may serve for the creation of potential fatigue damage criteria.

- EQUIVALENT STRAIN AMPLITUDE, $\left(\varepsilon_{eq}^{p}\right)_{gr,max}$

The equivalent plastic strain was used in the Coffin-Manson fatigue life criterion [Manson 53] [Coffin 54]. We adapted this criterion to the grain scale in writing the maximal value of the equivalent plastic strain in each surface grain during the fatigue cycling:

$$\left(\varepsilon_{eq}^{p}\right)_{gr,max} = \max_{t=t_0,t_1}\left(\sqrt{\frac{\left(\varepsilon_{11}^{p,gr}-\varepsilon_{22}^{p,gr}\right)^2+\left(\varepsilon_{22}^{p,gr}-\varepsilon_{33}^{p,gr}\right)^2+\left(\varepsilon_{33}^{p,gr}-\varepsilon_{11}^{p,gr}\right)^2+6\left[\left(\varepsilon_{12}^{p,gr}\right)^2+\left(\varepsilon_{23}^{p,gr}\right)^2+\left(\varepsilon_{31}^{p,gr}\right)^2\right]}{2}}\right) \quad \text{(V-22)}$$

where $\varepsilon_{11}^{p,gr}$, $\varepsilon_{22}^{p,gr}$, $\varepsilon_{33}^{p,gr}$, $\varepsilon_{12}^{p,gr}$, $\varepsilon_{23}^{p,gr}$, $\varepsilon_{31}^{p,gr}$ are the six components of the plastic strain tensor in a given surface grain, t_0, t_1 are the time corresponding to the beginning and the end of the fatigue cycling.

The distribution of $\left(\varepsilon_{eq}^{p}\right)_{gr,max}$ for the 12 surface grains showing sufficiently long cracks and the set of 488 surface grains without cracks is shown in FIG. V.11. For the grains without cracks, $\left(\varepsilon_{eq}^{p}\right)_{gr,max}$ has a distribution between 0.0059 and 0.0095. For the grains showing cracks, a narrow distribution can be seen: $\left(\varepsilon_{eq}^{p}\right)_{gr,max}$ varies between 0.0074 and 0.0095. In the high-value zone ($\left(\varepsilon_{eq}^{p}\right)_{gr,max}$ > 0.008), grains showing cracks occupy a proportion (83.3 %) much larger than that of the grains without cracks (49.8 %). This shows that more plastic deformation can be seen in cracked grains. $\left(\varepsilon_{eq}^{p}\right)_{gr,max}$ is a good indicator of fatigue damage.

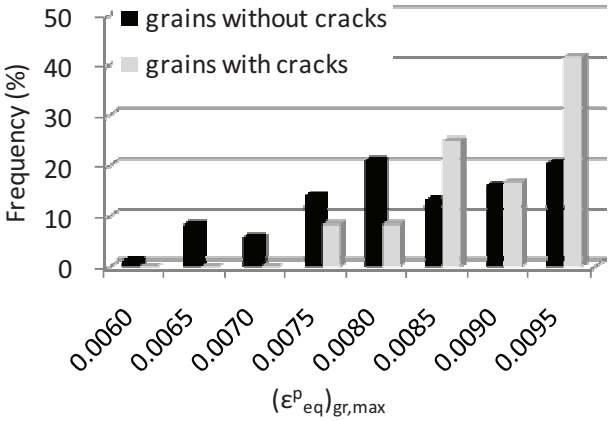

FIG. V.11 - Distributions of equivalent plastic strain amplitude $\left(\varepsilon_{eq}^{p}\right)_{gr,max}$ among 12 surface grains showing cracks and 488 surface grains without cracks. Distribution is obtained after a simulation of 192 cycles with $\Delta\varepsilon_t$ = 0.5 %.

➢ CUMULATED PLASTIC STRAIN, p_{gr}

The cumulated plastic strain was used in the crack initiation criterion of Manonukul [Manonukul 04]. This indicator shows the cumulated plastic deformation during fatigue cycling, which is different from the plastic deformation amplitude that shows plastic deformation only at certain time. The equivalent cumulated plastic strain in each surface grain is calculated as follows:

$$p_{gr} = \int_{t_0}^{t_1} \sqrt{\frac{2}{3}\left\{\left(\dot{\varepsilon}_{11}^{p,gr}\right)^2 + \left(\dot{\varepsilon}_{22}^{p,gr}\right)^2 + \left(\dot{\varepsilon}_{33}^{p,gr}\right)^2 + 2\left[\left(\dot{\varepsilon}_{12}^{p,gr}\right)^2 + \left(\dot{\varepsilon}_{23}^{p,gr}\right)^2 + \left(\dot{\varepsilon}_{31}^{p,gr}\right)^2\right]\right\}} \qquad \text{(V-23)}$$

where $\dot{\varepsilon}_{11}^{p,gr}$, $\dot{\varepsilon}_{22}^{p,gr}$, $\dot{\varepsilon}_{33}^{p,gr}$, $\dot{\varepsilon}_{12}^{p,gr}$, $\dot{\varepsilon}_{23}^{p,gr}$, $\dot{\varepsilon}_{31}^{p,gr}$ are the rate of the six components of the plastic strain in a given grain, and t_0, t_1 are the times corresponding to the beginning and the end of the fatigue cycling.

The distribution of p_{gr} for the 12 surface grains showing cracks and the 488 surface grains without any crack is shown in FIG. V.12. For the grains without cracks, p_{gr} has a distribution between 1.9 and 3.2. For the grains showing cracks, a narrow distribution can be seen: p_{gr} varies between 2.6 and 3.1. However, in the range p_{gr} > 3.0, the high-value zone, the grains showing cracks occupy a proportion (50.0 %) that is larger than that of the grains without cracks 21.3 %). This shows that more cumulated plastic deformation can be seen in cracked grains. p_{gr} is a very good indicator of fatigue damage.

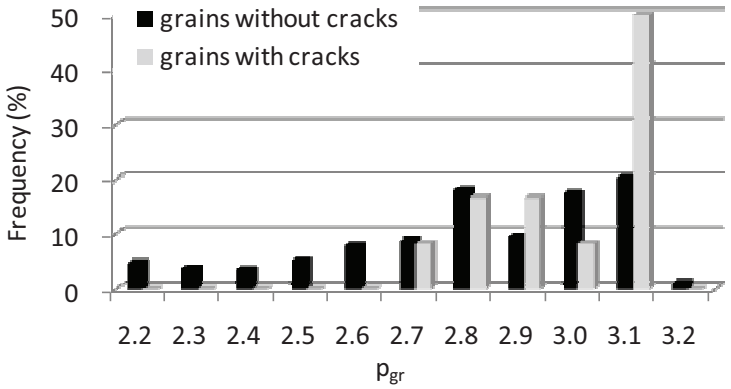

FIG. V.12 - Distributions of cumulated plastic deformation p_{gr} among 12 surface grains showing cracks and 488 surface grains without cracks. The distribution is obtained after a simulation of 192 cycles with $\Delta\varepsilon_t$ = 0.5 %.

- MAXIMAL SHEAR STRAIN, $|\gamma|_{gr,max}$

The macroscopic shear strain was used in the crack initiation criterion of Fatemi [Fatemi 88]. We adapted this indicator to the grain scale and calculated the maximal shear strain among the 12 slip systems of each surface grain:

$$|\gamma|_{gr,max} = \max_{\substack{i=1,12 \\ t=t_0,t_1}} (|\gamma|_i) \quad \text{(V-24)}$$

where $|\gamma|_i$ is the shear strain in slip system i (i=1-12), and t_0, t_1 are the times corresponding to the beginning and the end of the fatigue cycling.

The distribution of $|\gamma|_{gr,max}$ for the 12 surface grains showing cracks and 488 grains without crack is shown in FIG. V.13. A quasi normal distribution can be seen for the two types of grains, centered on 0.38. For the grains without crack, $|\gamma|_{gr,max}$ has a distribution between 0.0017 and 0.0065. Over 50 % of the grains without crack have a value of $|\gamma|_{gr,max}$ between 0.003 and 0.005. For the grains showing cracks, a similar distribution of $|\gamma|_{gr,max}$ can be seen and about 3/4 of the grains have a value of $|\gamma|_{gr,max}$ between 0.0025 and 0.0045. As no evident difference can be seen between the grains with or without cracks, $|\gamma|_{gr,max}$ is therefore not a suitable indicator of plastic deformation and of fatigue damage.

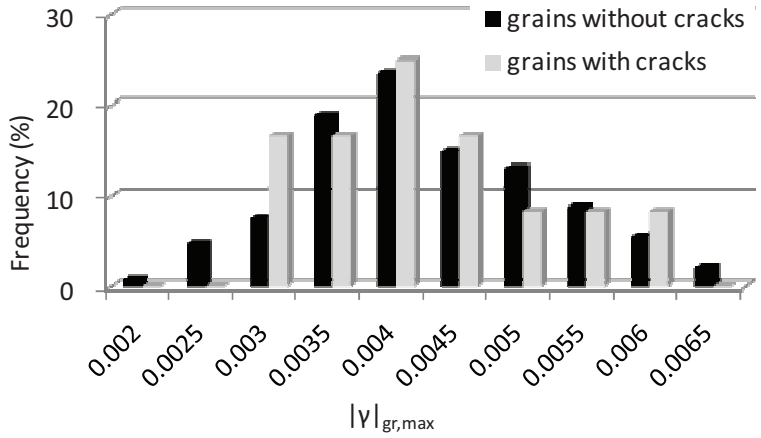

FIG. V.13 - Distributions of maximal shear strain $|\gamma|_{gr,max}$ among 12 surface grains showing cracks and 488 surface grains without cracks. The distribution is obtained after a simulation of 192 cycles with $\Delta\varepsilon_t$ = 0.5 %.

- MAXIMAL SHEAR STRESS, $|\tau|_{gr,max}$

The maximal shear stress in a given grain was used in the crack initiation criterion of Tanaka and Mura [Tanaka 81]. In the present study, this indicator is calculated as:

$$|\tau|_{gr,max} = \max_{\substack{i=1,12 \\ t=t_0,t_1}} (|\tau|_i) \quad \text{(V-25)}$$

where $|\tau|_i$ is the shear stress in slip system i (i = 1-12), and t_0, t_1 are the time corresponding to the beginning and the end of the fatigue cycling.

The distribution of $|\tau|_{gr,max}$ in the 12 surface grains showing cracks and in the 488 grains without crack is shown in FIG. V.14. For both grain types, a quite narrow distribution of $|\tau|_{gr,max}$ can be seen (most of them lie in the range [114, 116 MPa]). Besides, in the high-value zone, the grains showing cracks do not occupy a larger proportion than the grains without crack. $|\tau|_{gr,max}$ is therefore not a good indicator of fatigue damage.

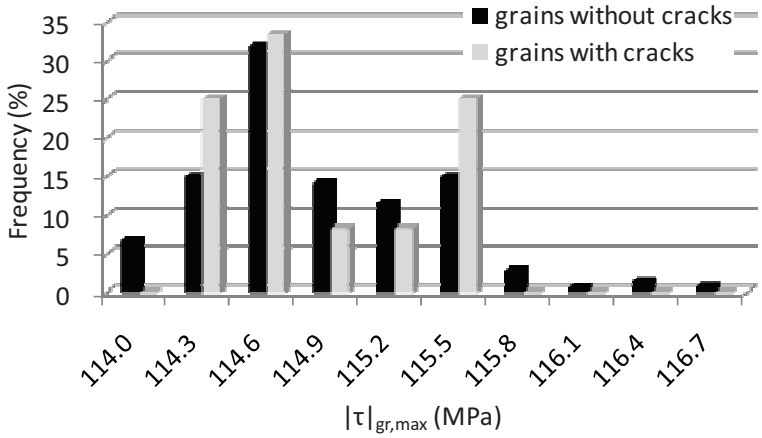

FIG. V.14 - Distributions of maximal shear stress $|\tau|_{gr,max}$ among 12 surface grains showing cracks and 488 surface grains without cracks. The distribution is obtained after a simulation of 192 cycles with $\Delta\varepsilon_t$ = 0.5 %.

➢ MAXIMAL ABSOLUTE VALUE OF τ_d/τ_p, $\left|\tau_d/\tau_p\right|_{gr,max}$

Déprés showed that under biaxial cyclic loading as thermal fatigue, plastic strain localization is strongly linked to the activation of two glide systems in double glide configuration [Déprés 04]. These two systems are slip systems sharing a common Burgers vector. In that condition, shear stresses in these two systems may be of great importance. Déprés proposed a criterion including the ratio of shear stresses in these two activated slip systems, that is to say, in the primary and deviate slip systems. Based on this assumption, we defined an indicator as:

$$\left|\tau_d/\tau_p\right|_{gr,max} = \max_{t=t_0,t_1}\left(\left|\tau_d/\tau_p\right|\right) \quad \text{(V-26)}$$

where τ_p is the maximal shear stress in all slip systems, τ_d is the deviated shear stress (shear stress in the slip system with the same slip direction as the slip system showing maximal shear stress), and t_0, t_1 are the time corresponding to the beginning and the end of the fatigue cycling.

The distribution of $\left|\tau_d/\tau_p\right|_{gr,max}$ for the 12 surface grains showing cracks and the 488 surface grains without cracks is shown in FIG. V.15. Although both have a wide distribution between 0.6 and 1.0, about 2/3 of grains with or without crack have a very high value between 0.95 and 1.0. For the grains showing cracks, the remaining third of the grains have a value of $\left|\tau_d/\tau_p\right|_{gr,max}$ mainly in the zone [0.75, 0.85]. However, the remaining third of the grains without cracks correspond to $\left|\tau_d/\tau_p\right|_{gr,max}$ evenly distributed in the zone [0.70, 0.95]. As the grains showing cracks do not occupy a larger proportion in the high-value zone, $\left|\tau_d/\tau_p\right|_{gr,max}$ does not seem a good indicator of fatigue damage.

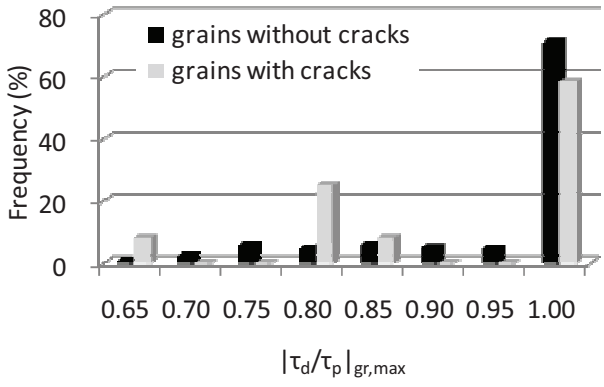

FIG. V.15 - Distributions of maximal absolute value of τ_d/τ_p among the 12 surface grains showing cracks and 488 surface grains without cracks. The distribution is obtained after a simulation of 192 cycles with $\Delta\varepsilon_t$ = 0.5 %.

➢ MAXIMAL CUMULATED ABSOLUTE VALUE OF SHEAR STRAIN, $(\int|\dot{\gamma}|)_{gr,max}$

At the grain scale, plastic strain develops under shearing. It seems then natural to evaluate if shear strain is correlated to crack initiation. We defined then an indicator based on the cumulated plastic strain, but at the slip system scale. The maximal cumulated absolute value of shear strain among the 12 slip systems in each surface grain is calculated as:

$$(\int|\dot{\gamma}_i|)_{gr,max} = \max_{i=1,12}\left(\int_{t_0}^{t_1}\left|\frac{d\gamma_i}{dt}\right| dt\right) \quad \text{(V-27)}$$

where $\dot{\gamma}_i = \frac{d\gamma_i}{dt}$ is the rate of shear strain in slip system i (i=1, 12), and t_0, t_1 are the times corresponding to the beginning and the end of the fatigue cycling.

The distribution of $(\int|\dot{\gamma}_i|)_{gr,max}$ for the 12 surface grains showing cracks and the 488 surface grains without cracks is shown in FIG. V.16. As indicator $|\gamma|_{gr,max}$, a quasi normal distribution can be seen for both the grains with or without crack, centered around 2.6. As no evident difference can be seen between the grains with or without crack, $|\gamma|_{gr,max}$ is therefore not a suitable indicator of fatigue damage.

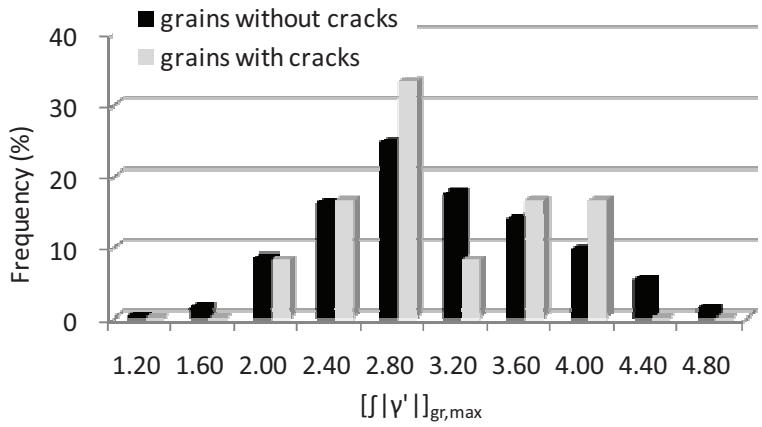

FIG. V.16 - Distributions of maximal cumulated absolute value of shear strain $(\int|\dot{\gamma}|)_{gr,max}$ among 12 surface grains showing cracks and 488 surface grains without cracks. The distribution is obtained after a simulation of 192 cycles with $\Delta\varepsilon_t$ = 0.5 %.

➢ MAXIMAL DISLOCATION DENSITY, ρ_{max}

The accumulation of plastic strain is linked to the multiplication of dislocations and leads to crack initiation [Déprés 04]. Indicators based on the dislocation densities have also been tested. The first one is the maximal dislocation density among the 12 slip systems in a given surface grain. It is defined as:

$$\rho_{max} = \max_{\substack{i=1,12 \\ t=t_0,t_1}} (\rho_i) \tag{V-28}$$

where ρ_i is the dislocation density in slip system i (i=1, 12), and t_0, t_1 are the time corresponding to the beginning and the end of the fatigue cycling.

The distribution of ρ_{max}/ρ_0 (ρ_0 is initial dislocation density) for the 12 surface grains showing cracks and the 488 surface grains without cracks is shown in FIG. V.17. It can be seen that for the grains without cracks, about 3/5 of the grains have a value of ρ_{max}/ρ_0 between 1.34 and 1.39. For the grains showing cracks, over 70 % of them have a value of ρ_{max}/ρ_0 between 1.35 and 1.39. There is no much difference between these two types of grains. ρ_{max} does thus not seem a suitable indicator.

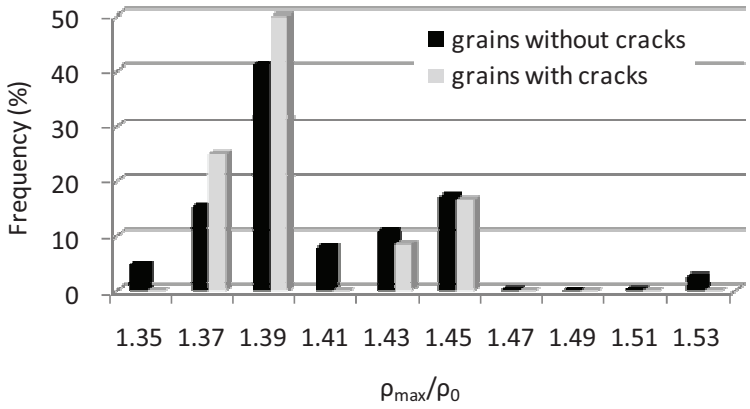

FIG. V.17 - Distributions of the ratio between maximal dislocation density and the initial dislocation density among the 12 slip systems, ρ_{max}/ρ_0, of 12 grains showing cracks and the 488 surface grains without cracks. The distribution is obtained after a simulation of 192 cycles with $\Delta\varepsilon_t$ = 0.5 %.

➢ SUM OF DISLOCATION DENSITIES, ρ_{gr}

The second indicator based on dislocation densities is the sum of dislocation densities over the 12 slip systems in a given surface grain and is calculated as:

$$\rho_{gr,max} = \max_{t=t_0,t_1}\left(\sum_{i=1}^{12}\rho_i\right) \quad \text{(V-29)}$$

where ρ_i is dislocation density in slip system i (i=1, 12) in a given surface grain, and t_0, t_1 are the time corresponding to the beginning and the end of the fatigue cycling.

The distribution of $\rho_{gr,max}/\rho_0$ (ρ_0 is the initial dislocation density) for the 12 surface grains showing cracks and the 488 surface grains without cracks is shown in FIG. V.18. The distributions of this indicator are similar to those of the ρ_{max}/ρ_0: for the grains without cracks, about 60% of the grains have a value of ρ_{max}/ρ_0 less than 14.0; and for the grains showing cracks, over 70 % of them have a value of ρ_{max}/ρ_0 less than 14.0. There is no much difference between these two types of grains. $\rho_{gr,max}$ is thus not a suitable indicator.

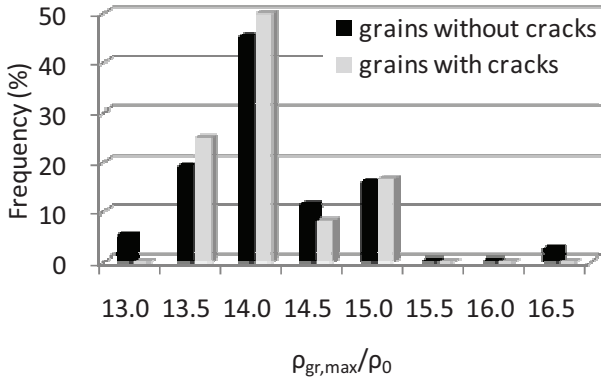

FIG. V.18 - Distributions of the ratio between the sum of dislocation densities and the initial dislocation density $\rho_{gr,max}/\rho_0$ among 12 surface grains showing cracks and 488 surface grains without cracks. The distribution is obtained after a simulation of 192 cycles with $\Delta\varepsilon_t$ = 0.5 %.

➢ CONCLUSIONS OF INDICATOR ANALYSIS

In the sections above, the distributions of the values of eight indicators were compared for grains with and without cracks. The indicators $\left(\varepsilon_{eq}^{p}\right)_{gr,max}$ and p_{gr} show good performance in separating the grains showing cracks from the grains without cracks in the high-value zone (the grains showing cracks occupy a much larger proportion in this zone). The remaining six indicators present either a normal ($|\gamma|_{gr,max}$ and $(\int|\dot{\gamma}|)_{gr,max}$), or a very narrow distribution (p_{max} and p_{gr}), or a distribution with a dominating proportion in a very narrow zone ($|\tau_d/\tau_p|_{gr,max}$). However, neither of the remaining six indicators present acceptable difference between grains with and without crack, especially in the high-value zone. They do not seem to be suitable indicators of fatigue damage.

➢ NOTES

In this study, the choice of the 12 grains showing cracks and the 488 surface grains without cracks was based on the observation on SEM after 2000 cycles. However, because of the limits of time and computer capacities, the simulations of indicator evolution were stopped after 192 cycles. In order to ensure that the analytic results obtained above have a sense, it should be verified that the simulated results after 192 cycles maintains the same distribution as that after 2000 cycles. In other words, the value of each indicator should have a constant variation rate after 192 cycles.

FIG. V.19 presents the evolution of the maximal shear stress $|\tau|_{gr,max}$ as a function of the number of cycles. This indicator has similar initial values (112.5-113 MPa) in all the grains. Before 20 cycles, the maximal shear stress increases in all grains, but with various rates: in some grains, $|\tau|_{gr,max}$ increases much more quickly than those in other grains. The order of grains with maximal $|\tau|_{gr,max}$ changes evidently. After 20 cycles, the rate of $|\tau|_{gr,max}$ slows down. After 50 cycles, $|\tau|_{gr,max}$ saturates in most of the grains, there is no longer increase of $|\tau|_{gr,max}$. The distribution of $|\tau|_{gr,max}$ remains the same after 50 cycles.

FIG. V.20 presents the evolution of $\left(\varepsilon_{eq}^{p}\right)_{gr,max}$ during the cycling. The value of $\left(\varepsilon_{eq}^{p}\right)_{gr,max}$ decreases during the first 10 cycles and then remains quasi-stable. The decrease of $\left(\varepsilon_{eq}^{p}\right)_{gr,max}$ is due to the hardening of material during the first loading cycles. As the elastic strain is proportional to the stress, which is increasing, the plastic strain decreases to keep the total strain constant. As no cyclic softening of material is taken into account by the model, the plastic strain remains stable afterwards.

The values of the two cumulated indicators p_{gr} and $(\int|\dot{\gamma}_i|)_{gr,max}$ keep increasing during the cycling. Although not stable, both of them have constant increasing rate after a few cycles, which ensures that their distribution remains the same.

As a conclusion, the simulated results seem reasonable and the results of the indicators after 192 cycles can be used in the analysis of crack initiation after a number of cycles much larger.

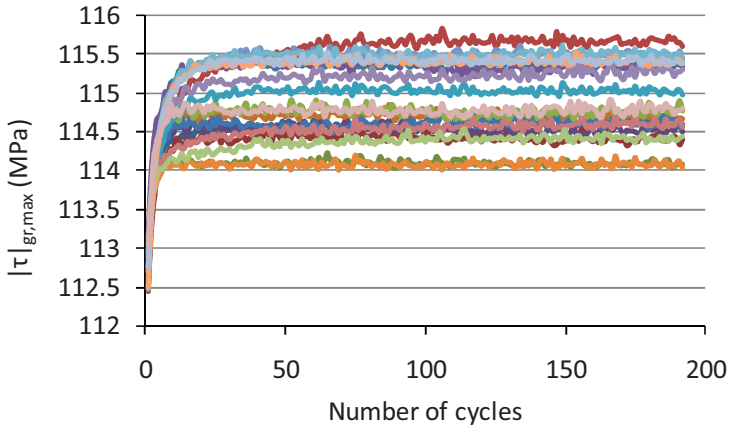

FIG. V.19 - Evolution of $|\tau|_{gr,max}$ as a function of the number of cycles in 20 random surface grains.

$\Delta\varepsilon_t$=0.5 %.

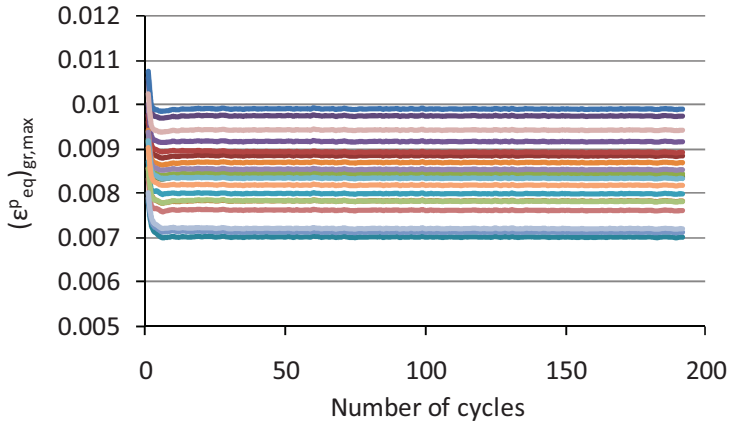

FIG. V.20 - Evolution of $\left(\varepsilon_{eq}^{p}\right)_{gr,max}$ as a function of the number of cycles in 20 random surface grains.

$\Delta\varepsilon_t$ = 0.5 %.

V.3.3. FORMULATION AND DISCUSSION OF TWO INITIATION CRITERIA

After evaluating crack initiation indicators, two crack criteria will be analyzed in this section. The first criterion proposed by T. Mura is based on Gibbs' free energy. This criterion has been widely discussed and several extensions of this criterion have been proposed. The second criterion to be presented was proposed by C. Déprés and is based on dislocation dynamics simulations. In this section, the formulations and the simulated results of these two criteria will be given.

➢ INITIATION CRITERION OF T. MURA

The initiation criterion of T. Mura [Mura 94] is based on Gibbs' free energy, which is considered to be in charge of the evolution of dislocation structures. The author assumes a crack initiates when the local accumulated energy is larger than the surface energy needed to create a decohesion surface. The length of an initiated crack is supposed to be the same as the grain size. The number of cycles to crack initiation, N_{ini}, is expressed by:

$$N_{ini} = C\frac{\mu\gamma_{surf}}{\bar{d}p^2(1-\nu)^2}\frac{1}{\left(|\tau|_{gr,max}-\tau_{PSB}\right)^2} \quad \text{(V-30)}$$

with C a material parameter, μ the shear modulus, ν the Poisson's ratio, γ_{surf} the specific energy of surface creation, $\bar{d}$ the grain size, p a factor of irreversibility of slip, $|\tau|_{gr,max}$ the absolute value of the maximal shear stress in the 12 slip systems of a given grain and τ_{PSB} the critical shear stress for the appearance of slip bands.

We chose arbitrary τ_{PSB} = 80 MPa in order to be able to compare grains with and without cracks. For the material studied here, the first part of formula (V-22), $k = C\frac{\mu\gamma_{surf}}{\bar{d}\,p^2(1-\nu)^2}$, is a constant and can be obtained by inverse method. The number of cycles to crack initiation for crack A was identified by means of image correlation (cf section IV.4.3, N_{ini} = 1500). The maximal shear stress in the grain where crack A initiated was obtained from the simulation considering the grain orientation. k is then obtained through formula (V-22), k = 1.803 x 10^6.

So, for a given material, N_{ini} depends only on the value of $|\tau|_{gr,max}$, which is linked to the amplitude of stress and slip system orientation.

First predictions of the number of cycles to crack initiation have been done. FIG. V.21 shows the number of cycles N_{ini} predicted by Mura's model for the 12 cracks during the first 192 cycles with a strain amplitude of 0.5 %. Because of the cyclic hardening, N_{ini} decreases and then stabilizes. At the end of cycling, N_{ini} varies between 1440 and 1570 cycles.

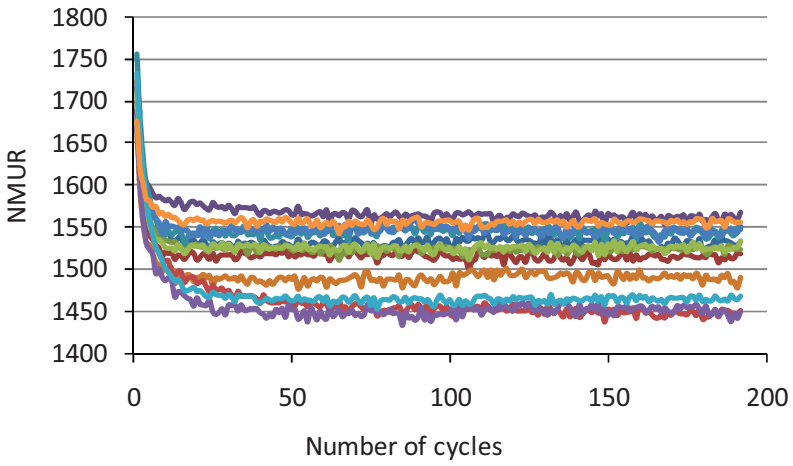

FIG. V.21 - Number of cycles to crack initiation calculated for 12 observed grains showing cracks during the first 192 cycles with a strain amplitude of 0.5 %, according to the criterion of T. Mura [Mura 94].

The predicted N_{ini} using the initiation of T. Mura, NMUR, for the 12 grains showing cracks and 488 cracks without cracks are shown in FIG. V.22. The maximal shear stress in each grain during 192 cycles is used. It can be seen that most of the predictions lie between 1400 and 1600 cycles. However, it is not possible to distinguish grains with and without crack using the criterion of Mura. This result agrees with the analysis made on indicator $|\tau|_{gr,max}$ in section V.3.2. As no difference was seen in the distribution of $|\tau|_{gr,max}$ for the grains with and without crack, no difference either is seen using the criterion based on this indicator.

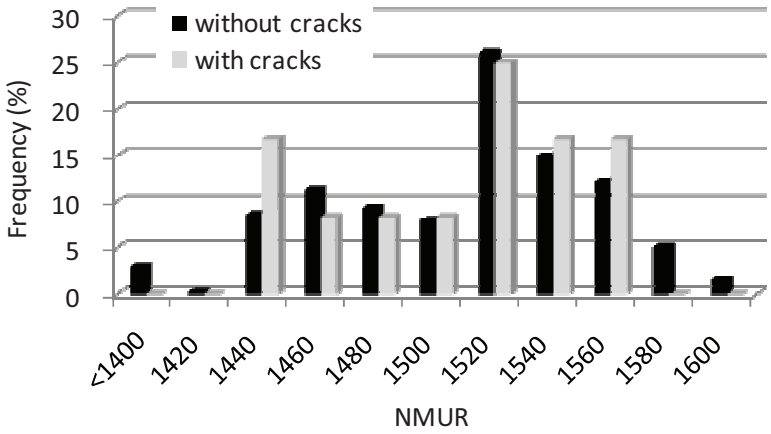

FIG. V.22 - Predicted numbers of cycles to crack initiation for the 12 surface grains showing cracks and the 488 surface grains without cracks after a tension-compression fatigue test of 2000 cycles using the crack initiation of T. Mura [Mura 94], based on the maximal shear stress in each grain during 192 cycles. $\Delta\varepsilon_t$=0.5 %.

➢ INITIATION CRITERION OF C. DÉPRÉS

Using discrete dislocation simulations, C. Déprés studied the evolutions of microstructure of dislocations and the relief induced at the free surface of a grain under biaxial fatigue conditions [Déprés 04]. He analyzed especially the factors influencing irreversible slips as the geometry of the grain and loading parameters as the loading type, the plastic strain amplitude and the mean plastic strain. He proposed a criterion assuming that crack initiation occurs when the irreversible strain cumulated in surface (number of PSB multiplied by the plastic strain cumulated in each band) reaches a threshold value:

$$\sqrt{N_{ini}} = \left(\frac{\tau_p}{\tau_d}\right)^{1.28} \frac{D_g}{h_g} \frac{1}{\left(1+2\frac{\left|\overline{\varepsilon_p^{VM}}\right|}{\Delta\varepsilon_p^{VM}}\right)} \frac{\gamma_{lim\,(\Delta\varepsilon_p)}^{surf}}{\Delta\varepsilon_p^{VM}} \tag{V-31}$$

The parameters introduced in the formulation above present the influences from two aspects:

- *Loading parameters.* τ_d is the deviated shear stress, τ_p is the primary shear stress. These parameters present the influence of loading type. In case of double slip, the formation of persistent slip bands and lines along two directions at the surface will be induced and more damage will be able to be cumulated. Thus a larger number of cycles to crack initiation is expected in this case. $\Delta\varepsilon_p^{VM}$ is the amplitude of plastic deformation in a surface grain. The plastic strain at the surface is proved to be proportional to the applied plastic strain. $\overline{\varepsilon_p^{VM}}$ is the mean plastic deformation. By carring out four pure shear tests with the same plastic strain amplitude but different mean plastic deformations, Déprés found the cumulated strain at the surface is approximately proportional to $\left(1+2\frac{\left|\overline{\varepsilon_p^{VM}}\right|}{\Delta\varepsilon_p^{VM}}\right)$.
- *Geometric parameters.* D_g, is the grain size, h_g is the depth of the grain below the surface. With the same grain size D_g, a higher h_g means a grain more elongated, and Déprés found that in this case, the cumulated irreversible plastic strain at the surface depend linearly on the grain depth.

τ_d, τ_p, $\overline{\varepsilon_p^{VM}}$ and $\Delta\varepsilon_p^{VM}$ can be obtained from the simulation in each surface grain using the methodology defined in section V.3.2. As the simulations are carried out at mean strain null, $\overline{\varepsilon_p^{VM}}$ = 0.

D_g was measured on EBSD analysis, D_g = 50 µm. Moreover, we assume that for a surface grain, h_g = D_g/2 which is consistent with the identification of the localization law for the surface grains.

The threshold value of the cumulative irreversible strain is evaluated from data of the literature. The height of the persistant slip bands leading to crack initiation is evaluated to h_g = 250 nm in a stainless

steel AISI 316L and their thickness to d_g = 500 nm [Man 02]. Assuming that the bands emerge at the surface with an angle of 45°, it is possible to write:

$$\gamma^{surf}_{lim\,(\Delta\varepsilon_p)} = \sqrt{2}\frac{h_b}{d_b} = 0.7 \qquad \text{(V-32)}$$

According to [Man 02], h_b is equal to 250 nm for an AISI 316L stainless steel, and d_b = 500 nm.

According to this criterion, the number of cycles of crack initiation, N_{ini}, depends on 4 parameters : τ_d, τ_p, $\overline{\varepsilon_p^{VM}}$ and $\Delta\varepsilon_p^{VM}$. This is different from the model of T. MURA. If the average plastic deformation is zero (the case for this study), N_{ini} depends only on τ_d, τ_p and $\Delta\varepsilon_p^{VM}$.

The criterion of Déprés predicts a number of cycles to crack initiation that is much larger than that observed in the fatigue test. In order to compare the observed and simulated results, the simulated number of cycles to crack initiation was divided by 30. Doing this, the number of cycles to crack initiation for the observed crack would be around 1500. FIG. V.23 presents the number of cycles to crack initiation calculated for the 12 observed grains showing cracks during the first 192 cycles. N_{ini} increases in the first number of cycles, then stabilizes.

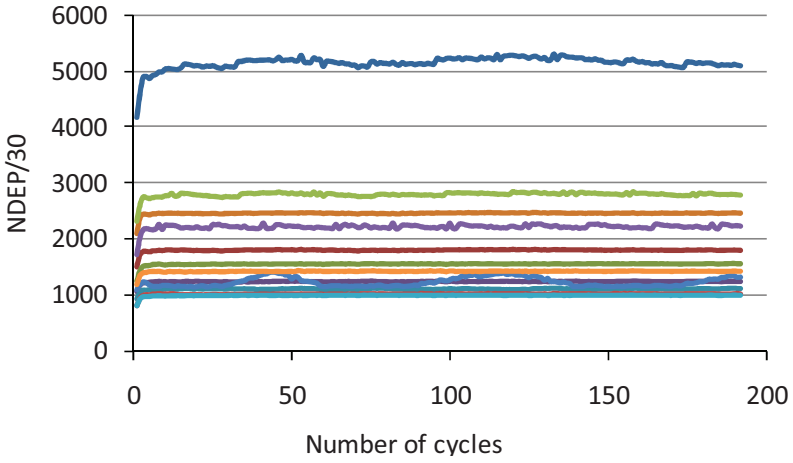

FIG. V.23 - Number of cycles to crack initiation calculated for 12 observed grains showing cracks during the first 192 cycles with a strain amplitude of 0.5%, according to the criterion of Déprés [Déprés 04].

The predicted number of cycles for crack initiation with the criterion of Déprés for the 12 grains showing cracks and 488 cracks without cracks are shown in FIG. V.24. The minimum value of the number of cycles to crack initiation calculated during the first 192 cycles is used. In order to be compared to the experimental results, the number of cycles simulated was divided by 30. It can be seen that for most of the grains with or without crack observed, the number of cycles predicted lies between 1000 and 2000. However, no evident difference can be seen between the two distributions.

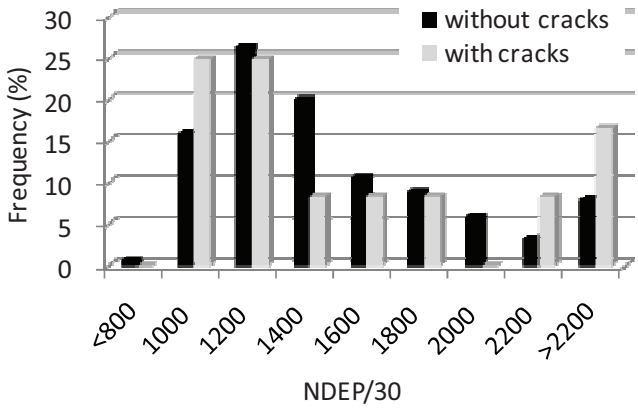

FIG. V.24 - Predicted numbers of cycles to crack initiation for the 12 surface grains showing cracks and the 488 surface grains without cracks after a tension-compression fatigue test of 2000 cycles using the crack initiation criterion of Déprés [Déprés 04]. $\Delta\varepsilon_t$ = 0.5 %.

V.4. CONCLUSION

Because surface grains are less constraint by their neighbors, for a given stress level, plastic slip is larger in surface grains than in grains in the bulk having the same crystallographic orientation. The stress-strain relationship of surface grains can thus not be calculated by a classical localization law. A specific localization law must then be defined to correctly reflect the mechanical behavior of grains at the surface. A first localization law was introduced which was proposed by M. Sauzay [Sauzay 00a]. This localization law enables to account for plastic surface grains embedded in an elastic media. Moreover, it is usable only for monotonous loadings. For these two conditions, a new localization law of type Cailletaud-Pilvin is considered. Finite element simulations have been used to identify the parameters of this law.

A review of fatigue life criteria and crack initiation criteria was then made. Instead of testing all these fatigue criteria, the values of eight indicators used in these criteria were calculated. The distributions of the values of these indicators were analyzed and compared for 12 observed grains showing cracks and 488 surface grains without cracks. The comparison showed that two indicators, the equivalent strain amplitude, $\left(\varepsilon_{eq}^{p}\right)_{gr,max}$, and the cumulated plastic strain, p_{gr}, have relatively higher values in the grains showing cracks than in the grains without cracks. This result confirms that they are two good indicators of fatigue damage. However, the six other indicators as crack initiation criteria proposed by Mura and Déprés do not let appear any difference between the distributions in grains showing cracks or not. None of these criteria above seems suitable for the prediction of crack initiation under the conditions tested in this study.

GENERAL CONCLUSION AND PERSPECTIVE

The mechanisms for crack initiation in fatigue are not totally understood, which explains also the lack of prediction tools. This work lies within the scope of the study of crack initiation criteria in fatigue under variable amplitude loadings. The first objective of this work is thus to provide a numerical frame allowing to test initiation criteria in fatigue. The second objective is to validate the proposed approach and to discriminate between existing criteria from the literature on the same experimental data base.

The mechanical behavior of the austenitic stainless steel studied was first characterized with one monotonous and three tension-compression cyclic tests. A cyclic hardening can be observed during the first cycles, followed by a softening that leads to a stabilization or quasi-stabilization. The hysteresis loops at 1000^{th} cycle shows a strong kinematic hardening.

In order to be able to account the mechanical behavior of the studied material under complex cyclic loadings, a model was chosen which was able to simulate a large number of cycles, especially under variable amplitude fatigue. The microstructure having only one heterogeneity scale, a one site self-consistent model was chosen. As the material does only show a slight texture, the material can be considered as isotropic and a random distribution of 500 orientations or a selected distribution of 40 orientations proposed in [Cailletaud 92] [Pilvin 90] were adopted in the simulation. The localization law proposed by Cailletaud and Pilvin [Cailletaud 92] is selected in this study, as it is capable of simulating complex cyclic experimental tests. Concerning the crystalline plastic behavior description, a crystalline constitutive law based on the evolution of dislocation densities in slip planes was selected.

The identification of the parameters used in the simulation was carried out using either direct measurement on experimental results, either the literature, or an inverse method based on a genetic algorithm. The inverse identification uses the experimental results of the first 5 cycles of a tension-compression cyclic test with a strain amplitude of 0.5 %. Simulated results are in globally good agreement with the experimental ones. The self-consistent condition has been verified during the simulation of a cyclic test.

Surface damage was studied crack initiation during a tension-compression cyclic test carried out with an in situ observation system. The specimen surface was chemically etched before the test in order to reveal the grain boundaries. The test was interrupted every 100 cycles in order to observe the surface of the specimen in a zone of 1080 µm × 400 µm. It is shown that over 75 % of the slip markings appear before 500 cycles. Crack initiation was analyzed in a bigger zone representing 2100 µm × 4000 µm. The crystallographic orientations in this zone were measured by EBSD and crack orientations were measured to identify the slip systems associated to cracks. 94% of cracks initiate in slip bands or in grain boundaries. Crystallographic analysis on the orientations of slip systems (slip system/loadings axis, μ, and slip system/normal to the free surface, β) or surface PSMs (PSM/loading axis, Π) associated to 91 initiated PSB cracks have been made. About 2/3 cracks initiate in slips systems with the highest Schmid Factor. About 70 % of the cracks initiate with an angle Π in the range [50, 80°] and an angle β in the range [40, 70°]. It has been found that if a slip system with the maximal Schmid factor in a grain has an orientation of about 45° with respect to the load axis, which is the case of grain A, there is a big chance that another slip system will be activated. At last, digital image correlation was used to measure the number of cycles to crack initiation.

As the grains at the surface are less constraints than the same grain in the bulk, they show a higher strain level. Localization laws of the literature were analyzed, and a specific localization law was proposed to account for elasto-plastic crystalline grains at the surface of an elasto-plastic matrix. In order to be able to use the localization law under cyclic loadings, a form similar to the localization law of Cailletaud and Pilvin was chosen. Parameters of the law were identified using a Finite Element calculation to account for the mean stress of a semi-hemispherical grain at the surface of a semi-infinite matrix. The full calculation includes then two parts: the first one corresponds to the modeling of the average behavior of the material trough a self-consistent model and the second to the prediction of the stress-strain relation in surface grains. Both use the same crystalline behavior but the localization laws are different.

Based on the simulated results, the analysis on the distribution of indicator values is done on 12 observed grains showing cracks and 488 surface grains without cracks. Two indicators, the equivalent strain amplitude, $\left(\varepsilon_{eq}^{p}\right)_{gr,max}$, and the cumulated plastic strain, p_{gr}, are found to be suitable indicators of fatigue damage as they occupy a quite larger proportion in the high-value zone for cracked grains than those for crack-free grains. Then, two crack initiation criteria using these two indicators [Mura

94] [Déprés 04] are presented and used in the simulation. However, neither of these two criteria above seems suitable to predict crack initiation in this study.

Some questions have been asked during this study and remain open.

Due to the large size of surface domain to analyze to establish crack initiation statistics, crack initiation criteria tested here were compared to a limited experimental data base. It seems then necessary to extend this data base to other loading paths, including notably the biaxial fatigue, and to enlarge the range of strain amplitude tested.

The cyclic softening of material was not considered in the simulation in this study. However, the cyclic hardening/softening of the various grains may enhance stress/strain concentration in some of these grains which could favor earlier crack initiation. In the future, it would be interesting to integrate this cyclic softening in the simulation in order to evaluate the material behavior better. The modeling of the cyclic softening should nevertheless be carried out accounting for dislocation microstructure evolutions.

In this study, the influence of neighbor grains on the crack initiation was not considered. In fact, the shape, size and orientation of neighbor grains may all introduce scattering on the number of cycles to crack initiation. It would be interesting to analyze this influence and to integrate it into the model.

Only two crack initiation criteria, those of T. Mura and of C. Déprés, were considered in this study. It would be appropriate to consider other criteria based on the indicators analyzed in the section V.3.2, especially criteria based on the equivalent strain amplitude and the cumulated strain, whose results distinguished the grains showing and without grains.

REFERENCE

ABAQUS 98 ABAQUS Version 5.8 Reference Manuals, Hibbitt, Karlsson and Sorensen Inc., 1998.

Abdul-Latif 02 A. Abdul-Latif, J. P. Dingli and K. Saanouni, Elastic-inelastic self-consistent model for polycrystals, J. Appl. Mech., Vol. 69, pp. 309-316, 2002.

Abdul-Latif 04 A. Abdul-Latif, A comparaison of two self-consistent models to predict the cyclic behavior of polycrystals, J. Appl. Mech., Vol. 126, pp. 62-69, 2004.

Acharya 00 A. Acharya and A. Beaudoin, Grain-size effect in viscoplastic polycrystals at moderate strains, J. Mech. Phys. Solids, Vol. 48, pp. 2213-2230, 2000.

Amelinckx 58 S. Amelinckx, Dislocation patterns in potassium chloride, Acta Metall. Vol. 6, pp. 34-58, 1958.

Amelinckx 64 S. Amelinckx, The direct observation of dislocations, Solid State Physics Supplement, Vol. 6, pp. 15, 1964.

Andrade-Campos 07 A. Andrade-Campos, S. Thuillier, P. Pilvin and F. Teixeira-Dias, On the determination of material parameters for internal variable thermoelastic-viscoplastic constitutive models, Int. J. Plast., Vol. 23, pp. 1349-1379, 2007.

Andrews 00 S. Andrews and H. Sehitoglu, A Computer Model for Fatigue Crack Growth from Rough Surfaces, Int. J. Fatigue, Vol. 22, pp. 619-630, 2000.

ANL 05 Effect of Material Heat Treatment on Fatigue Crack Initiation in Austenitic Stainless teels in LWR Environments, Argonne National Laboratory, U. S. Nuclear Regulatory Commission, 2005.

Antonopoulos 76 J. G. Antonopoulos, L. M. Brown and A. T. Winter, Phil. Mag., Vol. 34, pp. 549, 1976.

Armstrong 62 R. Armstrong, I. Codd, R. Douthwaite and N. Petch, Plastic deformation of polycrystalline aggregates, Phil. Mag., Vol. 7, pp. 45-58, 1962.

Armstrong 66 P. J. Armstrong and C. O. Frederick, A mathematical representation of the multiaxial Bauschinger effect, CEGB Report RD/B/N731, Berkeley Nuclear Laboratories, 1966.

Asaro 85 R.J. Asaro, A. Needleman, Texture development and strain hardening in rate dependent polycrystals, Acta Metall., Vol. 33, pp. 923, 1985.

Ashby 70 M. F. Ashby, The deformation of plastically non-homogeneous alloys, Phil. Mag., Vol. 21, pp. 399-424, 1970.

Ashby 96 M. F. Ashby and D. R. H. Jones, Engineering Materials 1- An Introduction to their Properties and Applications (2nd ed.), Butterworth-Heinemann, 1996.

ASTM 02 ASTM E2208-02, Standard Guide for evaluating non-contacting optical strain measurement systems, ASTM international, 2002.

Aswath 88 P. B. Aswath, S. Suresh, D. K. Holm and A. F. Blom, Load interaction effects on compression fatigue crack growth in ductile solids, J. Eng. Mater. Technol., Vol. 110, pp. 278-285, 1988.

Atkinson 73 J. D. Atkinson, L. M. Brown, R. Kwadjo, W. M. Stobbs, A. T. Winter and P. J. Woods, The structure of persistent slip bands and the fatigue strength of metals, in The Microstructure and Design of Alloys, Proc. ICSMA 3, Vol. 1, pp. 402, 1973.

Aubin 01 V. Aubin, Plasticité cyclique d'un acier inoxydable austéno-ferritique sous chargement biaxial non proportionnel, PhD thesis, Université des Sciences et technologies de Lille, 2001.

Baczmański 04 A. Baczmański and C.Braham, Elastoplastic properties of duplex steel determined using neutron diffraction and self consistent model, Acta Materiala, Vol. 52, pp. 1133-1142, 2004.

Badulescu 11 C. Badulescu, M. Grediac, H. Haddadi, J. -D. Mathias, X. Balandraud, H. -S. Tran, Applying the grid method and infrared thermography to investigate plastic deformation in aluminium multicrystal, Mech. Mater., Vol. 43, pp. 36-53, 2011.

Balint 05 D. Balint, V. Deshpande, A. Needleman and E. Van der Giessen, A discrete dislocation plasticity analysis of grain-size strengthening, Mater. Sci. Eng. A, Vol. 400-401, pp. 186-190, 2005.

Barbe 01a F. Barbe, L. Decker, D. Jeulin and G. Cailletaud, Intergranular and intragranular behavior of polycrystalline aggregates. Part 1: F.E. model, Int. J. Plast., Vol. 17, pp. 513-536, 2001.

Barbe 01b F. Barbe, L. Decker, D. Jeulin and G. Cailletaud, Intergranular and intragranular behavior of polycrystalline aggregates. Part 2: Results, Int. J. Plast., Vol. 17, pp. 537-563, 2001.

Bastenaire 72 F. A. Bastenaire, New Method for the Statistical Evaluation of Constant Stress Amplitude Fatigue-Test Results, Probabilistic Aspects of Fatigue, ASTM STP 511, pp. 3-28, 1972

Bataille 94 A. Bataille and T. Magnin, Surface damage accumulation in low-cycle fatigue: physical analysis and numerical modelling, Acta Metall. Mater., Vol. 42, pp. 3817-3825, 1994.

Bauschinger 86 J. Bauschinger, Mittheilungen XV: Über die Veränderung der Elasticitätsgrenze und der Festigheit des Eisens und Stahls durch Strecken und Quetschen durch Enwaermen und Abkuhlen und durch wiederholte Beanspruchung, Mechanisch-technischen Laboratorium (Munich), 1886.

Benallal 87 A. Benallal and D. Marquis, Constitutive equations for nonproportional cyclic elastoviscoplasticity, J. Eng. Mat. Tech., Vol. 109, pp. 326-336, 1987.

Bergonnier 05 S. Bergonnier, F. Hild, J. Rieunier and S. Roux, Strain heterogeneities and local anisotropy in crimped glass wool, J. Mater. Sci., Vol. 40, pp. 5949-5954, 2005.

Berveiller 79 M. Berveiller and A. Zaoui, An extension of the self-consistent scheme to plastically-flowing polycristals, J. Mech. Phys. Solids, Vol. 26, pp. 325-344, 1979.

Besnard 06 G. Besnard, F. Hild, S. Roux, “Finite-element” displacement fields analysis from digital images: Application to Portevin-Le Châtelier bands, Exp. Mech., Vol. 46, pp. 789-803, 2006.

Besson 01 J. Besson, G. Cailletaud, J. L. Chaboche and S. Forest, Mécanique non-linéaire des matériaux, Hermes, 2001.

Bigoniand 99 D. Bigoniand and B. Loret, Effects of elastic anisotropy on strain localization and flutter instability in plastic solids, J. Mech. Phy. Solids, Vol. 47, pp. 1409-1436, 1999.

Biner 02 S. Biner and J. Morris, A two-dimensional discrete dislocation simulation of the effect of grain size on strengthening behavior, Model. Simul. Mater. Sci. Eng., Vol. 10, pp 617-635, 2002.

Borg 06 U. Borg, Strain gradient crystal plasticity effects on flow localization, Int. J. Plast., Vo. 23, pp. 1400-1416, 2007.

Brown 70 G. M. Brown, A self-consistent polycrystalline model for creep under combined stress state, J. Mech. Phys. Solids, Vol. 18, pp. 367, 1970.

Brown 73 M. W. Brown, K. J. Miller, A theory for fatigue failure under multiaxial stress-strain conditions. Proc. Inst. Mech. Eng. London, Vol. 187, pp. 745-55, 1973.

Budianski 62 B. Budianski, T. T. Wu, Theoretical prediction of plastic strains of polycrystals, Proc. 4th US Nat. Cong. Apll. Mech., pp. 1175. 1962.

Bui 89 H. D. Bui and S. Taheri, La singularité Épine dans les bi-matériaux en thermo-élastoplasticité, C. R. Acad. Sci. Paris, Vol. 309, pp. 1527-1533, 1989.

Bunge 82 H. J. Bunge, Texture analysis in materials science, Butterworths, 1982. (Reprint: Cuvilier Verlag Göttingen 1993).

Cailletaud 91 G. Cailletaud, V. Doquet and A. Pineau, Cyclic multiaxial behaviour of an austenitic stainless steel: microstructural observation and micromechanical modelling. In: K. Kussmaul, D. McDiarmid and F. Socie, Editors, Fatigue Under Biaxial and Multiaxial Loading, Mechanical Engineering Publications, Vol.12, pp. 131-149, 1991

Cailletaud 92 G. Cailletaud, A micromechanical approach to inelastic behaviour of metals, Int. J. Plast., Vol. 8, pp. 55-73, 1992.

Calloch 97 S. Calloch, Essais triaxiaux non-proportionnels et ingénierie des modèles de plasticité cyclique, PhD thesis, ENS de Cachan, 1997.

Carpinteri 01 A. Carpinteri and A. Spagnoli, Multiaxial high-cycle fatigue criterion for hard metals, Int. J. Fatigue, Vol. 22, pp. 135-45, 2001.

Castro 90 R. Castro, Les aciers inoxydable, Les édition de physique, Vol. 3, 1990.

Chaboche 83 J. L. Chaboche and G. Rousselier, On the plastic and viscoplastic constitutive equations - Part I: Rules developped with internal variables concept, J. Press. Vessel Techn., Vol. 105, pp. 153-164, 1983.

Chaboche 91 J. L. Chaboche, D. Nouailhas, D. Pacou and P. Paulmier, Modeling of the cyclic response and ratchetting effects on inconel-718 alloy, Eur. J. Mech. A/Solids, Vol. 10, pp. 101-121, 1991.

Chauvot 00 C. Chauvot, M. Sester, Fatigue crack initiation and crystallographic crack growth in an austenitic stainless steel, Computational Materials Science, Vol. 19, pp. 87-96, 2000.

Chiu 78 Y. P. Chiu, On the stress field and surface deformation in a half space with a cuboidal zone in which initial strains are uniform, J. Appl. Mech., Vol.45, pp. 302-306, 1978.

Cho 99 K. K. Cho, Y. H. Chung, C. W. Lee, S. I. Kwun and M. C. Shin, Effects of grain shape and texture on the yield strength anisotropy of Al-Li alloy sheet, Scripta Mater., Vol. 40, pp. 651-657, 1999.

Choteau 99 M. Choteau, Caractérisation de l'effet Bauschinger en sollicitations uniaxiales d'un acier inoxydable austénitique X2CrNiMo17-12-2, PhD thesis, Université de Sciences et Technologie de Lille 1, 1999.

Chu 93 C. -C. Chu, F. Conle and J. J. Bonnen, Multiaxial stress-strain modelling and fatigue life prediction of SAE axle shafts, In: Symposium on Multiaxial Fatigue (D. L. McDowell and R. Ellis eds.), ASTM STP, Vol. 1191, pp. 37-54, 1993.

Coffin 54 L. R. Coffin, A study of the effects of cyclic thermal stresses on a ductile metal, Trans ASME, Vol. 76, pp. 931-950, 1954.

Conner 04 B. P. Conner, T. C. Lindley, T. Nicholas and S. Suresh, Application of a fracture mechanics based life prediction method for contact fatigue, Int. J. Fatigue, Vol. 26, pp. 511-520, 2004.

Cottrel 53 A. H. Cottrel, Dislocations and Plastic Flow in Crystals, Clarendon Press for Oxford. 1953.

Cottrell 57 A. H. Cottrell and D. Hull, Extrusion and intrusion by cyclic slip in copper. Proc. R. Soc., Vol. A242, pp. 211-213, 1957.

Cox 89 B. N. Cox, Surface displacements and stress field by a semi-ellipsoidal surface inclusion, J. Appl. Mech., Vol. 56, pp. 564-570, 1989.

Crossland 56 G. Crossland, Effect of large hydrostatic pressures on the torsional fatigue strenght of an alloy steel, In: Proceedings of the international conference of fatigue of metals, Inst. Mech. Engrs (London), pp. 138-49, 1956.

Dang Van 89 K. Dang Van, B. Griveau and O. Message, On a new multiaxial fatigue criterion: theory and application, In: Biaxial and multiaxial fatigue EGF, Mech. Eng. Publ. (London), Vol. 3, pp. 479-498, 1989.

Degallaix 84 S. Degallaix, R. Taillard and J. Foct, Role of nitrogen interstitials in plastic fatigue of austenitic stainless steels, Fatigue 84, Vol. 1, pp. 49-59, 1984.

Degallaix 95 S. Degallaix, A. Seddouki, G. Degallaix, T. Kruml and J. Polàk, Fatigue damage in austenitic-ferritic duplex stainless steels, Fatigue Fract. Engng. Mater. Struct., Vol. 18, pp. 65-77, 1995.

Degallaix-Moreuil 86 S. Degallaix-Moreuil, Effect of intersticial and precipitated nitrogen on low-cycle fatigue and tensile plasticity of ZN CND 17-12 (AISI 316L-316LN) austenetic stainless steels, PhD thesis, l'Université des sciences et techniques de Lille Flandre Artois, 1986.

Deperrois 90 A. Deperrois and K. Dang Van, Inclusion de surface et singularité Épine, C.R. Acad. Sci. Paris, Vol. 31, pp. 1285-1290, 1990.

Deperrois 91 A. Deperrois, Sur le calcul des limites d'endurance des aciers. Thesis of Ecole Polytechnique (Palaiseau), 1991.

Déprés 04 C. Déprés, Modélisation physique des stades précurseurs de l'endommagement en fatigue dans l'acier inoxydable 316L, PhD thesis, Institut national polytechnique de Grenoble, 2004.

Differt 86 K. Differt, U. Essmann and H. Mughrabi, A Model of Extrusions and Intrusions in Fatigued Metals: II. Surface Roughening by Random Irreversible Slip, Philos. Mag. A, Vol. 54, pp. 237-258, 1986.

Dingli 00 J. P. Dingli, A. Abdul-Latif and K. Saanouni, Predictions of the complex cyclic behavior of polycrystals using a self-consistent modeling, Int. J. Plast., Vol. 16, pp. 411-437, 2000.

Driver 94 J. H. Driver, D. Juul Jensen, and N. Hansen, Acta Mater., Vol. 42, pp. 3105, 1994.

Edwards 92 L. Edwards and A.T. Ozdemir, NATO ASI Series E, Kluwer Academic, Dordrecht, pp. 545, 1992.

Efstathiou 10 C. Efstathiou, H. Sehitoglu and J. Lambros, Multiscale strain measurements of plastically deforming polycrystalline titanium: Role of deformation heterogeneities, Int. J. Plast., Vol. 26, pp. 93-106, 2010.

El Bartali 09 A. El Bartali, V. Aubin and S. Degallaix, Surface observation and measurement techniques to study the fatigue damage micromechanisms in a duplex stainless steel, Int. J. Fatigue, Vol. 31, pp. 2049-2055, 2009.

Ellyin 93a F. Ellyin and D. Kujawski, A multiaxial fatigue criterion including mean stress effect, In: Advances in multiaxial fatigue (D. L. McDowell and R. Ellis eds.), ASTM STP, Vol. 1191, pp. 55-66, 1993.

Ellyin 93b F. Ellyin and Z. Xia, A general fatigue theory and its application to out-of-phase cyclic loading, J. Eng. Mater. Technol., Vol. 115, pp. 745-756, 1993.

Erieau 04 P. Erieau and C. Rey, Modeling of deformation and rotation bands and of deformation induced grain boundaries in IF steel aggregate during large plane strain compression, Int. J. Plast., Vol. 20, pp. 1763-1788, 2004.

Eshelby 57 J. D. Eshelby, The determination of the elastic field of an ellipsoidal inclusion and related problems, Proc. Roy. Soc. London A, Vol. 241, pp. 376-396, 1957.

Essmann 79 U. Essmann and H. Mughrabi, Annihilation of dislocations during tensile and cyclic deformation and limits of dislocations densities, Phil. Mag., Vol. 40, pp. 731-756, 1979.

Essmann 81 U. Essmann, U. Gösele and H. Mughrabi, A model of extrusions and intrusions in fatigued metals. I. Point-defect production and the growth of extrusions, Philos. Mag. A, Vol. 44, pp. 405-426, 1981.

Evers 04 L. Evers, W. Brekelmans and M. Geers, Scale dependent crystal plasticity framework with dislocation density and grain boundary effects, Int. J. Solids Struct., Vol. 41, pp. 5209-5230, 2004.

Evrard 08 Evrard P., Modélisation polycristalline du comportement plastique cyclique d'un acier inoxydable duplex et validation expérimentale, PhD thesis, Ecole Centrale de Lille, 2008.

Ewing 03 J. A. Ewing and J. C. W. Humfrey, The Fracture of Metals under Repeated Alternations of Stress, Phil. Trans. R. Soc., Vol. A200, pp. 241, 1903.

Figuera 83 J. C. Figuera and C. Laird, Crack Initiation Mechanisms in Copper Polycrystals Cycled under Constant Strain Amplitudes and in Step Tests, Mater. Sci. Eng., Vol. 60, pp. 45-58, 1983.

Findley 56 W. N. Findley, J. J. Coleman and B. C. Handley, Theory of combined bending and torsion fatigue data for 4340 steel, Proceedings of International Conference on Fatigue of Metals, Inst. Mech. Eng., pp. 150-157, 1956.

Findley 59 W. N. Findley, A theory for the effect of mean stress on fatigue of metals under combined torsion and axial load or bending, J. Eng. Indust., Vol. 81, pp. 301-306, 1959.

Fisher 57 J. C. Fisher, J. J. Gilman and W. G. Johnston, Dislocations and Mechanical Properties of Crystals, pp. 116, John Wiley And Sons Inc., 1957.

Fluck 51 P. G. Fluck, The influence of surface roughness on the fatigue life and scatter of test results of two steels, Proc. Am. Soc. Testing Mat., Vol. 51, pp. 584-592, 1951.

Follansbee 91 P. S. Follansbee, and G. T. Gray, The response of single crystal and polycrystal nickel to quasistatic and shock deformation, Int. J. Plasticity, Vol. 7, pp. 651, 1991.

Forsyth 53 P. J. E. Forsyth, Nature, Vol. 171, pp. 172, 1953.

Franciosi 82 F. Franciosi and A. Zaoui, Multislip in f.c.c single crystals : a theoretical approach compared with experimental data, Acta Metall., Vol. 30, pp. 1627-1637, 1982.

Franciosi 84 P. Franciosi, Etude théorique et expérimentale du comportement élastoplastique des monocristaux métalliques se déformant par glissement : modélisation pour un chargement complexe quasi-statique, PhD thesis, Université de Paris XIII, 1984.

Franciosi 85 P. Franciosi, The concepts of latent hardening and strain hardening in metallic single crystals, Acta Metall., Vol. 33, pp. 1601-1612, 1985.

François 91 F. François, A. Pineau and A. Zaoui, Comportement mécanique des matériaux, Viscoplasticité, endommagement, mécanique de la rupture, mécanique du contact, Hermès, 1991.

Friedel 64 J. Friedel, Dislocations (1st ed.), Oxford: Pergamon, 1964.

Frost 82 H. J. Frost and M. F. Ashby, Deformation-Mechanism Maps - The Plasticity and Creep of Metals and Ceramics, Pergamon Press, 1982.

Furukawa 02 T. Furukawa, T. Sugatab, S. Yoshimura and Mark Hoffman, An automated system for simulation and parameter identification of inelastic constitutive models, Comput. Methods Appl. Mech. Engrg. Vol. 191, pp. 2235-2260, 2002

Furukawa 97 T. Furukawa, G. Yagawa, Inelastic constitutive parameter identification using an evolutionary algorithm with continuous individuals, International Journal For Numerical Methods In Engineering, Vol. 40, pp. 1071-1090, 1997.

Garud 81a Y. S. Garud, Multiaxial fatigue: a survey of the state of the art, J. Test Eval, Vol. 9, pp. 165-78, 1981.

Garud 81b Y. S. Garud, A new approach to the evaluation of fatigue under multiaxial loading. J. Eng. Mater. Technol., Vol. 103, pp. 118-25, 1981.

Gaudin 02 C. Gaudin, Etude des mécanismes associés au rochet cyclique d'un acier austénitique AISI 316L, PhD thesis, Université de Technologie de Compiegne, 2002.

Glinka 95 G. Glinka, G. Shen and A. Plumtree, A multiaxial fatigue strain energy density parameter related to the critical plane, Fatigue Fract. Eng. Mater. Struct., Vol. 18, pp. 37-46, 1995.

Glinka 95 G. Glinka, G. Wang and A. Plumtree, Mean stress effects in multiaxial fatigue, Fatigue Fract. Eng. Mater. Struct., Vol. 18, pp. 755-764, 1995.

Glodež 10 S. Glodež, N. Jezernik, J. Kramberger and T. Lassen, Numerical modelling of fatigue crack initiation of martensitic steel, Adv. Eng. Software, Vol. 41, pp. 823-829, 2010.

Goloś 87 K. Goloś and F. Ellyin, A total strain energy density for cumulative fatigue damage, J. Press Vessel Technol, Vol. 110, pp. 36-41, 1987.

Goloś 88 K. Goloś, An energy based multiaxial fatigue criterion, Eng. Trans., Vol. 36, pp. 55-63, 1988.

Grubisic 76 V. Grubisic and A. Simbürger, Fatigue under combined out-of-phase multiaxial stresses, In: International Conference on Fatigue Testing and Design, Soc. Environ. Engrs (London), pp. 27.1-8, 1976.

Gurtin 02 M. E. Gurtin, A gradient theory of single-crystal viscoplasticity that accounts for geometrically necessary dislocations, J. Mech. Phys. Solids, Vol. 50, pp. 5-32, 2002.

Gutierrez-Urrutia 09 I. Gutierrez-Urrutia, S. Zaefferer and D. Raabe, Electron channeling contrast imaging of twins and dislocations in twinning-induced plasticity steels under controlled diffraction conditions in a scanning electron microscope, Scripta Mater., Vol. 61, pp. 737-740, 2009.

Haasen 58 P. Haasen, Plastic deformation of nickel single crystals at low temperatures, Phil. Mag., Vol. 3, pp. 384, 1958.

Halford 66 G. R. Halford, The energy required for fatigue, J. Mater., Vol. 1(1), pp. 15-22, 1966.

Hall 51 E. Hall, The deformation and aging of mild steel: iii. Discussion of results, Proc. Phys. Soc. Lond., Vol. B64, pp. 747-753, 1951.

Han 05 C. -S. Han, H. Gao, Y. Huang and W. D. Nix, Mechanism-based strain gradient crystal plasticity - I. Theory, J. Mech. Phys. Solids, Vol. 53, pp. 1188-1203, 2005.

Hashimoto 83a K. Hashimoto and H. Margolin, The role of elastic interaction stresses on the onset of slip in polycrystalline alpha brass - I. Experimental determination of operating slip systems and qualitative analysis, Acta Metall., Vol. 31, 773-785, 1983.

Hashimoto 83b K. Hashimoto and H. Margolin, The role of elastic interaction stresses on the onset of slip in polycrystalline alpha brass - II. Rationalization of slip behavior, Acta Metall., Vol. 31, pp. 786-800, 1983.

Heinz 92 A. Heinz and P. Neumann, High cyclic fatigue crack initiation in stainless steels, In: ESIS 13 (K. J. Miller and E. R. de los Rios eds.), Mechanical Engineering Publications, pp. 31-54, 1992.

Héripré07 Héripré E., Dexet M., J. Crépin, L. Gélébart, A. Roos, M. Bornert and D. Caldemaison, Coupling between experimental measurements and polycrystal finite element calculations for micromechanical study of metallic materials, Int. J. Plast., Vol. 23, pp. 1512-1539, 2007.

Hild 02 F. Hild, B. Raka, M. Baudequin, S. Roux, and F. Cantelaube, Multiscale displacement field measurements of compressed mineral-wool samples by digital image correlation, Applied Optics, Vol. 41, pp. 6815-6828, 2002.

Hild 06 F. Hild and S. Roux, Digital image correlation: From displacement measurement to identification of elastic properties - A review, Strain, Vol. 42, pp. 69-80, 2006.

Hill 65 R. Hill, Continuum micro-mechanics of elastoplastic polycrystals, J. Mech. Phys. Solids, Vol. 13, pp. 89-101, 1965.

Hoc 01 T. Hoc and S. Forest, Polycristal modelling of IF-TI steel under complex loading path, Int. J. Plast., Vol. 17, pp. 65-85, 2001.

Hook 67 R. E. Hook and J. Hirth, The deformation behavior of isoaxial bicrystals of Fe-3%Si, Acta Metall., Vol. 15, pp. 535-551, 1967.

Horstemeyer 99 M. F. Horstemeyerand and M. I. Baskes, Atomistic finite deformation simulations: a discussion on length scale effects in relation to mechanical stresses, J. Eng. Mates. Technol., Vol. 121, pp. 114, 1999.

Howie 61 A. Howie, Metallurgical Reviews, Vol. 6, pp. 467, 1961.

Huang 00 H. L. Huang and N. J. Ho, The Study of Fatigue in Polycrystalline Copper under Various Strain Amplitude at Stage I: Crack Initiation and Propagation, Mater. Sci. Eng. A, Vol. 293, pp. 7-14, 2000.

Hull 01 D. Hull and D. J. Bacon, Introduction to Dislocations (4th Ed.), Butterworth-Heinemann, 2001.

Hull 55 D. Hull, J. Inst. Metals, Vol. 84, pp. 527, 1955-56.

Humphreys 80 C. J. Humphreys, Imaging of dislocations, Dislocations in Solids, Vol. 5, pp. 1, 1980.

Huntington 58 H. Huntington, In: The elastic constants of crystals (F. Seitz, D. Turnbull eds.), Solid State Physics, Academic Press Incorporation Publishers, 1958.

Hutchinson 70 J. W. Hutchinson, Elastic-plastic behaviour of polycrystalline metals and composites, Proc. R. Soc. Lond., Vol. A319, pp. 247-272, 1970.

Hutchinson 76 J. W. Hutchinson, Bounds and self-consistent estimate for creep of polycrystalline materials, Proc. R. Soc. A, Vol. 348, pp. 101, 1976.

Jahed 06 H. Jahed and A. Varvani-Farahani, Upper and lower fatigue life limits model using energy-based fatigue properties, Int. J. Fatigue, Vol. 28, pp. 467-73, 2006.

Jasiuk 97 I. Jasiuk, P. Y. Sheng and E. Tsuchida, A spherical inclusion in an elastic half-space under shear, J. Appl. Mech., Vol. 64, pp. 471-479, 1997.

Jenkinson 62 A. E. Jenkinson and A. R. Lang, Direct Observations of Imperfections in Crystals, lnterscience, pp. 471, 1962.

Jiménez 06 F. Jiménez, J. M. Cadenas, G. Sánchez, A. F. Gómez-Skarmeta and J. L. Verdegay, Multi-objective evolutionary computation and fuzzy optimization, International Journal of Approximate Reasoning, Vol. 43, pp. 59-75, 2006.

Jin 84 N. Y. Jin and A. T. Winter, Cyclic deformation of copper single crystals oriented for double slip, Acta Metall., Vol. 32, pp. 989-995, 1984.

Kafri 80 O. Kafri, Optics letters, Vol. 5, pp. 555, 1980.

Kafri 90 O. Kafri and I. Glatt, The Physics of Moiré Metrology, J. Wiley & Sons Inc., 1990.

Kalidindi 01 S. R. Kalidindi, Modeling anisotropic strain hardening and deformation textures in low stacking fault energy FCC metals, Int. J. Plast., Vol. 17, pp. 837-860, 2001.

Kamaya 09 M. Kamaya, Influence of bulk damage on crack initiation in low-cycle fatigue of 316 stainless steel, Fatigue Fract. Engng. Mater. Struct., Vol. 33, pp. 94-104, 2009.

Kandil 82 E. A. Kandil, M. W. Brown and K. J. Miller, Biaxial low cycle fatigue of 316 stainless steel at elevated temperatures, 280, The Metals Society (London), pp. 203-210, 1982.

Kim 78a W. H. Kim and C. Laird, Crack nucleation and stage I propagation in high strain fatigue - I. Microscopic and interferometric observations, Acta Meall., Vol. 26, pp. 777-787, 1978.

Kim 78b W. H. Kim and C. Laird, Crack nucleation and stage I propagation in high strain fatigue - II. Mechanism, Acta Metall., Vol. 26, pp. 789-799, 1978.

Kochendorfer 50 A. Kochendorfer, Neue Ergebnisse uber die Verfestigung bei der plastischen Verformung von Kristallen, Z. Metallk, Vol. 41, pp. 265, 1950.

Kocks 98 U. F. Kocks, C. Tome and and H. R. Wenk, Texture Anisotropy: Preferred Orientation in Polycrystals and Their Effects on Material Properties, Cambridge University Press, 1998.

Kouddane 94 R. Kouddane, N. Zouhal and A. Molinari, Complex Loading of Viscoplastic Materials: Micro-Macro Modelling, Mat. Sci. Eng. A, Vol. 175, pp. 31, 1994.

Kouris 89 D. A. Kouris and T. Mura, The elastic field of a hemispherical inhomogeneity at the free surface of an elastic half-space, J. Mech. Phys. Solids, Vol. 37, pp. 365-379, 1989.

Kreher 93 W. Kreher and A. Molinari, Residual stresses in polycrystals as influenced by grain shape and texture, J. Mech. Phy. Solids, Vol. 41, pp. 1955-1977, 1993.

Krempl 74 E. Krempl, The influence of state of stress on low-cycle fatigue of structural materials: a literature survey and interpretive report, ASTM STP, Vol. 549, 1974.

Kröner 61 E. Kröner, Zur plastischen verformung des vielkristalls, Acta Metall, Vol. 9, pp. 155, 1961.

Kruml 97 T. Kruml, J. Polàk, K. Obrtlìk and S. Degallaix, Dislocation structures in the bands of localized cyclic plastic strain in austenitic 316L and austenitic-ferritic duplex stainless steels, Acta Materiala, Vol. 45, pp. 5145-5151, 1997.

Krupp 07 U. Krupp, Fatigue Crack Propagation in Metals and Alloys: Microstructural Aspects and Modelling Concepts, WILEY-VCH Verlag GmbH & Co. KGaA, 2007.

Kuroda 06 M. Kuroda and V. Tvergaard, Studies of scale dependent crystal viscoplasticity models, J. Mech. Phys. Solids, Vol. 54, pp. 1789-1810, 2006.

Lagaros 05 N. D. Lagaros, V. Plevris and M. Papadrakakis, Multi-objective design optimization using cascade evolutionary computations, Computer Methods in Applied Mechanics and Engineering, Structural and Design Optimization, Vol. 194, pp. 3496-3515, 2005.

Lagattu 04 F. Lagattu, J. Brillaud and M. Lafarie-Frenot, High strain gradient measurements by using digital image correlation technique, Materials Characterization, Vol. 53, pp. 17-28, 2004.

Lagoda 01 T. Lagoda, Energy models for fatigue life estimation under uniaxial random loading. Part I: The model elaboration, Int. J. Fatigue, Vol. 23, pp. 467-80, 2001.

Lai 93 M. O. Lai, J. T. Oh and A. Y. C. Nee, Fatigue properties of holes with residual stresses, Eng. Fract. Mech., Vol. 45, pp. 551-557, 1993.

Laird 86 C. Laird, P. Charsley and H. Mughrabi, Mater. Sci. Eng., Vol. 81, pp. 433, 1986.

Laird 96 C. Laird, Fatigue, In: Phys. Metall. (4th ed., R.W. Cahn and P. Haasen eds.), Vol. 3, Elsevier Science, pp. 2293, 1996.

Lange 53 H. Lange and K. Lucke, Störungen der Gleitung bei Aluminiumeinkristallen, Z. Metallk. Vol. 44, pp. 183, 1953.

Laufer 64 E. E. Laufer and W. N. Roberts, Phil. Mag., Vol. 10, pp. 883, 1964.

Laufer 66 E. E. Laufer and W. N. Roberts, Phil. Mag., Vol. 14, pp. 65, 1966.

Lebensohn 04 R. A. Lebensohn, C. N. Tome and P. J. Maudlin, A selfconsistent formulation for the prediction of the anisotropic behavior of viscoplastic polycrystals with voids, J. Mech. Phys. Solids, Vol. 52, pp. 249-278, 2004.

Lee 89 S. Lee and C. C. Hsu, Thermoelastic stress due to surface parallelepiped inclusions, J. Appl. Mech., Vol. 52, pp. 225-228, 1989.

Lee 92 M. Lee, I. Jasiuk and E. Tsuchida, The sliding circular inclusion in an elastic half-plane, J. Appl. Mech., Vol. 59, pp. 57-64, 1992.

Leese 81 G. E. Leese and J. Morrow, Low cycle fatigue properties of a 1045 steel in torsion, In: Multiaxial Fatigue, ASTM STP, Vol. 83, pp. 482-489, 1981.

Lemaitre 88 J. Lemaitre and J.L. Chaboche, Mecanique des materiaux solides, Dunod, Bordas, 1988.

Li 01 X. W. Li, Z. F. Zhang, Z. G. Wang, S. X. Li and Y. Umakoshi, SEM-ECC investigation of dislocation arrangements in cyclically deformed copper single crystals with different crystallographic orientations, Diffusion and Defect Data, Pt A Defect and Diffusion Forum, Vol. 188-190, pp. 153-170, 2001.

Li 99a X. W. Li, Z. G. Wang and S. X. Li, Cyclic deformation behavior of double-slip-oriented copper single crystals I: coplanar double slip orientation on 011-111 side of the stereographic triangle, Mater. Sci. Eng. A, Vol. 260, pp. 132-138, 1999.

Li 99b X. W. Li, Z. G. Wang and S. X. Li, Survey of plateau behaviour in the cyclic stress-strain curve of copper single crystals, Philos. Mag. Lett., Vol. 79, pp. 715-719, 1999.

Lim 05 J. -Y. Lim, S. -G. Hong, S. -B. Lee, Application of local stress-strain approaches in the prediction of fatigue crack initiation life for cyclically non-stabilized and non-Masing steel, Int. J. Fatigue, Vol. 27, pp. 1653-1660, 2005.

Lin 57 T. H. Lin, Analysis of elastic and plastic strains of facecentered cubic crystals, J. Mech. Phys. Solids, Vol. 5, pp. 143, 1957.

Lindroos 71 V.K. Lindroos, Phil. Mag., Vol. 24, pp. 709, 1971.

Lindstedt 98 U. Lindstedt, B. Karlsson and M. Nyström, Small fatigue cracks in an austenitic stainless steel, Fatigue Fract. Engng. Mater. Struct., Vol. 21, pp. 85-98, 1998.

Liu 03 J. Liu and H. Zenner, Fatigue limit of ductile metals under multiaxial loading. In: Biaxial/multiaxial fatigue and fracture, Elsevier, pp. 147-63, 2003.

Lukáš 01 P. Lukáš, Fatigue crack initiation mechanisms, In: Encyclopedia of Materials: Science and Technology (K. H. J. Buschow, R. W. Cahn, M. C. Flemings, B. Ilschner, E. J. Kramer and S. Mahajan eds.), Vol. 3, Elsevier Science, pp. 2884, 2001.

Lukáš 04 P. Lukáš and L. Kunz, Phil. Mag, Vol. 84, pp. 317, 2004.

Lukáš 68 P. Lukáš, M. Klesnil and J. Krejčí, Phys. Status Solidi, Vol. 27, pp. 545, 1968.

Lukáš 96 P. Lukáš, Fatigue Crack Nucleation and Microstructure, ASM Handbook: Fatigue and Fracture, Vol. 19, pp. 96-109, 1996.

Lynn 02 A. K. Lynn and D. L. DuQuesnay, Computer simulation of variable amplitude fatigue crack initiation behaviour using a new strain-based cumulative damage model, International Journal of Fatigue, Vol. 24, pp. 977-986, 2002.

Ma 87 B. -T. Ma, Strain Localization and Short Crack Growth Kinetics under Variable Loads: The Physical Basis of Damage Summation in Cyclic Deformation, Dissertation, University of Pennsylvania, 1987.

Ma 89 B. -T. Ma and C. Laird, Overview of fatigue behavior in copper single crystals - II. Population, size, distribution and growth kinetics of stage I cracks for tests at constant strain amplitude, Acta Metall., Vol. 37, pp. 337-48, 1989.

Macha 99 E. Macha and C. M. Sonsino, Energy criteria of multiaxial fatigue failure, Fatigue Fract. Eng. Mater. Struct., Vol. 22, pp. 1053-1070, 1999.

Madec 01 R. Madec, Des intersections entre dislocations à la plasticité du monocristal CFC : Etude par dynamyque des dislocations, PhD thesis, Université Paris XI Orsay, 2001.

Magnin 84 T. Magnin, J. Driver, J. Lepinoux and L. Kubin, Aspects microstructuraux de la déformation cyclique dans les métaux et alliages C.C. et C.F.C I. - consolidation cyclique, Physique Appliquée, Vol. 19, pp. 467-482, 1984.

Man 02 J. Man, K. Obrtlík, C. Blochwitz and J. Polák, Atomic force microscopy of surface relief in individual grains of fatigued 316L austenitic stainless steel, Acta Mater., Vol. 50, pp. 3767-3780, 2002.

Man 09 J. Man, K. Obrtlík and J. Polák, Extrusions and intrusions in fatigued metals. Part 1. State of the art and history, Philos. Mag., Vol. 89, pp. 1295-1336, 2009.

Manole 10 C. Manole, Analyse des contraintes internes dans les monocristaux CFC : vers une nouvelle loi de plasticité cristalline, PhD thesis, Université de Savoie, 2010.

Manonukul 04 A. Manonukul and F. P. E. Dunne, High- and low-cycle fatigue crack initiation using polycrystal plasticity, Proc. R. Soc. Lond. A, Vol. 460, pp. 1881-1903, 2004.

Manson 53 S. S. Manson, Behavior of materials under conditions of thermal stress, NACA TN-2933, 1953.

Marchionni 96 M. Marchionni and D. J. Boerman, Low cycle fatigue properties of a reduced activation Cr-Mn austenitic stainless steel, J. Nucl. Mater., Vol. 228, pp. 129-134, 1996.

Masumura 82 R. A. Masumura and Y. T. Chou, Antiplane eigenstrain problem of an elliptic inclusion in an anisotropic half plane, J. Appl. Mech., Vol. 49, pp. 52-54, 1982.

Mateo 96 A. Mateo, L. Llanes, L. Iturgoyen and M. Anglada, Cyclic stress-strain response and dislocation substructure evolution of a ferrite-austenite stainless steel, Acta Materiala, Vol. 44, pp. 1143-1153, 1996.

McDiarmid 90 D. L. McDiarmid, A general criterion for high cycle multiaxial fatigue failure, Fatigue Fract. Eng. Mater. Struct., Vol. 14, pp. 429-53, 1990.

McDowell 92 D. L. McDowell and J. Berard, A DJ-based approach to biaxial fatigue, Fatigue Fract. Eng. Mater. Struct., Vol. 15, pp. 719-741, 1992.

Mecking 70 H. Mecking and K. Lucke, A new aspect of the theory of flow stress of metals, Scripta Met., Vol. 4, pp. 427-432, 1970.

Melmed 96 A. J. Melmed, Recollections of Erwin Muller's laboratory: the development of FIM (1951-1956), Applied Surface Science, Vol. 94-95, pp. 17-25, 1996.

Miller 73 M. W. Brown and K. J. Miller, A theory for fatigue failure under multiaxial stress-strain conditions, Proc. Inst Mech. Engrs, Vol. 187, pp. 65-73, 1973.

Miller 97 K. J. Miller, The Three Thresholds for Fatigue Crack Propagation, Fatigue Fract. Mech., Vol. 27, pp. 267-286, 1997.

Mineur 00a M. Mineur, Condition Locales d'amorçage des fissures de fatigue dans un acier inoxydable de type 316L : aspects crystallographiques (EBSD), PhD thesis, Université de Poitiers, 2000.

Mineur 00b M. Mineur, P. Villechaise and J. Mendez, Influence of the crystalline texture on the fatigue behavior of a 316L austenitic stainless steel, Mater. Sci. Eng. A, Vol. 286, pp. 257-268. 2000.

Molinari 87 A. Molinari, R. G. Canova, S. Ahzi, A self-consistent approach to the large deformation polycrystal viscoplasticity, Acta Metall., Vol. 35, pp. 2983, 1987.

Molinari 97 A. Molinari, S. Ahzi and R. Kouddane, On the self-consistent modeling of elastic-plastic behavior of polycrystals, Mechanics of Materials, Vol. 26, pp. 43-62, 1997.

Moulart 09 R. Moulart, R. Rotinat and F. Pierron, Full-field evaluation of the onset of microplasticity in a steel specimen, Mechanics of Materials, Vol. 41, pp. 1207-1222, 2009.

Moussavi 97 S. E. Moussavi Torshizi, Ecrouissage cyclique d'aciers inoxydables austénitique, ferritique et austéno-ferritique: influence de l'histoire du chargement, PhD thesis, Ecole Centrale de Lille, 1997.

Mowbray 73 D. F. Mowbray and J. E. McConnelee, ASTM STP, Vol. 519, pp. 151, 1973.

Mroz 67 Z. Mroz, On the description of anisotropic work hardening, J. Mech. Phys. Sol., Vol. 15, pp. 163-175, 1967.

Mughrabi 01 H. Mughrabi, Cyclic strain localization in fatigued metals, In: Physical Aspects of Fracture (E. Bouchaud, D. Jeulin, C. Prioul and S. Roux eds.), Vol. II/32, Kluwer Academic, Dordrecht, pp. 271, 2001.

Mughrabi 06 H. Mughrabi, Specific features and mechanisms of fatigue in the ultrahigh-cycle regime, Int. J. Fatigue, Vol. 28, pp. 1501-1508, 2006.

Mughrabi 78 H. Mughrabi, The cyclic hardening and saturation behaviour of copper single crystals, Mater. Sci. Eng., Vol. 33, pp. 207-223, 1978.

Mughrabi 83 H. Mughrabi, R. Wang, K. Differt, Fatigue crack initiation by cyclic slip irreversibilities in high-cycle fatigue, In: Fatigue mechanisms, ASTM STP 811, pp. 5-45, 1983.

Mughrabi 99 H. Mughrabi, On the life-controlling microstructural fatigue mechanisms in ductile metals and alloys in the gigacycle regime, Fatigue and Failure of Engineering Materials and Structures, Vol. 22 , pp. 633-641, 1999.

Mura 87 T. Mura, Micromechanics of Defects in Solids (2nd ed.), MARTINUS NIJHHOFF PUBLISHERS, 1987.

Mura 94 T.Mura, A theory of fatigue crack initiation, Mater. Sci. Eng. A, Vol. 176, pp. 61-70, 1994.

Nabarro 64 F. R. N. Nabarro, Z. S. Basinski and D. B. Holt, The Plasticity of Pure Single Crystals, Advances in Physics, Vol. 13, pp. 193, 1964.

Nemat-Nasser 86 S. Nemat-Nasser and M. Obata, Rate-dependent, finite elastoplastic deformation of polycrystals, Proceedings of the Royal Society of London A, Vol. 407, pp. 343-375, 1986.

Obrtlík 94 K. Obrtlík, T. Kruml and J. Polák, Dislocation structures in 316L stainless steel cycled with plastic strain amplitudes over a wide interval, Mater. Sci. Eng. A, Vol. 187, pp. 1-9, 1994,

Osterstock 08 S. Osterstock, Vers la prédiction de l'apparition de réseaux de fissures : influence des paramètres microstructuraux sur la dispersion à l'amorçage, Phd thesis, Ecole Centrale de Lille, 2008.

Papadopoulos 01 I. V. Papadopoulos, Long life fatigue under multiaxial loading, Int. J. Fatigue, Vol. 23, pp. 839-849, 2001.

Papadopoulos 95 I. V. Papadopoulos, A high-cycle criterion applied in biaxial and triaxial out-of-phase stress conditions, Fatigue Fract. Eng. Mater. Struct., Vol. 18, pp. 79-91, 1995.

Paquin 01 A. Paquin, S. Berbenni, V. Favier, X. Lemoine and M. Berveiller, Micromechanical modeling of the elastic-viscoplastic behavior of polycrystalline steels, Int. J. Plast., Vol. 17, pp. 1267-1302. 2001.

Paris 63 P. Paris and F. Erdogan, A critical analysis of crack propagation laws, Trans. Am. Soc. Mech. Engrs., Vol. 1, pp. 528-534, 1963.

Peirce 83 D. Peirce, R. J. Asaro and A. Needleman, Material rate dependence and localized deformation in crystalline solids, Acta Metall., Vol. 31, pp. 1951-1976, 1983.

Petch 53 N. Petch, The cleavage strength of polycrystals, J. Iron Steel Inst., Vol. 174, pp. 25-28, 1953.

Peters 82 W. H. Peters and W. F. Ranson, Digital imaging techniques in experimental stress analysis, Optical Engineering, Vol. 21, pp. 427-431, 1982.

Phillips 62 W. L. Phillips, Aluminum and copper tested in direct shear, Trans. Metall. Soc. of AIME, Vol. 224, pp. 845, 1962.

Pilvin 90 P. Pilvin, Approches multiéchelles pour la prévision du comportement anélastique des métaux. PhD thesis, Université Pierre et Marie Curie, 1990.

Pilvin 97 P. Pilvin, Une approche simplifiée pour schématiser l'effet de surface sur le comportement mécanique d'un polycristal, 40ème colloque de métallurgie de l'INSTN, 1997.

Pokluda 94 J. Pokluda, F. Kroupa, L. Obdrzalek, Mechanical properties and structure of solids, PCdir, 1994.

Polák 03 J. Polák, Cyclic deformation, crack initiation, and low-cycle fatigue, In: Comprehensive Structural Integrity (I. Milne, R. O. Ritchie and B. Karihallo eds.), Elsevier, Vol. 4, pp. 1, 2003.

Pook 07 L. Pook, Metal Fatigue - What It is , Why It Matters, Springer, 2007.

Prasad Reddy 08 G. V. Prasad Reddy, R. Sandhya, M. Valsan and K. Bhanu Sankara Rao, High temperature low cycle fatigue properties of 316(N) weld metal and 316L(N)/316(N) weld joints, Int. J. Fatigue, Vol. 30, pp. 538-546, 2008.

Provan 91 J. W. Provan and Z.B. Zhai, Fatigue crack initiation and stage-I propagation in polycrystalline materials. II: Modelling, Int. J. Fatigue, Vol. 13, pp. 110-116, 1991.

Pyrz 07 M. Pyrz and F. Zairi, Identification of viscoplastic parameters of phenomenological constitutive equations for polymers by deterministic and evolutionary approach, Modelling and Simulation in Materials Sciences and Engineering, Vol. 15, pp. 85-103, 2007.

Qu 05 J. Qu, Q. L. Jin and B. Y. Xu, Parameter identification for improved viscoplastic model considering dynamic recrystallization, Int. J. Plast., Vol. 21, 1267-1302, 2005.

Raabe 03 D. Raabe, M. Sachtleber, H. Weiland, G. Scheele and Z. Zhao, Grain-scale micromechanics of polycrystal surfaces during plastic straining, Acta Mater., Vol. 51, pp. 1539-1560, 2003.

Radi 09 M. Radi and A. Abdul-Latif, Grain shape effect on the biaxial elastic-inelastic behavior of polycrystals with a self-consistent approach, Proc. Eng., Vol. 1, pp. 13-16, 2009.

Rauch 93 E. F. Rauch and S. Thuillier, Plasticity and unstable flow mild steel, Archives of Metallurgy, Vol. 38, pp. 167-177, 1993.

Ray 71 I. L. F. Ray and D. J. H. Cockayne, Proc. Roy. Soc., Vol. A325, pp. 543, 1971.

Rice 71 J. R. Rice, Inelastic constitutive relations for solids: An internal-variable theory and its application to metal plasticity, J. Mech. Phys. Solids, Vol. 19, pp. 433, 1971.

Robert 89 J. Robert and W. Catherine, Holographic and Speckle Interferometry, Cambridge University Press, 1989.

Roux 09 S. Roux, J. Réthoré and F. Hild, Digital image correlation and fracture: an advanced technique for estimating stress intensity factors of 2D and 3D cracks, J. Phys. D: Appl. Phys., Vol. 42, pp. 214004, 2009.

Saai 10 A. Saai, H. Louche, L. Tabourot and H. J. Chang, Experimental and numerical study of the thermo-mechanical behavior of Al bi-crystal in tension using full field measurements and micromechanical modeling, Mech. Mater., Vol. 42, pp. 275-292, 2010.

Sachs 28 G. Sachs, Plasticity problems in metals, Z. Ver. Dent. Ing., Vol. 72, pp. 734, 1928.

Sangid 11 M. D. Sangid, H. J. Maier, H. Sehitoglu, A physically based fatigue model for prediction of crack initiation from persistent slip bands in polycrystals, Acta Mater., Vol. 59, 328-341, 2011.

Sauzay 00a M. Sauzay, Effets de surface et d'anisotropie en fatigue multiaxiale, PhD thesis, University Paris 06, 2000.

Sauzay 00b M. Sauzay and P. Gilormini, Surface and cyclic microplasticity, Fatigue Fract. Eng. Mater. Struct., Vol. 23, pp. 573-579.

Sauzay 00c M. Sauzay and P. Gilormini, Inclusion élastoplastique en surface, C.R. Acad. Sci. Paris, Vol. 328, pp. 117-122, 2000.

Sauzay 99a M. Sauzay and P. Gilormini, Surface effect, fatigue and microplasticity, In: Fourth International Conference on Constitutive Laws in Engineering Materials (R. C. Picu and E. Krempl eds.), Rensselaer Polytechnic Institute, pp. 98-101, 1999.

Sauzay 99b M. Sauzay, J. Lemaitre and R. Desmorat, Une prise en compte de l'effet de surface en fatigue polycyclique, 14ème Congrès Français de Mécanique (Toulouse), 1999.

Schaeffler 49 A. L. Schaeffler, Constitution diagram for stainless steel weld metal, Metal Progress, Vol. 56, pp. 680-680B, 1949.

Schijve 09 J. Schijve, Fatigue of structures and materials (2nd ed.), Springer, 2009.

Schmid 50 E. Schmid and W. Boas, Plasticity of crystals, Hughes, 1950.

Schroeter 03 B. M. Schroeter and D. L. McDowell, Measurement of deformation fields in polycrystalline OFHC copper, Int. J. Plast., Vol. 19, pp. 1355-1376, 2003.

Schwartz 10 J. Schwartz, O. Fandeur and C. Rey, Fatigue crack initiation modeling of 316LN steel based on non local plasticity theory, Procedia Engineering, Vol. 2, pp. 1352-1362, 2010.

Shu 99 J. Y. Shu and N. A. Fleck, Strain gradient crystal plasticity: size-dependent deformation of bicrystals, J. Mech. Phys. Solids, Vol. 47, pp. 297-324, 1999.

Sines 55 G. Sines, Failure of materials under combined repeated stresses with superimposed static stresses, Tech. Rep. Technical note 3495, Nat. Adv. Coun. Aeronaut. (USA), 1955.

Socie 93 D. Socie, Critical plane approaches for multiaxial fatigue damage assessment, In: Advance in multiaxial fatigue (D. L. McDowell and R. Ellis eds.), ASTM STP, Vol. 1191, pp. 7-36, 1993.

Stanzl-Tschegg 07 S. Stanzl-Tschegg, H. Mughrabi and B. Schoenbauer, Life time and cyclic slip of copper in the VHCF regime, Int. J. Fatigue, Vol. 29, pp. 2050-2059, 2007.

Suresh 98 S. Suresh, Fatigue of Materials (2nd ed.), Cambridge University Press, 1998.

Surrel 04 Y. Surrel, Les techniques optiques de mesure de champ: essai de classification, Instrumentation Mesure Métrologie RS série I2M, Vol. 4, pp. 11-42, 2004.

Tabourot 01 L. Tabourot, Vers une vision unifiée de la plasticité cristalline, Habilitation à diriger les recherches, Université de Savoie, 2001.

Tabourot 97 L. Tabourot, M. Fivel and E. Rauch, Generalised constitutive laws for FCC single crystals, Mat. Sci. Eng. A, Vol. 234-236, pp. 639-642, 1997.

Tanaka 81 K. Tanaka and T. Mura, A dislocation model for fatigue crack initiation, J. Appl. Mech., Vol. 48, pp. 97-103, 1981.

Tanaka 94 E. Tanaka, A nonproportionality parameter and a viscoplastic constitutive model taking into account amplitude dependences and memory effects of isotropic hardening, Eur. J. Mech. A/Solids, Vol. 13, pp. 155-173, 1994.

Tao 05 G. Tao and Z. Xia, A non-contact real-time strain measurement and control system for multiaxial cyclic/fatigue tests of polymer materials by digital image correlation method, Polym. Test., Vol. 24, pp. 844-855, 2005.

Taylor 38 G. I. Taylor, Plastic strain in metals, J. Inst. Metals, Vol. 62, pp. 307, 1938.

Thompson 56 N. Thompson, N. Wadsworth and N. Louat, Xi. The Origin of Fatigue Fracture in Copper, Philos. Mag., Vol. 1, pp. 113-126, 1956.

Tiem 86 S. Tiem, M. Berveiller and G.R. Canova, Grain shape effects on the slip system activity and on the lattice rotations, Acta Metall., Vol. 34, pp. 2139-2149, 1986.

Underwood 95 J. H. Underwood, Residual-stress effects at a notch root in A723 steel to extend fatigue life, Exp. Mech., Vol. 35, pp. 61-65, 1995.

Vallellano 00a C. Vallellano, A. Navarro and J. Domínguez, Fatigue Crack Growth Threshold Conditions at Notches: I. Theory, Fatigue Fract. Eng. Mater. Struct., Vol. 23, pp. 113-121, 2000.

Vallellano 00b C. Vallellano, A. Navarro and J. Domínguez, Fatigue Crack Growth Threshold Conditions at Notches: II. Generalization and Application to Experimental Results, Fatigue Fract. Eng. Mater. Struct., Vol. 23, pp. 123-128, 2000.

Varvani-Farahani 00 A. Varvani-Farahani, A new energy-critical plane parameter for fatigue life assessment of various metallic materials subjected to inphase and out-of-phase multiaxial fatigue loading conditions, Int. J. Fatigue, Vol. 22, pp. 295-305, 2000.

Vogel 53 F. L. Vogel, W.G. Pfann, H. E. Corey and E. E. Thomas, Observations of Dislocations in Lineage Boundaries in Germanium, Physical Review, Vol. 90, pp. 489, 1953.

Vogt 84 J. B. Vogt, S. Degallaix and J. Foct, Low cycle fatigue life enhancement of 316 L stainless steel by nitrogen alloying, Int. J. Fatigue, Vol. 6, pp. 211-215, 1984.

Wareing 79 J. Wareing and H.G. Vaughan, Influence of surface finish on low-cycle fatigue characteristics of type 316 stainless steel at 400°C, Metal Sci., Vol. 13, pp. 1-7, 1979.

Weng 82 G. J. Weng, A unified self-consistent theory for the plastic-creep deformation of metals, J. Appl. Mech., Vol. 49, pp. 728, 1982.

Wu 91 H. C. Wu and W. C. Yeh, On the experimental determination of yield surfaces and some results of annealed 304 stainless steel, Int. J. Plast., Vol. 7, pp. 803-826, 1991.

Xie 02 J. Xie, A. T. Alpas and D. O. Northwood, A mechanism for the crack initiation of corrosion fatigue of Type 316L stainless steel in Hank's solution, Mater. Charact., Vol. 48, pp. 271-277, 2002.

Yamaguchi 81 I. Yamaguchi, A laser-speckle strain-gauge, Journal of Physics E: Scientific Instruments, Vol. 14, pp. 1270-1273, 1981.

Yang 04 X. J. Yang, A viscoplastic model for 316L stainless steel under uniaxial cyclic straining and stressing at room temperature, Mech. Mater., Vol. 36, pp. 1073-1086, 2004.

Zeghadi 07 A. Zeghadi, S. Forest, A. -F. Gourgues and O. Bouaziz, Ensemble averaging stress-strain fields in polycrystalline aggregates with a constrained surface microstructure - Part 2: crystal plasticity, Philos. Mag., Vol. 87, pp. 1425-1446, 2007.

Zhang 03 L. Zhang, G. Wang, J. Cheng and L. Jiang, Investigation of the low-cycle fatigue life under multi-axial non-proportional loading, Mater. Sci. Eng., Vol. 355, pp. 18-23, 2003.

Zong 90 C. Zong, N. Y. Jin, X. Zhou, E. Meng and X. F. Chen, Cyclic deformation of AISI-310 stainless steel I. Cyclic stress-strain responses, Acta Metallurgica Materialia, Vol. 38, pp. 2135-2140, 1990.

RESUME ETENDU

INTRODUCTION GENERALE

Afin de dimensionner au plus juste, il est nécessaire de connaître le mieux possible le comportement des structures à la fatigue. Beaucoup de modèles existent dans la littérature pour prédire la durée de vie sous chargement cyclique mais ils sont en général basés sur des observations macroscopiques et ne peuvent pas être reliés directement aux propriétés de la microstructure. Ils ne permettent donc pas de privilégier telle ou telle caractéristique de la microstructure vis-à-vis de la durée de vie en fatigue. La présente étude a pour objectif l'établissement d'un critère d'amorçage en fatigue en lien avec la microstructure du matériau. Une approche à champ moyen a été utilisée afin de simuler facilement la sollicitation cyclique supportée par le matériau polycristallin considéré, ici un acier inoxydable austénitique AISI 316L. Les grains sont alors considérés comme entourés par le milieu homogène équivalent. Comme l'amorçage se produit en surface en fatigue, une loi de localisation spécifique a été établie pour prendre en compte le fait que les grains de surface se déforment plus, étant moins contraints par leurs voisins. Une fois ce cadre numérique établi, différents critères d'amorçage ont été discriminés sur une même base expérimentale. La surface d'une éprouvette soumise à une sollicitation de fatigue oligocyclique a alors été observée afin de caractériser les paramètres cristallographiques influençant l'amorçage, l'étude s'est focalisée sur l'amorçage intragranulaire car le cadre de l'approche à champs moyen ne permet pas de prendre en compte l'influence des grains voisins.

I. INTRODUCTION A LA FATIGUE ET A L'AMORÇAGE DE FISSURE

Le premier chapitre présente tout d'abord les notions de durée de vie et de courbe de Wöhler, puis les familles d'aciers inoxydables ainsi que le comportement mécanique sous sollicitation cyclique. L'effet Bauschinger et le durcissement/adoucissement cyclique observés dans les aciers inoxydables austénitiques sont notamment rappelés. Le rôle du taux d'azote dans la durée de vie en fatigue oligocyclique est notamment souligné.

Le paragraphe suivant présente le comportement plastique intragranulaire. Plusieurs sources d'hétérogénéité dans l'état des contraintes et des déformations intragranulaires sont détaillées. A

cause de l'anisotropie de l'élasticité cristalline, suivant les directions sollicitées, le rapport des déformations maximale et minimale peut atteindre un rapport 3 dans l'austénite [Huntington 58]. Cependant, bien que l'anisotropie d'élasticité cristalline ait une grande influence en fatigue à grand nombre de cycles, son influence est négligeable à plus haut niveau de déformation, ainsi qu'il a été montré par [Osterstock 08]. Comme la déformation plastique se développe par glissement sur un nombre fini de plans, le comportement plastique d'un grain dépend largement de son orientation et peut être prédite par sa position dans le triangle standard. Ces observations ont été effectuées sur des monocristaux sollicités d'une part en traction monotone [Mughrabi 78] mais aussi en traction-compression cyclique [Li 99a]. Par ailleurs, des grains de différentes formes et différentes tailles n'auront pas le même niveau de contrainte. En effet, les joints de grain s'opposant au mouvement des dislocations, les dislocations s'accumulent près des joints et créent alors des concentrations de contrainte. De plus, la densité de dislocations géométriquement nécessaires pour prendre en compte les incompatibilités de déformation entre grains modifie également l'écrouissage du cristal.

Sous sollicitation cyclique, le glissement plastique crée un relief à la surface, dont l'irréversibilité est accentuée par les effets d'environnement. Au cours des cycles, la déformation plastique se localise en bandes de glissement persistantes (BGP). Ces bandes de glissement persistantes sont classiquement caractérisées par une structure de dislocations en échelle et laissent une marque de glissement persistante à la surface. Par le relief d'extrusion-intrusion que ces bandes créent sur la surface libre, elles sont un lieu privilégié d'amorçage des fissures [Ma 87]. Ce n'est cependant pas le seul, puisque des fissures peuvent également s'initier au joint de grain ou au joint de macle [Mineur 00]. La localisation de l'amorçage dépend fortement du niveau de déformation [Kim 78a, b] [Figuera 83] [Heinz 92]. Après initiation, les fissures se propagent d'abord à la surface puis dans le volume. La propagation est d'abord gouvernée par les caractéristiques cristallographiques tant que 2 à 3 joints n'ont pas été franchis. La fissure s'oriente ensuite perpendiculairement à la plus grande contrainte principale et sa propagation peut être décrite par une loi de type Paris.

II. CARACTERISATION MECANIQUE DE L'ACIER ETUDIE

Les travaux présentés dans ce travail reposent sur l'analyse d'un acier inoxydable austénitique Z2CND17-12. La composition chimique massique est donnée dans le TAB. II.1. Le matériau a une microstructure globalement isotrope, avec des grains équiaxes de taille moyenne 50 µm.

Des essais de traction monotone et de traction-compression cyclique à plusieurs amplitudes de déformation imposée ont été réalisés sur une machine d'essais hydraulique afin de caractériser le comportement mécanique du matériau étudié. Les résultats montrent le comportement de durcissement/adoucissement cyclique habituellement observé dans les aciers inoxydables austénitiques à température ambiante. Par ailleurs, le cyclage induit un léger adoucissement cyclique par rapport à la traction monotone en-dessous de 0.5 % d'amplitude de déformation imposée et un léger durcissement cyclique à 0.8 % d'amplitude de déformation imposée. L'effet Bauschinger est très prononcé sur ce matériau, ce qui laisse présager un fort écrouissage cinématique. Ce résultat est en accord avec la littérature [Choteau 99]. Enfin, le module d'élasticité a été mesuré en post-traitement par une procédure automatique lors de chaque traversée du domaine d'élasticité des essais cycliques. Les valeurs mesurées varient entre 165 et 185 GPa, montrant la grande sensibilité de la mesure du module d'élasticité aux conditions expérimentales. Pour chaque condition d'essai, le module est stable pendant la majeure partie de l'essai, indiquant l'absence d'endommagement macroscopique.

III. MODELISATION DU COMPORTEMENT MECANIQUE

Plusieurs approches sont possibles pour modéliser le comportement mécanique de l'acier inoxydable austénitique étudié en fatigue oligocyclique. L'approche choisie devait à la fois utiliser une description physique des mécanismes de la déformation plastique et permettre la simulation de plusieurs centaines voire milliers de cycles. Pour ces deux raisons, nous avons choisi une approche multiéchelles qui consiste en la détermination du comportement du milieu homogène équivalent au volume élémentaire représentatif du matériau. L'échelle d'hétérogénéité à considérer ici est le grain, un modèle autocohérent à un site est donc tout à fait adapté. La morphologie des grains est à peu près équiaxe. De plus, le matériau est faiblement texturé (FIG. III.3), le volume élémentaire représentatif pourra donc être constitué d'une distribution isotrope d'orientations cristallines avec des grains sphériques.

Les modèles de transition d'échelle sont caractérisés par loi de localisation, qui permet de déterminer l'état des contraintes dans un grain ou une inclusion connaissant l'état des contraintes macroscopique. Le schéma autocohérent, dans le cas de l'élasticité linéaire, consiste à plonger chaque grain dans une matrice correspondant au milieu homogène équivalent recherché. N problèmes d'Eshelby sont alors résolus. Afin de pouvoir simuler des comportements non-linéaires,

plusieurs lois de localisation ont été introduites, peu d'entre elles permettent cependant de simuler des chargements cycliques. La loi de localisation proposée par Cailletaud et Pilvin a été choisie dans cette étude pour sa capacité à simuler des chargements complexes et pour son temps de simulation réduit [Evrard 08].

La formulation de la loi de comportement locale nécessite de connaître les systèmes de glissement présents au sein du matériau et de postuler une loi de comportement à leur échelle. Les systèmes de glissement des structures cubiques face centrée sont composés de 4 plans de glissement de type {111} possédant chacun 3 directions de glissement de type <110>. Afin de faciliter l'écriture du critère d'écoulement en cas de glissement multiple, une formulation de type viscoplastique a été choisie pour la loi d'écoulement (Eq III.8) [Tabourot 01]. La cission critique est reliée aux densités de dislocations présentes sur les différents systèmes de glissement par l'intermédiaire d'une matrice d'interaction (modèle des arbres de la forêt).

Le modèle présenté ci-dessus nécessite 12 paramètres matériau (TAB. III.2). Certains de ces paramètres ont été mesurés (module d'élasticité E, diamètre des grains relié à un paramètre L contrôlant la production de dislocations), d'autres sont issus de la littérature (vecteur de Burgers b, densité initiale de dislocations ρ_0, paramètres de viscosité K et n, coefficient de Poisson ν). Les 5 paramètres restants ont été identifiés par méthode inverse en comparant les résultats expérimentaux des 5 premiers cycles de l'essai de fatigue à 0.5% d'amplitude à la simulation. L'optimisation est réalisée à l'aide d'un algorithme génétique. Les simulations sont en bon accord avec les observations expérimentales.

La loi de localisation de Cailletaud-Pilvin ne vérifie pas la condition d'auto-cohérence par construction. Il est donc nécessaire de mettre en œuvre des procédures spécifiques pour cela. Afin de vérifier la condition d'auto-cohérence au moins sur les trajets radiaux, il est préconisé d'identifier les paramètres du modèle en deux étapes en utilisant la loi de localisation de Berveiller-Zaoui pour la première étape [Evrard 08] mais cela n'a pas été possible. Nous avons donc quantifié l'erreur dans la relation d'auto-cohérence pendant les premiers 192 cycles. L'erreur commise est extrêmement faible, la condition peut donc être considérée comme vérifiée.

IV. ANALYSE EXPERIMENTALE DE L'AMORÇAGE

Afin d'observer et d'analyser l'endommagement en fatigue, un essai de fatigue d'amplitude 0.5 % a été réalisé sur une éprouvette plate polie. L'essai a été interrompu tous les 100 ou 200 cycles afin de

permettre l'observation de la surface de l'éprouvette à l'aide d'un dispositif de microscopie optique monté sur la machine d'essai. Un domaine de 8×6 images a été enregistré à chaque arrêt. Chaque image représente une zone de 140 μm $\times$ 70 μm, suffisamment grande pour voir plusieurs grains et suffisamment petite pour observer l'endommagement de surface. L'essai a été arrêté à 2000 cycles et un scan EBSD a été effectué sur une surface totale de 4.2 mm $\times$ 2 mm, afin d'avoir suffisamment de fissures pour une analyse statistique des caractéristiques cristallographiques de ces fissures (seules 3 fissures ont amorcé dans la zone suivie optiquement).

Les observations de la surface de l'éprouvette in situ ont permis de caractériser l'activité plastique pendant le cyclage. Après 300 cycles, 2/3 des grains montrent une activité plastique, environ 90 % après 2000 cycles. Les systèmes de glissement activés ont de plus été identifiés et analysés, la distribution des facteurs de Schmid des systèmes de glissement activés correspond bien à celle des facteurs de Schmid maximum calculés pour l'ensemble des grains des la zone étudiée, ce qui valide l'utilisation de ce paramètre comme critère de plasticité. Seuls quelques grains présentent deux systèmes de glissement activés. Les facteurs de Schmid de ces deux systèmes de glissement sont le plus souvent très élevés. En effet, à cause de la faible énergie de faute d'empilement du matériau, qui diminue d'autant plus que le taux d'azote augmente, le glissement dévié est difficile, plusieurs systèmes de glissement sont activés afin d'accommoder la déformation plastique.

Afin d'avoir des données statistiques importantes, les microfissures ont été recherchées dans une zone de 8.4 mm^2 dont les orientations cristallographiques étaient connues. La densité de fissures après 2000 cycles est de 12 fissures/mm^2. Ces fissures apparaissent majoritairement sur des marques de glissement (51.3 %) et aux joints de grains (42.5 %). Cette première catégorie de fissures a été ensuite analysée, afin de pouvoir ensuite discriminer des critères d'amorçage intragranulaires au chapitre suivant. Le système de glissement associé à chaque fissure amorcée sur une marque de glissement a été identifié, 3 paramètres ont été calculés : le facteur de Schmid μ par rapport à l'axe de chargement, l'angle entre la marque de glissement sur la surface et l'axe de chargement Π et l'angle entre la direction de glissement et la normale à la surface β. Les résultats montrent que les fissures apparaissent uniquement dans des grains orientés pour le glissement simple (μ>0.41) mais que ce n'est pas toujours le système le mieux orienté qui conduit à la fissure. Les distributions des angles Π et β sont quasi-symétriques respectivement autour des angles 60-70° et 50-60°. L'analyse des grains dans lesquels la fissure apparait sur un système de glissement mal orienté au sens du facteur de Schmid montre que dans ces grains, le système le mieux orienté au sens de μ fait un angle Π proche de 45° et un angle β proche de 80°. C'est-à-dire que ces grains sont de type A selon la terminologie de Miller [Miller 73], et qu'ils ont un faible volume débouchant [Després 04]. Ces grains

qui ont un système de glissement bien orienté vis-à-vis de la déformation plastique (μ_{max} élevé) mais pas d'un point de vue amorçage ont finalement amorcé sur un autre système de glissement moins bien orienté pour la déformation plastique.

Enfin, les images obtenues à l'aide du microscope in situ ont été utilisées pour déterminer le nombre de cycles à l'amorçage des fissures situées dans la zone observée en continu pendant l'essai. La technique de corrélation d'images numériques a été utilisée pour déterminer les champs de déplacement et de déformation entre deux images de la même zone obtenues à deux instants consécutifs du cyclage [Hild 06] [El Bartali 09]. La texture de niveaux de gris nécessaire à la corrélation d'image a été obtenue par une légère attaque chimique avant l'essai. La qualité des images a tout d'abord été évaluée en imposant des déplacements de corps rigides artificiels à une image extraite de la série à analyser. La sensibilité de l'incertitude du déplacement calculé à la taille de maille est du même ordre de grandeur que celle obtenue avec des mouchetis classiques à l'échelle macroscopique. Les images permettent d'effectuer des calculs de corrélation d'images numériques, bien que la texture ne soit pas vraiment visible. La taille de maille choisie est de 32×32 pixels, ce qui représente environ 4.4×4.4 μm^2. Les incertitudes en déplacement et en déformation sont alors respectivement de 0.0054 pixels et $1.2\ 10^{-4}$.

Deux fissures ont amorcé sur des marques de glissement dans la zone d'observation in situ. Les champs de déplacement et de déformation obtenus entre différents instants du cyclage autour de ces fissures montrent que la déformation est au départ relativement homogène par grain, avec une localisation aux joints de grains. Le champ de déformation s'homogénéise ensuite, puis présente des localisations de déformation dans la zone où la fissure A a amorcé entre 1400 et 1600 cycles (FIG. IV.33), ce qui tend à indiquer que l'amorçage de cette fissure s'est produit entre 1400 et 1600 cycles. Les calculs n'ayant pas abouti pour la seconde fissure, une conclusion similaire n'a pu être établie.

V. MODELISATION DE LA MICROPLASTICITE DE SURFACE ET DE L'AMORÇAGE

Les grains de surface, dans lesquels les fissures de fatigue s'amorcent, sont moins contraints par leurs voisins que les grains du volume, ce qui autorise des niveaux de déformation plus élevés dans ces grains que dans des grains du volume ayant la même orientation. De plus, ces plus grandes déformations favorisent l'amorçage de fissure. Les lois de localisation utilisées dans les modèles auto-cohérents ne permettent pas de décrire le comportement d'un grain en surface, une loi spécifique doit donc être établie.

Une étude bibliographique est présentée, montrant l'influence de la profondeur du grain et de son orientation ainsi que l'existence d'une singularité entre le grain et la matrice environnante. Nous nous sommes de plus appuyés sur l'étude réalisée par Sauzay, portant sur la réponse d'un grain de surface élastoplastique dans une matrice semi-infinie élastique [Sauzay 00a]. Afin de définir une loi de localisation permettant de rendre compte du comportement d'un grain élastoplastique dans une matrice élastoplastique en fatigue, une simulation par éléments finis a été réalisée. Un grain hémisphérique est placé à la surface d'une matrice de très grande taille par rapport au grain. Le grain a un comportement élastoplastique, la plasticité cristalline étant décrite par les lois présentées au chapitre III. La matrice a un comportement élastoplastique, mais par un souci de simplicité, son comportement plastique est décrit par une loi d'écrouissage cinématique de type Armstrong-Frederick. Une sollicitation de traction-compression cyclique est imposée à la matrice. Les résultats montrent que l'état de contrainte et de déformation dans le grain est hétérogène, au contraire de l'hypothèse du problème d'Eshelby. Il n'est donc pas possible de décrire par une loi de localisation l'ensemble des valeurs de contrainte du grain de surface. Nous avons fait le choix de simuler avec la loi de localisation la valeur moyenne dans le grain plutôt que les valeurs extrêmes. Afin de permettre de simuler des sollicitations cycliques, la loi de localisation proposée est écrite sous la même forme que la loi de Cailletaud-Pilvin, en introduisant une variable d'accommodation intergranulaire $\underline{\gamma}^{g}$. Les deux paramètres de la loi d'évolution de $\underline{\gamma}^{g}$ sont identifiés à partir de l'évolution de la moyenne des contraintes dans le grain de surface. 11 orientations différentes ont été simulées pour l'identification.

De nombreux modèles ont été proposés dans la littérature pour rendre compte de la durée de vie en fatigue. Une revue bibliographique en présente un certain nombre. L'objectif n'est pas de tester tous ces critères sur la base des observations présentées au chapitre IV mais d'en extraire un nombre limité d'indicateurs qui seront comparés à la base expérimentale. 8 indicateurs ont été sélectionnés : les 3 premiers sont calculés dans chaque grain : l'amplitude de déformation plastique équivalente, la déformation plastique cumulée, la somme des densités de dislocations ; les 5 suivants sot calculés pour chaque système de glissement et la valeur maximale sur l'ensemble des systèmes de glissemetn est conservée : la déformation de cisaillement maximale, la contrainte de cisaillement maximale, la valeur maximale du rapport de la cission déviée sur la cission primaire, la déformation de cisaillement cumulée, la densité de dislocation maximale.

La simulation est réalisée de la manière suivante. Le comportement mécanique du matériau est simulé à l'aide du modèle présenté au chapitre III. A chaque incrément de temps, la loi de localisation pour les grains de surface est utilisée afin de calculer l'état des contraintes dans les grains de surface, la même loi de plasticité cristalline est utilisée dans les grains de surface qu'en volume pour calculer

les déformations plastiques dans le grain. Deux familles de grains de surface sont considérés : les 12 grains dans lesquels des fissures de longueur importante ont été observées après 2000 cycles de l'essai de fatigue à 0.5% d'amplitude de déformation imposée et 488 grains ne présentant pas de fissure. Les distributions des indicateurs ont été comparées pour ces deux familles de grains. Les résultats montrent des distributions différentes entre les deux familles de grains pour les indicateurs amplitude de déformation plastique équivalente et déformation plastique cumulée mais pas pour les 6 autres indicateurs. Les distributions observées pour ces 6 indicateurs sont soit sur un intervalle très serré ce qui ne permet pas de discriminer entre les deux familles, soit des distributions de type normale sans vraie différence.

Par ailleurs, deux critères d'amorçage de la littérature ont également été analysés et comparés aux résultats expérimentaux. Il s'agit du critère d'amorçage de Mura [Mura 94] et de celui de Després (Després 04]. Le premier fait l'hypothèse qu'une fissure s'amorce quand l'énergie accumulée est supérieure à l'énergie de surface nécessaire à la création d'une fissure, tandis que le second relie à la déformation plastique cumulée dans les bandes de glissement persistantes. Aucune différence importante n'est observée entre les distributions de ces deux critères dans les grains fissurés ou non.

CONCLUSION GENERALE

Ce travail avait pour objectif de caractériser les premiers stades d'amorçage en fatigue oligocyclique dans un acier inoxydable austénitique et de fournir un cadre numérique permettant de tester des critères d'amorçage en fatigue vis-à-vis des observations expérimentales.

Le comportement mécanique de l'acier étudié a été caractérisé en fatigue oligocyclique. Il a été modélisé par un schéma autocohérent utilisant la loi de localisation de Cailletaud-Pilvin et une loi de plasticité cristalline basé sur l'évolution des densités de dislocations.

L'endommagement de surface a été suivi pendant un essai de fatigue à l'aide d'un dispositif de microscopie optique in situ. Les images acquises pendant l'essai ont permis de déterminer l'évolution des champs de déplacement et de déformation au cours du cyclage par corrélation d'images numériques, et d'en déduire le moment de l'amorçage. L'ensemble des fissures présentes dans une zone de 8.4 mm2 a été analysé et leurs caractéristiques cristallographiques calculées. La moitié des fissures ont amorcé sur une marque de glissement et 42 % aux joints de grains. Il a été montré que les grains fissurés ont un facteur de Schmid maximal supérieur à 0.41, et qu'environ 2/3 des grains fissurent sur le système de glissement ayant le facteur de Schmid maximal. Pour les autres, le système le mieux orienté vis-à-vis de la déformation plastique n'était pas un système favorisant

l'amorçage (grain de type A, faible volume débouchant), et une fissure a finalement été créée sur un autre système.

Une loi de localisation spécifique aux grains de surface a été identifiée à partir de simulations par éléments finis. La forme proposée fait intervenir une variable d'accommodation intergranulaire, sur le modèle de la loi de localisation de Cailletaud-Pilvin de l'approche auto-cohérente. L'état des contraintes et des déformations dans des grains de surface a alors été simulée, en comparant deux familles de grains : des grains présentant des fissures après 2000 cycles et des grains n'en présentant pas. 8 indicateurs basés sur des critères de fatigue de la littérature ont été analysés et comparés. Seules les distributions des indicateurs basés sur la déformation plastique équivalente montrent des différences entre les deux familles de grains. Deux critères d'amorçage de la littérature ont également été testés sans montrer de différence de distribution.

Même si la zone suivie et analysée au cours de l'essai était grande, le nombre de fissures reste limité et ne permet pas d'établir des statistiques importantes. Il est donc nécessaire d'élargir cette base expérimentale pour avoir d'une part plus de fissures pour une sollicitation donnée et d'autre part des sollicitations plus variées en testant d'autres niveaux de déformation et d'autres trajets de chargement.

L'adoucissement cyclique n'a pas été considéré dans cette étude. Cependant le durcissement/ adoucissement cyclique peut accroitre la concentration de contrainte ou de déformation dans certains grains ce qui favorise un amorçage précoce. Il serait donc intéressant de prendre en compte cet adoucissement dans le futur.

Résumé

« Etude de l'amorçage en fatigue plastique d'un acier inoxydable austénitique »

Bien que l'amorçage de fissure joue un rôle important en fatigue, ses mécanismes ne sont pas encore pleinement compris. Des critères d'amorçage basés sur des mécanismes physiques de déformation plastique ont été proposés mais ne sont pas faciles à utiliser et à valider, car ils nécessitent des variables locales à l'échelle du grain. L'étude présente vise à établir un critère d'amorçage en fatigue oligocyclique, utilisable sous chargement d'amplitude variable.

Le comportement mécanique de l'acier inoxydable AISI 316L étudié a été caractérisé en fatigue oligocyclique. Il a été modélisé par un schéma autocohérent utilisant une loi de plasticité cristalline basé sur l'évolution des densités de dislocations.

L'endommagement de surface a été suivi pendant un essai de fatigue à l'aide d'un dispositif de microscopie optique in situ. Les fissures présentes après 2000 cycles ont été analysées et leurs caractéristiques cristallographiques calculées.

Comme les grains de surface montrent une déformation plus importante à cause d'un moindre confinement par les grains voisins, il est nécessaire de définir une loi de localisation spécifique aux grains de surface. La forme proposée fait intervenir une variable d'accommodation intergranulaire, sur le modèle de la loi de localisation de Cailletaud-Pilvin. Elle a été identifiée à partir de simulations par éléments finis. L'état des contraintes et des déformations dans les grains de surface a alors été simulé. Des indicateurs d'amorçage potentiels ont ensuite été comparés sur une même base expérimentale. Deux indicateurs pertinents de l'endommagement en fatigue ont pu être obtenus.

Mots clés : fatigue oligocyclique, acier inoxydable austénitique, critère d'amorçage, modélisation multi-échelle , grain de surface, orientations cristallographiques, observation in situ loi de localisation.

Abstract

« Study of crack initiation in low-cycle fatigue of an austenitic stainless steel »

Although crack initiation is proved to play an important role in fatigue, its mechanisms have not been fully understood. Some crack initiation criteria based on physical mechanisms of plastic deformation have been defined. However, these criteria are not easy to use and valid, as they need local variables at the grain scale. The present study aims at establishing a crack initiation criterion in low-cycle fatigue, which should be usable under variable amplitude loading conditions.

Tension-compression fatigue tests were first carried out to characterize the mechanical behavior of the stainless steel AISI 316L studied. The mechanical behavior was simulated using a self-consistent model using a crystalline plastic law based on dislocation densities. The evolution of surface damage was observed during a fatigue test using an in situ optical microscopic device. Cracks were analyzed after 2000 cycles and their crystallographic characteristics calculated.

As surface grains exhibit larger strain because they are less constraint by neighbor grains a specific numerical frame is necessary to determine stress state in surface grains. A localization law specific to surface grains under cyclic loading was identified from finite element simulations The proposed form needs an intergranular accommodation variable, on the pattern of the localization law of Cailletaud-Pilvin. Stress-strain state in surface grains was simulated. Potential indicators for crack initiation were then compared on a same experimental data base. Indicators based on the equivalent plastic strain were found to be suitable indicators of fatigue damage.

Key words : low-cycle fatigue, austenitic stainless steel, crack initiation criterion, multi-scale modeling, surface grain, crystallographic orientations, in situ observation, localization law.